Mid-infrared GaSb-based Type-I Quantum Wells Diode Lasers Utilizing Cascade Pumping Scheme

A Dissertation Presented

by

Rui Liang

to

The Graduate School

in Partial Fulfillment of the

Requirements

for the Degree of

Doctor of Philosophy

in

Electrical Engineering

Stony Brook University

December 2014

Stony Brook University

The Graduate School

Rui Liang

We, the dissertation committee for the above candidate for the
Doctor of Philosophy degree, hereby recommend
acceptance of this dissertation.

Leon Shterengas – Dissertation Advisor
Associate Professor, Department of Electrical and Computer Engineering

Harbans Dhadwal - Chairperson of Defense
Associate Professor, Department of Electrical and Computer Engineering

Mikhail Gouzman
Adjunct Professor, Department of Electrical and Computer Engineering

David Hwang
Assistant Professor, Department of Mechanical Engineering

This dissertation is accepted by the Graduate School

Charles Taber
Dean of the Graduate School

Abstract of the Dissertation

Mid-infrared GaSb-based Type-I Quantum Wells Diode Lasers Utilizing Cascade Pumping Scheme

by

Rui Liang

Doctor of Philosophy

in

Electrical Engineering

Stony Brook University

2014

Mid infrared semiconductor diode lasers have broad range of applications, including light detection and ranging, infrared countermeasures, medical treatment and spectroscopy. Compact and efficient devices operating in continuous-wave (CW) regime at room temperature (RT) are preferred for those applications. This work is focusing on the development of GaSb-based type-I quantum wells (QWs) diode lasers in the spectral range of 2.2 – 3.4 μm, with high output power and Diffraction-Limited beam.

The novel design of cascade type-I QWs diode lasers was proposed. The interband tunneling through the "leaky" window in band alignment at GaSb/InAs heterointerface was used to realize cascade pumping of type-I GaSb QWs in the device active region. The GaSb/InAs tunnel junction required only moderate n-doping on InAs side and, thus, did not generate excessive absorption losses despite being located near the transfer mode peak. The two-stage cascade design provides twofold increase of the device slope efficiency as compared to that of single stage diode lasers. Corresponding high CW power RT operated 2.4 – 3.3 μm two-stage cascade diode lasers were fabricated. The cascade structure was further optimized to improve the QW optical confinement factor, and the threshold current density was reduced. The two- and three-stage cascade diode lasers demonstrated CW output power of 650 mW and 960 mW at 3 μm in RT, respectively.

Diffraction-Limited and distributed feedback diode lasers with narrow ridge waveguide were designed and fabricated. Various etching techniques (wet etching, Cl_2-free and Cl_2-based dry etching) were developed to improve the etching profile and lasers performance. Diffraction-Limited cascade diode lasers demonstrated CW output power of 100 mW at 3 μm, and 40 mW at 3.15 μm in RT, respectively. Distributed feedback 3.27 μm diode lasers demonstrated CW output power of 15 mW at RT.

Table of Contents

List of illustrations

List of tables

Publication

Journals:

[1] L. Shterengas, **R. Liang**, G. Kipshidze, T. Hosoda, G. Belenky, S. Bowman, R. Tober "Cascade type-I quantum well diode lasers emitting 960mW near 3μm", Applied Physics Letters, Vol. 105, 161112, 2014.

[2] **R. Liang**, T. Hosoda, L. Shterengas, A. Stein, M. Lu, G. Kipshidze, G. Belenky, "Distributed feedback 3.27 μm diode lasers with continuous wave output power above 15 mW at room temperature", Electronics Letters, Vol. 50, 1378, 2014.

[3] **R. Liang**, L. Shterengas, T. Hosoda, A. Stein, M. Lu, G. Kipshidze, G. Belenky, "Diffraction-Limited 3.15 μm Cascade Diode Lasers", Semiconductor Science and Technology, Vol. 29, 115016, 2014.

[4] **R. Liang**, G. Kipshidze, T. Hosoda, L. Shterengas, G. Belenky, "3.3 – 3.4 μm Diode Lasers Based on Triple-layer GaInAsSb Quantum Wells", IEEE Photonics Technology Letters, Vol. 26, 664, 2014.

[5] L. Shterengas, **R. Liang**, G. Kipshidze, T. Hosoda, G. Belenky, "Type-I Quantum Well Cascade Diode Lasers Emitting near 3 μm", Applied Physics Letters, Vol. 103, 121108, 2013.

[6] T. Hosoda, **R. Liang**, G. Kipshidze, L. Shterengas, G. Belenky, "Room Temperature Operated Diffraction-Limited $\lambda \simeq 3$ μm Diode Lasers with 37 mW of Continuous-wave Output Power", Electronics Letters, Vol. 49, 667-668, 2013.

[7] **R. Liang**, T. Hosoda, G. Kipshidze, L. Shterengas, G. Belenky, "GaSb-based Diode Lasers with Asymmetric Separate Confinement Heterostructure", IEEE Photonics Technology Letters, Vol. 25, 925-928, 2013.

[8] S. Jung, **R. Liang**, G. Kipshidze, S. Suchalkin, L. Shterengas, G. Belenky, "Single Spatial Mode 2-2.2 μm Diode Lasers Fabricated by Selective Wet Etching", Semiconductor Science and Technology, Vol. 27, 085004, 2012.

[9] S. Jung, G. Kipshidze, **R. Liang**, S. Suchalkin, L. Shterengas, G. Belenky, "GaSb-Based Mid-Infrared Single Lateral Mode Lasers Fabricated by Selective Wet Etching Technique with an Etch Stop Layer", Journal of Electronic Materials, Vol. 41, 899-904, 2012.

[10] **R. Liang**, J. Chen, G. Kipshidze, L. Shterengas, G. Belenky, "High Power 2.2 μm Diode Lasers With Heavily Strained Active Region", IEEE Photonics Technology Letters, Vol. 23, 603-605, 2011.

Conference Proceedings:

[11] **R. Liang**, L. Shterengas, G. Kipshidze, T. Hosoda, S. Suchalkin, G. Belenky, "Novel Cascade Diode Lasers Based on Type-I Quantum Wells", International Journal of High Speed Electronics and Systems, Vol. 23, 3 & 4, 1450022, 2014.

[12] L. Shterengas, **R. Liang**, G. Kipshidze, T. Hosoda, S. Suchalkin, G. Belenky, "Cascade Pumping of GaSb-based Type-I Quantum Well Diode Lasers", Proceedings SPIE OPTO, 900213-900213-10, 2014.

[13] T. Hosoda, J. Chen, G. Tsvid, D. Westerfeld, **R. Liang**, G. Kipshidze, L. Shterengas, G. Belenky, "Progress in Development of Room Temperature CW GaSb Based Diode Lasers for 2-3.5 μm Spectral Region", International Journal of High Speed Electronics and Systems, Vol. 20, 43-49, 2011.

[14] J. Chen, T. Hosoda, G. Tsvid, **R. Liang**, D. Westerfeld, G. Kipshidze, L. Shterengas, G. Belenky, "Type-I GaSb Based Diode Lasers Operating at Room Temperature in 2 to 3.5 μm Spectral Region", Proceedings of SPIE, 7686, 76860S, 2010.

Conference Presentations:

[15] **R. Liang**, L. Shterengas, T. Hosoda, A. Stein, M. Lu, G. Kipshidze, G. Belenky, "Diffraction-Limited 3.15 μm Cascade Diode Lasers", 72nd Device Research Conference, Jun. 2014, Santa Barbara, CA, USA.

[16] L. Shterengas, **R. Liang**, G. Kipshidze, T. Hosoda, S. Suchalkin, G. Belenky, "Cascade Pumping of GaSb-based Type-I Quantum Well Diode Lasers", SPIE Photonics West 2014, Feb. 2014, San Francisco, CA, USA.

[17] **R. Liang**, L. Shterengas, G. Kipshidze, T. Hosoda, S. Suchalkin, G. Belenky, "Novel Cascade Diode Lasers Based on Type-I Quantum Wells", 8th Workshop on Frontiers in Electronics (WOFE-2013), Dec. 2013, San Juan, Puerto Rico.

[18] **R. Liang**, T. Hosoda, G. Kipshidze, L. Shterengas, G. Belenky, "3 μm GaSb-based Type-I Quantum-Well Diode Lasers with Cascade Pumping Scheme", Conference on Lasers and Electro-Optics (CLEO: Science and Innovations), Jun. 2013, San Jose, CA, USA.

[19] L. Shterengas, G. Kipshidze, T. Hosoda, **R. Liang**, S. Jung, D. Westerfeld, G. Belenky "Diode lasers operating in spectral range from 1.9 to 3.5 μm", 23rd IEEE International Semiconductor Laser Conference (ISLC), Oct. 2012, San Diego, CA, USA.

Acknowledgments

I would like to take this opportunity to express my gratitude to my advisor Prof. Leon Shterengas for the continuous support, intellectual guidance, invaluable advice and encouragement on my way of pursuing PhD degree.

I would like to thank Prof. Gregory Belenky for the invaluable guidance and support.

I would like to thank Prof. Dmitri Donetski, Prof. Sergey Suchalkin, Prof. David Westerfeld, Dr. Gela Kipshidze, and Dr. Takashi Hosoda for the help and collaborations.

I would like to thank all the colleagues I have worked with in Optoelectronics Group at Stony Brook, Dr. Jianfeng Chen, Dr. Seungyong Jun, Dr. Ding Wang and Youxi Lin.

At last, I must gratefully thank my wife, Ying Su, my parents and family for their support during my PhD study.

Chapter 1 Introduction

Laser, or the light amplification by stimulated emission of radiation, amplifies lights in gain mediums by positive feedback between the facets of a resonant cavity, and emits the coherent light. Semiconductor lasers, which are using semiconductor as the medium, were firstly invented at1962 [1-3]. Because of their versatilities and advantages, including compactness, low power consumption, modulability, mass productivity and inexpensive costs, semiconductor lasers have been rapidly developed into one of the most important and most widely implemented optoelectronics devices in many areas to fulfill different requirements and purposes. In this work, we are focusing on the edge-emitting Fabry-Perot semiconductor diode lasers operating in the mid infrared spectral range.

1.1 Applications of mid infrared diode lasers

Mid infrared semiconductor diode lasers emitting in the spectral range of 1.9 – 3.5 μm, have broad range of applications in medical, industrial, scientific and defense areas For medical application, it is notable that at the spectral range of 2.7-3.0 μm there is strong water absorption, which can be used for surgery, like in dentistry, 3.0 μm lasers could be applied in cavity cares, gum diseases and many other pain free treatments [4, 5]. The mid-infrared lasers can also be used in chemical and biological spectral analysis for medical diagnostics, for example, the non-invasive blood glucose detection for treatment of diabetes due to the glucose absorption at 2.3 μm, and some gases related to some diseases could be detected cause of their absorption at mid-infrared range. For industrial and scientific areas, the mid-infrared lasers could be used for materials processing, pumping of solid-state and fiber laser, free space transmitters (atmospheric transparency windows at 3 - 5 μm with minimum background noises), tunable diode laser absorption spectroscopy (TDLAS) or gas detection and leakage monitoring systems, for these industrial gases in the spectral range: C_2H_2 (2.98 - 3.11 μm), CH_4 (3.15 - 3.50 μm), C_2H_6 (3.22 - 3.69 μm), C_2H_4 (3.09 - 3.42 μm), HCl (3.396 μm) [6, 7]. For the defense and security areas, mid-infrared lasers could be used for remote explosive identification, hazard gases detection, infrared illumination and countermeasures, and light detection and ranging (LIDAR) [8].

All these applications discussed above prefer the compact and efficient devices operating in continuous wave (CW) regime at room temperature (RT). For the mid infrared spectral range of 1.9 – 3.5 μm, the GaSb-based type-I quantum wells (QWs) laser diodes can serve as an ideal light source for those of applications, owing to the excellent performance, compactness and efficiency.

1.2 Design and materials of GaSb-based type-I QWs diode lasers

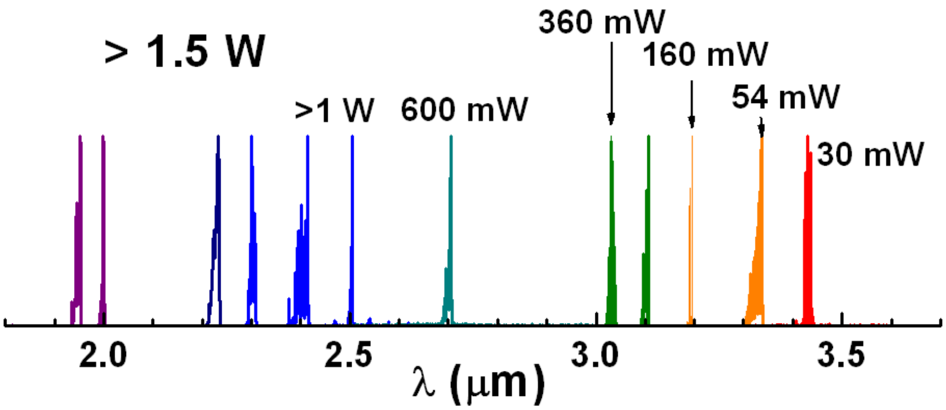

Figure 1.1 CW output power achieved in RT for the GaSb-based single stage type-I QWs diode lasers in the spectral range of 1.9 – 3.5 μm at Stony Brook University by 2010.

The GaSb-based type-I QWs diode lasers emitting in the mid-infrared range of 2.0 - 3.5 μm have shown significant progress. In our research group at Stony Brook University, the single laser emitter with Watt level CW output power in RT has been achieved in the spectral range of 1.9 – 2.5 μm [9], while the 3 μm lasers showing up to 360mW output power of CW mode in RT [10], and the CW operation was achieved at the emission wavelength as high as 3.44 μm (30 mW) [11] (Figure 1.1). In this section, the design and characteristics of typical GaSb-based type-I QWs diode lasers will be introduced from devices to structure, and parameters to performance.

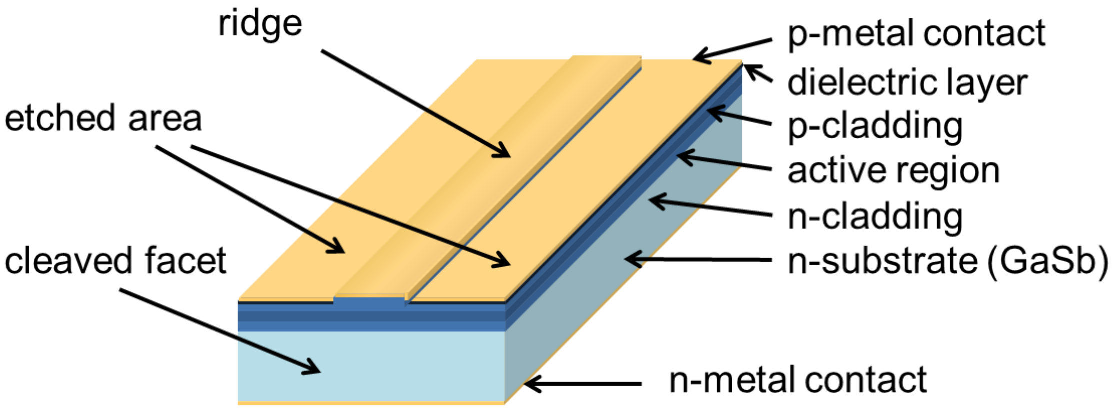

Figure 1.2 Schematic diagram of an edge emitting laser diode

A typical edge emitting device of GaSb-based type-I QWs diode laser can be shown in Figure 1.2. From the bottom of the device, there are n-metal contact, n-doped substrate, n-doped cladding layer, active region, which including QWs sandwiched by undoped waveguide, then p-doped cladding layer, p-dope cap, dielectric layer, and p-metal contact. Basically, there are graded buffer layers between cladding layers and substrate or cap, which help the carriers to transport. The dielectric layer is to confine the current injected into the active stripes, which are more often to be made as ridges by etching the rest areas, in order improve the current confinement by limiting the lateral current spreading, and also the optical confinement by increasing the refractive index different between the active stripes and the neighboring areas, and this is called index guided structure. The active stripe is where the spontaneous and stimulated emissions take place and be amplified when the carriers are injected in to the QWs and recombined radiatively. The front and back sides of the laser device are cleaved facets, forming the laser cavity, in where the emitted photons are bounced and amplified, and then reach the lasing eventually when the optical gain overcomes the total optical loss which including the internal loss and mirror loss. The cleaved facets can be coated by anti-reflective (AR) and high-reflective (HR) coatings, to get a specific reflectivity to improve the output power, and the coating can also protect the semiconductor devices from oxidation.

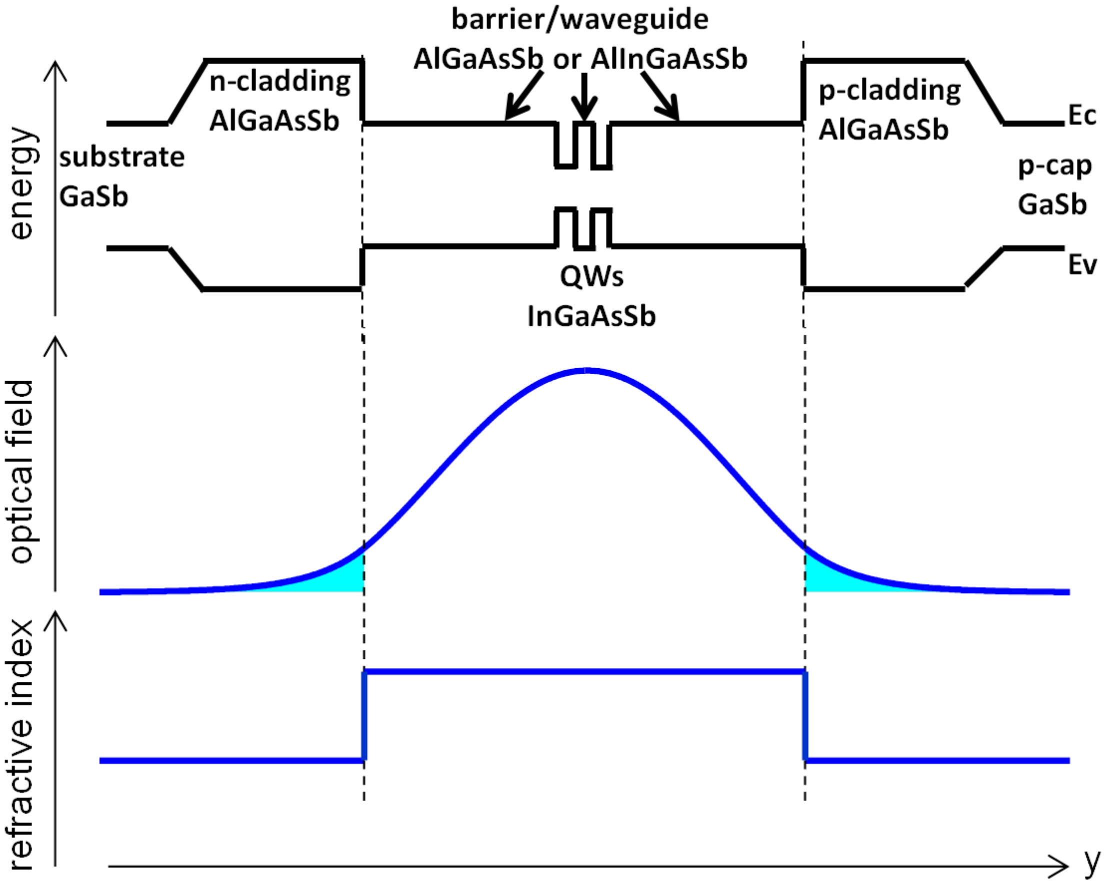

Figure 1.3 Schematic energy band diagram of GaSb-based type-I laser heterostructure with corresponding refractive index profile and optical field distribution.

Figure 1.3 schematically shows the energy band diagram of the typical heterostructure of GaSb-based type-I QWs diode lasers, as well as the refractive index profile and optical field distribution. The pseudomorphic wafers are grown by molecular beam expitaxy (MBE) on GaSb substrates. On the wafer epitaxial growth direction (from left hand side to right), there are GaSb substrate, contact, n-cladding AlGaAsSb, waveguide of AlGsAsSb or AlInGaAsSb sandwiching the QWs of InGaAsSb, then p-cladding AlGaAsSb and p-cap GaSb. All the layers except QWs are lattice-matched to the GaSb substrate.

The QWs are using InGaAsSb quaternary alloy in our GaSb-based type-I QWs diode lasers. The $In_xGa_{1-x}As_ySb_{1-y}$ has a direct bandgap for all alloy composition and is lattice matched to GaSb when y = 0.913x. Comparing to the ternary materials, such as GaInAs, the quaternary materials for active layer have an additional degree of freedom for the QWs design. The bandgap E_g, strain ε_{zz}, and band offsets ΔE can be adjusted individually within certain limitations by changing the composition. But in the GaSb lattice-matched InGaAsSb, there is a strong asymmetry between the light conduction band mass and the heavy valence band mass. As a result, the usual semiconductor laser picture of a degenerate distribution of both electrons and holes does not actually apply. The upper laser levels in the conduction band are indeed filled with electrons while the lower lasing levels in the valence band are not totally empty. Due to the heavy valence band mass, the holes quasi-Fermi level is above the top of the valence band. Hence, the holes occupation probability at the top of the valence band is relatively small compared to the electrons occupation probability at the bottom of the conduction band.

In modern laser designs, compressively strained QWs are typical. Strained layer are very thin and lattice mismatched, accompanied by a uniform elastic strain. This strain reduces the cubic symmetry of the semiconductors and modifies the electronic and optical properties of the QW [12]. InGaAsSb QWs with decreased As composition are compressively strained. The compressive strain splits the first heavy-hole and first light-hole subbands and reduces hole density of states (DOS) at the valence band edge, so the electron and hole DOS are baclenced [13]. In addition, the compressive strain can also increase valence band offset between QWs and barriers, which can help improving the holes confinement, then improving the internal efficiency and temperature characteristics of lasers.

AlGaAsSb quaternary alloy is used as the barrier or waveguide materials used for GaSb-based type-I QWs diode lasers emitting 2.x μm. Increasing Al and As composition in the AlGaAsSb can increase the valence band offset between QWs and barriers. The utilization of broaden waveguide separate confinement structure design [9] provided lower internal optical losses due to the reduction of free carrier optical losses in doped cladding layers, by increasing the waveguide width and reduced the optical field overlap factor on claddings. Successfully reduced internal optical loss and DOS in QWs, in turn decreased the threshold current density. With the compressively strained QWs and broadened waveguide design, the CW output power in RT was boosted above watt level for the GaSb-based type-I QWs diode lasers emitting 2.x μm.

The heterostructure of InGaAsSb/AlGaAsSb has strong misbalance between conduction and valence band offsets, the conduction band offset usually exceeds the valence band offset. So the localization of holes could be very poor while the electrons confinement is sufficient. The holes can emit thermionically from QWs into the barriers and waveguide and subsequently recombine, and then decrease the internal efficiency with temperature. This hole leakage is greater as longer wavelength due to the valence band offset is further reduced because of the In concentration is higher in the InGaAsSb QWs for longer wavelength [14, 15].

One option to address the strong misbalance between conduction and valence band offsets is to introduce quinary AlInGaAsSb as barrier and waveguide material which offers the possibility to adjust independently conduction and valence band energy. This independent adjustment would enable us to increase the valence band offset without changing conduction band offset between QWs and barriers. The utilization of quinary AlInGaAsSb alloy as barrier realized the CW operation of GaSb-based diode lasers with emission wavelength at 3 μm and above (as high as 3.44 μm) in RT [16].

However, presumably inefficient carrier delivery through the quinary AlInGaAsSb alloy waveguide core layers limited the device performance. Hence, the broadened waveguide design that was successfully utilized to reduce internal optical loss of 2.x μm GaSb-based type-I QWs diode lasers did not result into improved efficiency of ~3 μm lasers with quinary waveguide cores. The broadening of the waveguide core indeed reduced internal losses but simultaneously led to reduction of the device internal efficiency [17].

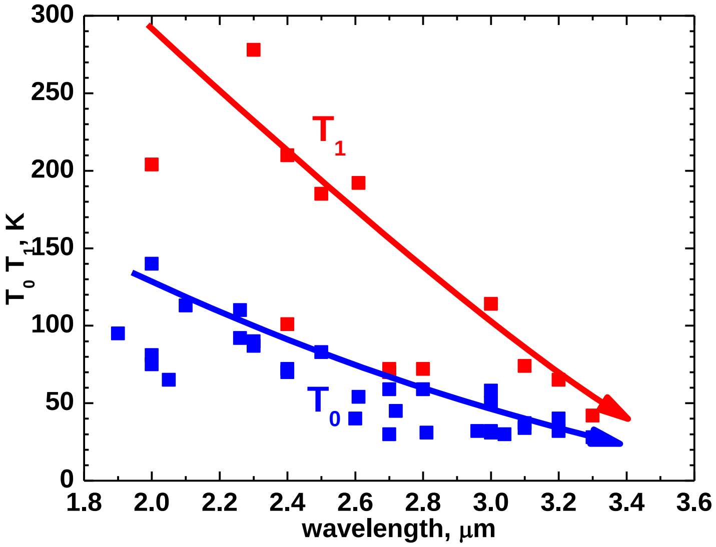

Figure 1.4 Characteristic temperature T_0 and T_1 for devices in the spectral range of 2-3.5 μm [18]

Besides the issues of insufficient hole confinement and inefficient carrier delivery in quinary alloy, the Auger recombination and free carrier absorption are increased when lasers wavelength increased from 2.x to 3.x μm. Thus the longer wavelength devices, especially λ > 3 μm, exhibit a greater deterioration in performance with increasing temperature, their characteristic temperature T_0 and T_1 decrease, as shown in Figure 1.4, and the CW output power in RT is limited far below watt level. In this work, we will focus on the development of λ > 3 μm GaSb-based type-I QWs diode lasers with improved efficiency and output power.

1.3 Characteristics and parameters of QWs diode lasers

In the QWs semiconductor lasers, the electrons and holes are electrically injected into the QWs. The carriers are localized in the QWs because of the energy band offset between QWs and barriers. The carriers can recombine together either in radiation or non-radiation. The recombination process is expressed as follows:

$$R_{rec} = R_{nr} + R_r \tag{1.1}$$

Here R_{rec} is the rate of recombination electrons per unit volume in the active region, R_{nr} is the rate of nonradiative recombination, and R_r is the rate of radiative recombination. R_{nr} and R_r can be rewritten as

$$R_{nr} = R_{SRH} + R_{Auger} = AN + CN^3 \tag{1.2}$$

$$R_r = BN^2 \tag{1.3}$$

Here R_{SRH} is the Schockley-Read-Hall (SRH) recombination rate, R_{Auger} is the Auger recombination rate, N is the electron density in the QWs, A, B, and C are SRH, radiative and Auger recombination coefficients respectively.

The radiation induced photons can interact with electrons in conduction band and holes in valence band to stimulate emission of identical photons. If the injected carrier concentration (electrons in conduction band, holes in valence band) becomes strong enough, the stimulated emission will exceed the absorption and reach the positive optical gain. The optical field will be confined within the nominally undoped waveguide, due to the refractive index difference between waveguide (higher index) and cladding layers (lower index). Because of difference in spatial extends of carrier wave function and electromagnetic field mode, the modal gain (g) is given by product of confinement factor (Γ) and material gain (G) which is defined as:

$$g = \Gamma \cdot G = \frac{dg}{dI}(I - I_{tr}) \tag{1.4}$$

Here dg/dI is the differential gain, I is the input current, I_{tr} is the transparency current.

To achieve lasing, positive feedback of the radiation (partially) is required, which is generally provided by a pair of cleaved facets, perpendicular to the waveguide axis, and form the resonance cavity. During the propagation, the optical wave will experience the loss which is generally due to intraband and interband absorption. In the case of intra-band absorption, the photon is absorbed by a free electron or hole, which is excited to a higher energy state in the conduction or valence band respectively. Because of momentum conservation, the intraband transition can only take place with the help of an additional interaction with a phonon or an impurity. This loss mechanism increases in strength with increasing wavelength proportional to λ^k with k in the range of 2 to 3.5. In the case of interband absorption, the absorbed photon energy excites an electron from a filled state in a lower lying band to an empty state in a higher lying band. Considering about the losses in different layers, total internal loss is comprised of the active layer loss α_a, the waveguide core loss α_{wg}, and the cladding loss α_{cl} (which including mode leakage loss, if any):

$$\alpha_{int} = \alpha_a + \alpha_{wg} + \alpha_{cl} \tag{1.5}$$

After reaching the transparency condition, corresponding pumping of the active region, for instance, the injection of the carriers from claddings into QWs must create population inversion in QWs, which is defined as:

$$f_c - f_v > 0 \tag{1.6}$$

Here f_c and f_v are Fermi distribution functions of electrons in conduction band and holes in valence band. From Equation 1.6, the energy separation of quasi-Fermi levels of electrons and holes must exceed the bandgap of QW material to reach the transparency condition. After the population is reversed, more current is required to separate the quasi-Fermi levels of electrons and holes further away to reach the threshold condition simultaneously, while material gain becoming threshold material gain G_{th}.

$$\Gamma \cdot G_{th} - \alpha = 0 \tag{1.7}$$

Here α is the total loss defined as:

$$\alpha = \alpha_{in} + \alpha_m \tag{1.8}$$

And α_m is mirror loss

$$\alpha_m = \frac{1}{L} ln\,(R_1 R_2) \tag{1.9}$$

The threshold current I_{th} is determined by transparency current I_{tr}, differential gain dg/dI , and totol loss α, as follows:

$$I_{th} = I_{tr} + \frac{\alpha}{dg/dI} \tag{1.10}$$

After reaching the threshold condition, the carrier concentration and material gain in the QWs are pinned at their threshold value, and all the extra injected carriers from cladding layers will recombine radiatively with internal efficiency η_{int} to convert the inputted electric power to the optical power output:

$$P = \eta \cdot (I - I_{th}) \tag{1.11}$$

Here η is the slope efficiency, measured in W/A, is defined as:

$$\eta = \frac{hv}{q} \eta_{int} (I - I_{th}) \frac{\alpha_m}{\alpha_m + \alpha_{int}} \tag{1.12}$$

Here q is electron charge, hv is photon energy, η_{int} is internal efficiency, the fraction of the current after threshold leading to photon generation.

The performances of semiconductor lasers are dependent on devices temperature, because the population of electrons states coupled into the laser mode is governed by Fermi statistics. The changes of the laser threshold and efficiency with temperature can be expressed as:

$$I_{th}(T) = I_{th}(T_{ref}) \cdot exp\left(\frac{T-T_{ref}}{T_0}\right) \tag{1.13}$$

$$\eta(T) = \eta(T_{ref}) \cdot exp\left(-\frac{T-T_{ref}}{T_1}\right) \tag{1.14}$$

T_{ref} is certain reference temperature and T is device temperature, T_0 and T_1 are Empirical characteristic temperature. Becuase contribution of different mechanisms to device thermal sensitivity varies with temperature, the T_0 and T_1 are functions of temperature itself. Higher T_0 and T_1 indicate relatively low temperature sensitivity of the device threshold and efficiency, which are preferred in semiconductor laser engineering. For GaSb-based type-I QWs diode lasers, the longer wavelength devices, especially λ > 3 μm, exhibit a greater deterioration in performance with increasing temperature, their characteristic temperature T_0 and T_1 decrease, as shown in Figure 1.4.

Chapter 2 Single Stage Diode Lasers Emitting in 2.2 - 3.4 µm

2.1 Introduction

Lasers operating in the spectral region from 2.2 to 3.4 µm are in demand for variety of applications in areas ranging from medical to industrial and military, including tunable diode laser spectroscopy, light detection and ranging, pump for solid state and fiber lasers and direct source for infrared countermeasures. High power, compact and efficient semiconductor lasers operating in CW regime at RT are in demand for various applications. GaSb-based single stage type-I QWs semiconductor laser technology is uniquely suited to address this demand.

High power GaSb-based diode lasers have been reported in the spectral region of 1.9 to 2.5 µm [9, 19-26]. Studies on the role of compressive strain above 1 % on the threshold and efficiency of GaSb-based diode lasers have been performed [13, 27]. It was demonstrated that increasing the compressive strain from 1 to 1.5 % in GaInAsSb QWs improves both the differential gain and the threshold current density of diode lasers. Both heavy-light hole splitting and reduced As composition in heavily strained QWs shift the valence band edge upward. We advocate that the increased valence band offset between the heavily compressively strained GaInAsSb QWs and the AlGaAsSb barrier layers is responsible for the observed enhancement of the device performance parameters. It is also important to use relatively narrow QWs (~ 10 nm or narrower) to maintain sufficient separation between topmost heavy hole subbands. The mechanism of improvement is related to the dramatically reduced thermal population of the barrier and second subband states and the resulting decrease of the threshold carrier concentration. The reduction of the threshold carrier concentration results from both the decreased transparency carrier concentration and increased differential gain.

The CW RT operation of GaSb-based type-I QW diode lasers in spectral region above 2.8 μm was demonstrated after the carrier confinement in the active QWs was improved [28]. This was achieved when quaternary AlGaAsSb barriers were replaced with quinary AlGaInAsSb barriers resulting into increased valence band discontinuities in GaInAsSb QWs [16]. However, presumably inefficient carrier delivery through five component alloy waveguide core layers limited the device performance [28]. The broadened waveguide design approach [29] that was successfully utilized to reduce internal optical loss of GaSb-based 2.2 μm lasers [30] did not result into improved efficiency of λ ~3 μm emitters with quinary waveguide cores [17]. The broadening of the waveguide core indeed reduced internal losses but simultaneously led to reduction of the device internal efficiency. The best operating parameters of λ > 3 μm diode lasers were obtained for narrow waveguide devices and their injection efficiency was still near or below 50% [28]. One possible approach to resolve this issue could be based on detailed studies of the carrier transport constraints and nonradiative recombination in quinary alloys followed by development of the advanced growth methodology.

In the spectral range above 3.3 μm, an advantage of the interband mid-Infrared semiconductor diode lasers [31, 32] as compared to quantum cascade intersubband lasers (QCLs) [33] is low turn-on power level. Diode lasers with type-I QWs active region operate at RT up to 3.44 μm in CW regime [28] and up to 3.73 μm in pulsed mode [34]. One of the challenges of development of the type-I QWs GaSb-based diode lasers for wavelength above 3 μm is degradation of the hole confinement barriers in narrow gap QWs with high In and As content [28]. A well established alternative approach to get to longer wavelength is to utilize InAs/GaInSb/InAs W-QW active region [35]. This approach led to development of the efficient cryogenically operated optically pumped [36] and CW RT operated interband cascade lasers

(ICLs) [31, 32]. However, previously reported diode lasers based on multiple W-QW active regions operated at RT only in pulsed regime [36]. One possible explanation is carrier transport constraints associated with hole tunneling through multiple ~ 2-nm-thick InAs layers and, consequently, inefficient use of the multiple W-QW active region. In case of both optically pumped and ICL devices, the uniform pumping of many active W-QWs is achieved contributing to the efficient device operation.

In this chapter, we will discuss novel design and optimization on the heterostructure of GaSb-based single stage diode lasers, for the purpose of improving the efficient and performance of lasers in the spectral range of 2.2 to 3.4 μm. These endeavors includes the 2.2 μm diode lasers and arrays with heavily strained active region, 3.1 μm diode lasers with asymmetric separate confinement heterostructur e, and 3.3-3.4 μm diode lasers with triple-layer GaInAsSb QWs.

2.2 2.2 μm diode lasers and arrays with heavily strained active region

In this section, we demonstrate the heavily strained active region design approach with the fabrication of 2.2 μm high power diode lasers and their arrays [30]. The heavy compressive strain (1.5%) in the GaInAsSb QWs ensured strong carrier confinement and high differential gain. A broadened waveguide design approach was utilized to obtain an internal optical loss below 4 cm and a threshold current density below 100 A/cm^2. Individual high-power lasers produced 1.6 W of CW multimode power at RT from a single 100-μm-wide aperture. Linear laser arrays generated more than 25 W of quasi-CW output power. The device power conversion efficiencies were better than 20% in peak and above 10% at maximum output power level.

2.2.1 Laser heterostructure and device fabrication

The laser heterostructure was grown by solid-source MBE on Te-doped GaSb substrates in a Veeco GEN-930 modular system equipped with valved cracker cells for As and Sb. All layers except for QWs were lattice matched to the substrate. Heavily doped graded bandgap layers were introduced between the n(p)-GaSb buffer(cap) layers and the n(p)-$Al_{85}Ga_{15}As_7Sb_{93}$ cladding layers. The claddings were 1.5 μm thick and were doped with Te (nominal n= 10^{18} cm^{-3}) and Be (nominal p= 10^{17} cm^{-3} for the first 500 nm adjacent to the waveguide core and 10^{18} cm^{-3} for the remaining 1 μm). Lower than nominal n-doping levels are expected in quaternary aluminum-containing alloys. The waveguide core was composed of a dual-QW active region centered between 400-nm-thick nominally undoped $Al_{30}Ga_{70}As_3Sb_{97}$ layers. Aluminum content in barrier alloy was increased to 30 % from previously used 25% [24] to improve hole confinement. The QWs were 11-nm-thick $In_{28}Ga_{72}As_3Sb_{97}$ with a compressive strain of 1.5 % separated by a 20-nm-thick $Al_{30}Ga_{70}As_2Sb_{98}$ barrier. The valence band offset between the QW and barrier materials was estimated to be adequate at about 150 meV, while the band offset in the conduction band is ample and in excess of 500 meV [37, 38]. Optical field calculations [39] predict the overlap of the laser mode with the p-cladding to be about 6 %, resulting in low optical losses in these GaSb-based broadened waveguide lasers [19].

The laser wafer was processed into an index guided ridge waveguide structure by wet etching of the p-cladding layer outside of the 100-μm-wide current stripes. Laser temperature sensitivity characterization and laser optical gain measurements were performed using uncoated 1-mm-long devices In-soldered epi-side up onto copper blocks. For CW characterization the bars were cleaved and immediately loaded to vacuum reactor to be coated AR (3%) / HR (95%). The AR coating was single quarter wave layer of Al_2O_3 while HR was two periods of a Si/Al_2O_3 Bragg reflector. Both the individual devices and the linear laser arrays were In-soldered epi-side-down with flux onto gold-coated copper blocks. Top contacts were wire-bonded. CW characterization was performed with mounted devices bolted to a Peltier-cooled copper plate.

The hot side of the Peltier was water-cooled. The cooling system was capable of removing about 100 W of heat.

Laser output power was measured using a calibrated thermopile sensor with a 2 cm diameter aperture. The sensor was placed about 1 cm away from the laser output mirror and no collecting optics were used. The far field distributions were measured by scanning a single 500 μm diameter photodetector at a distance of about 30 cm away from laser front mirror. Optical gain was measured using the Hakki-Paoli method [40] with a Fourier transform spectrometer and external InSb photodetector. Amplified spontaneous emission collection and beam focusing on the photodetector were performed using reflective optics. A mechanical slit (about 1 mm) in front of the reflective objective (numerical aperture, NA = 0.5) was used to filter out the higher order lateral modes of the laser cavity.

2.2.2 Results and discussion

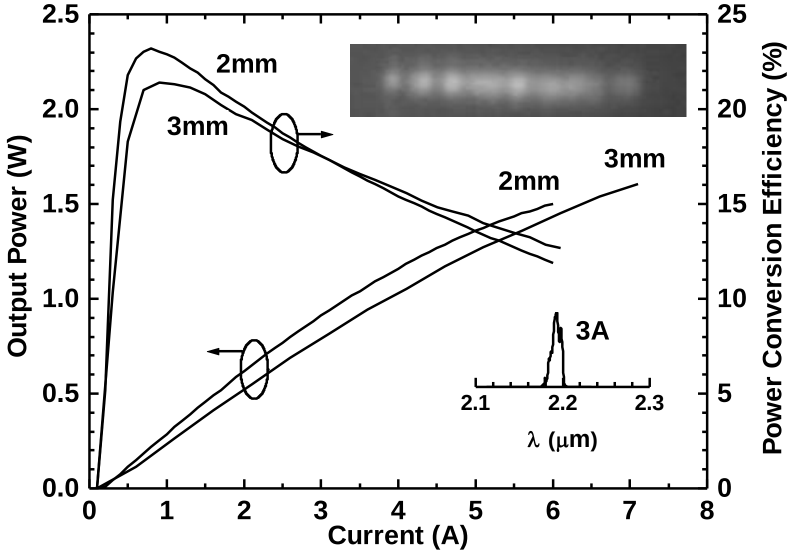

Figure 2.1 Power and power conversion characteristics of 2- and 3-mm-long AR/HR coated lasers measured in CW at 17 °C. Insets show near field (top) and laser spectrum (bottom).

Figure 2.1 shows the measured CW output powers and power conversion efficiencies of individual lasers at a heat sink temperature of 17 °C. A CW output power of 1.5 W was reached at 6 A for the 2-mm-long devices. Lasers with 3 mm long cavity length and, hence, increased thermal footprint generated 1.6 W at 7A despite reduced overall device efficiency. Device power conversion efficiency (PCE) peaked at more than 20 % and remained above 10 % at the maximum output power level. CW external efficiency near threshold was 52%. The temperature stability of the efficiency is characterized by a parameter T_1 of about 290 K as measured in the temperature range from 15 to 60 °C. This excellent temperature stability indicates that there are no severe current leakage paths.

The laser spectrum was centered near 2.19 μm at a current of 3 A, with a full-width at half-maximum (FWHM) of 12 nm. Divergence in the fast axis direction was typical for diffraction-limited broadened waveguide lasers with a FWHM of about 63^o that is independent of current. The calculated fast axis far field distribution had a beam divergence of about 62^o, i.e. in close correspondence to the experimental value. Beam divergence in excess of 60^o FWHM complicates fiber coupling and requires coupling optics with numerical aperture above 0.5. Asymmetric waveguide design can be utilized to reduce the fast axis beam divergence down to about 40^o FWHM [26]. The multimode beam in the slow axis direction shows a far field divergence of about 10^o that tends to increase somewhat with current. The corresponding near field pattern (Figure 2.1 inset) clearly shows filamentation with an average filament spacing of about 12 μm. This is indicative that stable single spatial mode operation can be expected for 10-μm-wide or narrower ridge waveguides.

High power lasers demonstrate CW threshold current densities below 100 A/cm^2; less than 50 A/cm^2 per QW. The value is comparable to the best values reported for diode lasers at any wavelength even though our laser heterostructure has not been optimized for maximum optical confinement in the QW. The threshold current density demonstrates excellent temperature stability as indicated by a T_0 parameter above 90 K as measured over a temperature range from 15 to 60 °C. This observation challenges the conventional belief that nonradiative Auger recombination should hamper the performance of mid-infrared lasers. While the probability of Auger processes increases with wavelength, the probability of radiative recombination and the effective density of states are also wavelength dependent. Narrowing the QW bandgap reduces the electron in-plane effective mass and the effective density of states. This results in a lower transparency concentration and increased differential gain for these mid-infrared lasers. The increased gain and lower transparency concentration act to reduce the threshold carrier concentration. Auger processes increase superlinearly with carrier concentration, so the reduced carrier concentration pays important benefits in reducing the effect of Auger recombination.

In order to take full advantage of the lowered density of states in the conduction band, it is necessary to take measures to reduce the net density of states in the valence band. This is achieved through the introduction of compressive strain in relatively narrow QWs. It should be noted that in GaSb-based type-I QW lasers not only the usual effect of lightening of the heavy hole effective mass is important. It is critical to maximize the valence band offset in the active QWs by using heavily strained GaInAsSb alloys with minimal As composition and proper barrier material. Otherwise the thermal population of the barrier states will effectively make the valence band carriers “heavier”. This repels the electron and hole quasi-Fermi levels from the band edges at laser threshold and increases the threshold carrier concentration.

Figure 2.2 plots the measured current dependence of the modal gain spectra. An internal optical loss of 3 - 4 cm^{-1} can be estimated. This relatively low internal optical loss was achieved by waveguide broadening in combination with reduced doping of the p-cladding section adjacent to waveguide core. The net modal differential gain is about 370 cm^{-1}/A. Transparency current density is about 40 A/cm^{2}. These experimental results can be interpreted to support the argument discussed above. The low electron effective density of states in narrow bandgap QWs decreases the threshold carrier concentration in heavily compressively strained QWs with adequate hole confinement.

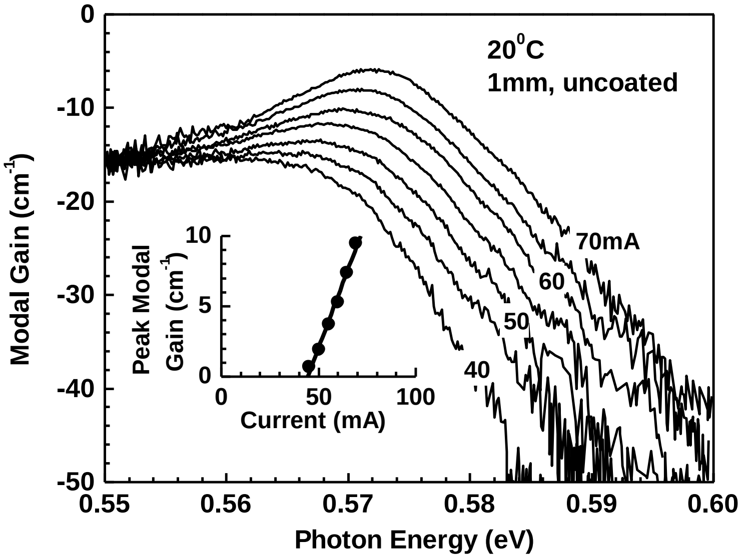

Figure 2.2 Current dependences of the modal gain spectra measured at 17 °C for 1-mm-long uncoated devices. Inset shows the corresponding dependence of the peak modal gain on current.

Figure 2.3 shows the measured CW power and power conversion characteristics of a 22 element 1-mm-long cavity linear laser array at a heat sink temperature of 17 °C. The array fill-factor was a conservative 20 %. Each laser element emitted through a 100-μm-wide aperture. The inset shows the near field image of the array output mirror. A CW output power of more than 12 W was reached at 50 A where PCE is about 10 %. Saturation of the CW output power level is caused by the limitations of the Peltier cooler. The laser array spectrum experiences red shift and line broadening with current (see inset). At 40 A the output is centered at 2.23 μm with a linewidth of about 20 nm. In the quasi-CW regime (30 μs/300 Hz) with dramatically reduced thermal load, the array output power reaches 27W at 90A.

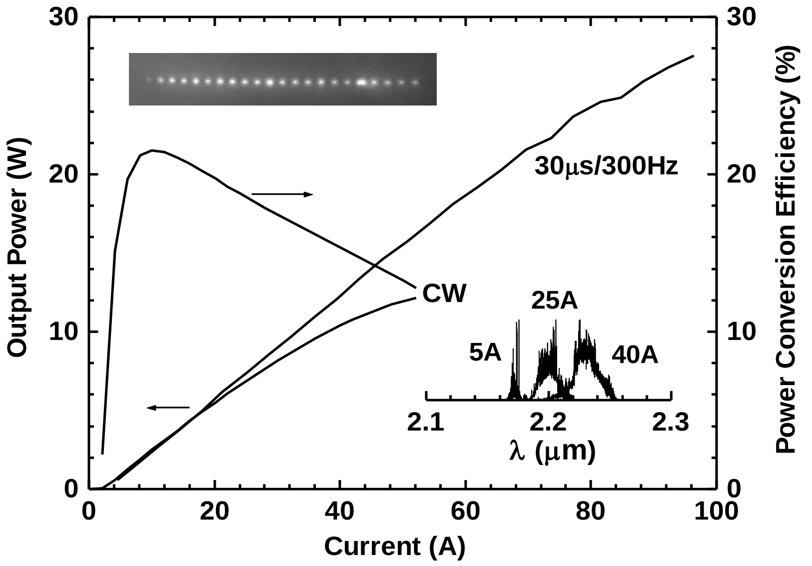

Figure 2.3 CW power and power conversion characteristics of 22 element 1-mm-long AR/HR coated laser array measured in CW and quasi-CW regimes at 17 °C. Insets show near field (top) and laser spectra (bottom).

2.3 3.1 μm diode lasers with asymmetric separate confinement heterostructure

This section discusses a novel approach of asymmetric separate confinement heterostructure aimed at improved device efficiency [41]. In the new heterostructure the strong carrier confinement in active GaInAsSb QWs is maintained by using AlGaInAsSb barriers but the separate confinement heterostructure is made out of different materials and is designed for minimized carrier recombination. The diode lasers emitting near 3.1 μm were fabricated following this approach. The devices with new design demonstrated factor of ~1.5 improvement of internal efficiency at RT. Both threshold current and slope efficiency became more temperature stable as confirmed by increased values of T_0 and T_1 parameters. The output power level was increased up to 220 mW CW at 17 ^{o}C for 100-μm-wide, 2-mm-long, AR/HR coated 3.15 μm multimode diode lasers.

2.3.1 Laser heterostructure and device fabrication

The laser heterostructure with new design was grown by MBE on Te-doped GaSb substrates in a Veeco GEN-930 modular system equipped with valved cracker cells for As and Sb. The same system was used for growth of laser heterostructure based on previous design and these devices serve as a reference in this work [42]. In both new and reference laser heterostructure all layers except for QWs were lattice-matched to the GaSb substrate. Figure 2.4 plots the calculated flat band diagrams of the reference (Figure 2.4 (a)) and new (Figure 2.4 (b)) laser heterostructure and highlights the important differences between them.

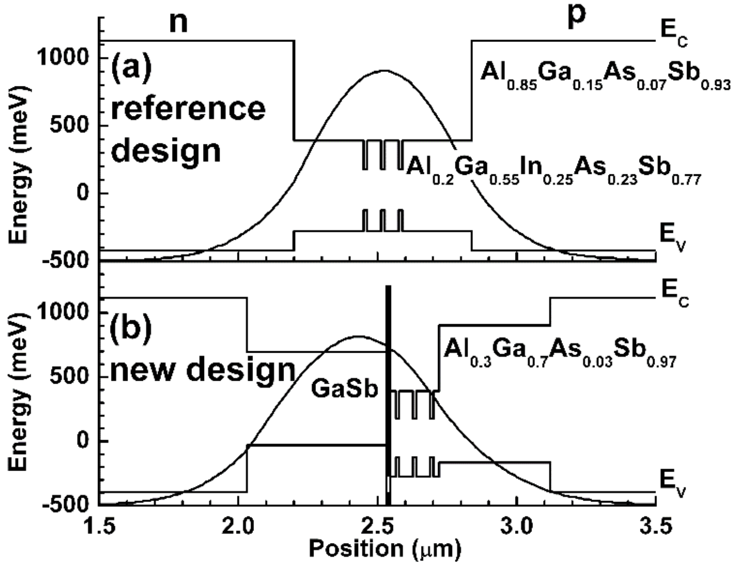

Figure 2.4 Schematic band alignment diagram and transverse near field distribution of (a) reference design with symmetric nonbroadened quinary AlGaInAsSb waveguide, and (b) new design with asymmetric broadened GaSb and quaternary AlGaAsSb waveguide used in this work.

The parameters for the calculations were taken from [37]. Details of the reference laser heterostructure can be found elsewhere [42]. In new laser heterostructure the waveguide claddings were made of $Al_{80}Ga_{20}As_{7}Sb_{93}$, doped with Te (n-side) and Be (p-side). Heavily doped seven-period $Al_{80}Ga_{20}As_{7}Sb_{93}$/GaSb superlattice (SL) was introduced between the n-GaSb substrate and n-cladding to assist electron transport. The hole transport into p-cladding was facilitated by introduction of a heavily doped graded bandgap layer between the p-cladding and p-cap.

The three-QW active region and waveguide core were nominally undoped. The three-QW active region designs of new and reference laser heterostructures were nearly the same, hence, both emitted near 3.1 µm. However, if in previous design the $A_{20}Ga_{55}In_{25}As_{23}Sb_{77}$ alloys were used for both the barriers and waveguide core layers, the new structure had different waveguide core design. Namely, the electrons travel from n-cladding to active region through 500 nm of GaSb while holes from p-cladding to active region were delivered through 400-nm-wide $Al_{30}Ga_{70}As_{1}Sb_{99}$ quaternary. Six-period InAs (12Å)/AlSb (12Å) SL between GaSb and active region acted as a hole stopper [43] while remained tunnel transparent for electron transport. It should be noted that GaSb-based type-I QW diode lasers with GaInAsSb/AlGaInAsSb QWs and symmetric AlGaAsSb separate confinement heterostructure (SCH) were reported [44]. Those device heterostructures did not utilize SL hole stopper, hence the recombination current in SCH was not suppressed.

The calculated near field patterns are shown in Figure 2.4. The refractive indices of individual layers were estimated following [39]. The refractive index of quinary $Al_{20}Ga_{55}In_{25}As_{23}Sb_{77}$ alloy was taken equal to that of GaSb (~3.8). This estimation is somewhat justified by the fact that both materials had nearly the same bandgap according to our photoluminescence studies. The measurements of the far field patterns and calculation of group modal refractive indexes from amplified spontaneous emission spectra performed for variety of diode lasers utilizing quinary waveguides also support the validity of this estimation. The effect of the QW dielectric permittivity on modal profile was neglected. As seen from the calculated modal profiles the intensity of the normalized electric field at the location of three-QW active region gets reduced in new laser heterostructure. This results into the reduction of the overall coupling between active region and optical mode by a factor of about 1.5 as compared to reference structure.

The wafers were processed into index-guided 100-µm-wide ridge lasers, by etching of the p-cladding material outside of the current stripes. Inductively coupled $H_2/CH_4/Ar$ plasma reactive ion etching process was utilized. Uncoated 1-mm-long devices were used for measurement of the modal gain and characterization of the temperature dependence of the laser threshold and efficiency. These measurements were performed in short pulse regime to minimize Joule heating. For the CW characterization, 2-mm-long devices with mirrors coated to reflect ~5% (AR) and ~95% (HR), were In-soldered epi-side down onto gold-coated polished copper blocks. The blocks were bolted to brass heatsink attached to Peltier cooler. The heat was removed by running water.

2.3.2 Results and discussion

Figure 2.5 shows the temperature dependence of the laser threshold and slope efficiency as measured in short pulse regime (100 kHz/200 ns) for 1-mm-long uncoated devices based on new and reference laser heterostructures. The devices based on new heterostructure demonstrated improved slope efficiency by the factor 1.3 at 300 K. The new design results into reduced threshold current at temperatures above 200 K. Decrease of the threshold currents and increased of the slope efficiency are accompanied by improved thermal stability of both parameters. It should be noted that the improved temperature stability characterized by increased values of both T_0 (from 33 to 43 K) and T_1 (from ~80 to ~110 K) was achieved without altering the active region electronic structure. Hence, one can conclude that the device parameters are not yet limited by fundamental considerations such as free carrier absorption and nonradiative recombination in active region.

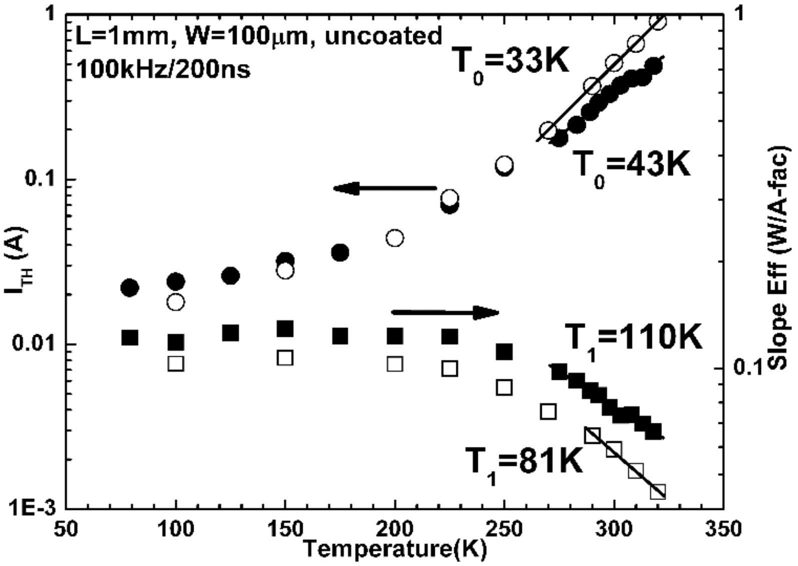

Figure 2.5 Temperature dependences of the threshold current (circle) and near threshold slope efficiency (squares) measured in pulse regime (100 kHz/200 ns) for 1-mm-long, 100-μm-wide uncoated devices. Solid symbols correspond to lasers with new heterostructure and open symbols correspond to devices with reference design.

Hakki-Paoli method [40] supplemented by spatial filtering optics was utilized to measure the current dependence of the laser modal gain spectra (Figure 2.6) to determine internal optical loss and calculate the internal efficiency. The total loss of about 25 cm^{-1} can be estimated from the long wavelength part of the modal gain spectra. The internal optical loss of about 13 cm^{-1} can be estimated assuming mirror loss of about 12 cm^{-1} for 1-mm-long uncoated devices. This value is about 5 cm^{-1} higher than what was previously measured for reference lasers [42]. Somewhat increased internal optical loss could be accounted by possible accumulation of holes due to energy barrier at the interface between active region and AlGaAsSb hole transport layer (Figure 2.4 (b)). This hole transport constraint can be eliminated by introduction of the compositionally graded layers in further design optimization efforts. Another, perhaps less probable, scenario is extra loss due to presence of residual p-doping in GaSb electron transport layer. Our calibration studies showed that nominally undoped GaSb demonstrate the p-type conductivity characterized by ~10^{16} cm^{-3} free holes concentration. It is not clear at the moment if the Al-containing waveguide core layers should be expected to have lower residual doping level.

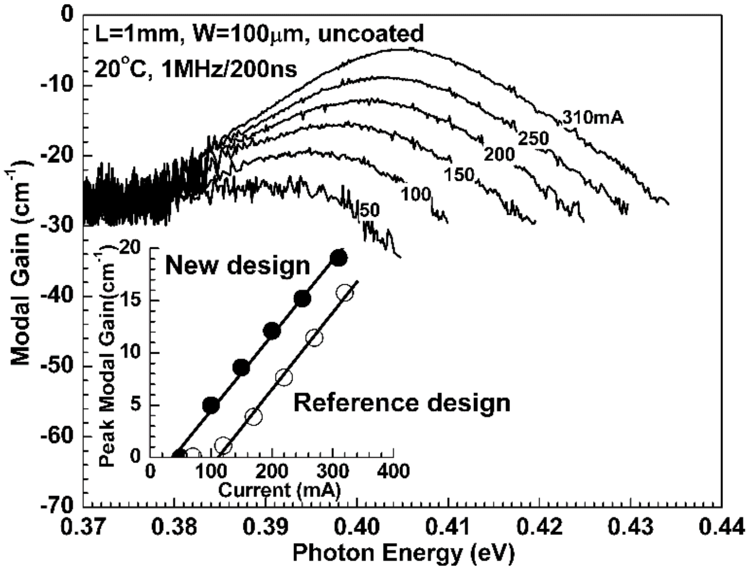

Figure 2.6 Current dependence of modal gain spectra measured for 1-mm-long 100-μm-wide uncoated devices at 20 °C. Inset shows current dependence of peak modal gain for new (solid circles) and reference (open circles) devices.

In the new laser heterostructure the recombination current through waveguide core layers (GaSb and AlGaAsSb) should be minimized. Higher electron mobilities in GaSb should lead to lower equilibrium carrier concentration. Moreover, InAs/AlSb SL stopper prevents hole injection into GaSb electron transport layer while large conduction band offset between active region and AlGaAsSb prevents electron injection into AlGaAsSb hole transport layer. Thus the carrier transport through waveguide core layers in new laser heterostructure is not of ambipolar type but rather monopolar in nature. The quantitative analysis should be based on detailed modeling but qualitatively this consideration can explain observed increase of the internal efficiency in lasers with new design. The estimation based on measured values of internal loss and slope efficiency values yields internal efficiency of about ~80% at 20 °C as compared to ~50% obtained with previous design.

Figure 2.6 plots the dependence of the peak modal gain on current for devices with new and reference designs. The transparency current decreases in devices with new design as can be expected with improved internal efficiency. The differential gain with respect to current remains nearly unchanged despite lower optical confinement factor in new laser heterostructure. This can be explained by nearly compensating effects of improved internal efficiency and reduced optical confinement.

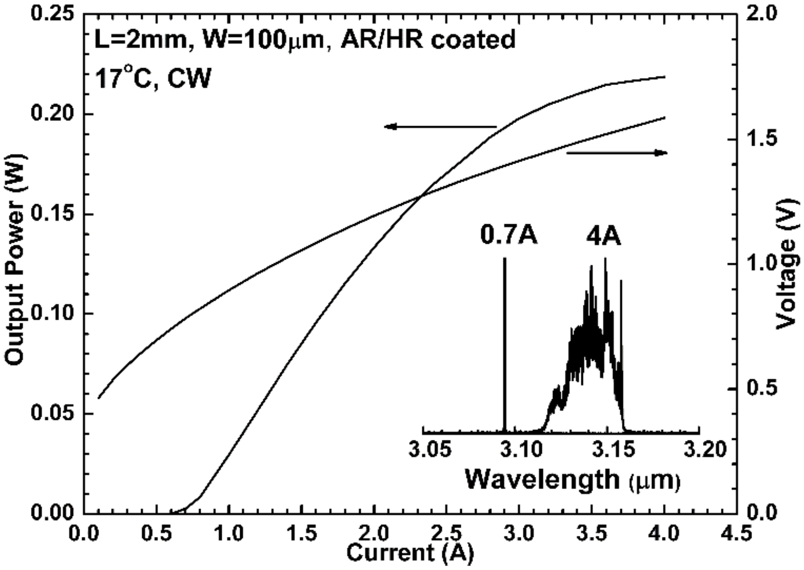

Figure 2.7 CW light-current and current-voltage characteristics of 2-mm-long AR/HR coated devices at 17 ℃. Inset shows the spectra at 0.7 and 4 A.

Figure 2.7 shows the CW light-current and current-voltage characteristics measured for 2-mm-long AR/HR coated devices with new design. The devices emitted 220 mW of CW output power at 4 A at 1.6 V at 17 ^{o}C. Threshold current density was ~350 A/cm^2. The laser spectra measured near threshold and at 4 A are shown in inset to Figure 2.7. The output power was limited by the thermal roll-over. The active region overheating is apparent from spectral red shift (inset to Figure 2.7). The input electrical power at maximum optical output was about 6 W and less than 1 W of input electrical power was required to obtain 25 mW of 3.1 μm output.

2.4 3.3 - 3.4 µm diode lasers with triple-layer GaInAsSb QWs

In this section we discuss modified design of the W-QW without InAs layers for GaSb-based diode lasers emitting 3.3 to 3.4 µm [45]. Diode lasers utilizing W-QWs made of quaternary GaInAsSb layers with 50% In but variable As composition were designed and fabricated. The devices with 10- and 12-nm-wide W-QW operated near 3.3 and 3.4 µm in CW regime at RT. It should be noted that diode lasers with active region based on 12-nm-wide standard type-I $Ga_{50}In_{50}As_{20}Sb_{80}$ QWs operate near 3 µm [28]. Type-I QW GaSb-based diode laser operation at wavelength near 3.3 µm or above required wider QWs with In composition above 55% [28]. Increase of the QW In content is associated with certain technological issues and also requires increase of the As composition leading to hole confinement degradation.

2.4.1 Laser heterostructure and device fabrication

Figure 2.8 illustrates the design of QWs and shows RT photoluminescence (PL) spectra measured for corresponding laser heterostructures. Figure 2.8 (a) shows calculated band diagram [37] of the 6-nm-wide 1.6% compressively strained $Ga_{50}In_{50}As_{23}Sb_{77}/Al_{20}Ga_{55}In_{25}As_{23}Sb_{77}$ QW used as a reference in this work. The laser heterostructure with these QWs showed photoluminescence (PL) peak near 2.55 µm at RT (~490 meV). Increase of the width of the QW to 12 nm led to PL red shift to ~ 2.9 µm, corresponding to bandgap reduction of ~65 meV. These 12-nm-wide QWs were used in development of the high power type-I cascade diode lasers reported in Ref. [46]. Figure 2.8(b) shows the calculated band diagram of the 3/6/3-nm-wide triple layer QW. The 3-nm-wide inserts have the same 50% In composition as central layer did but have As content increased to 32%. The exact As composition is hard to determine and the value provided corresponds to the best match between calculated and experimentally observed red shift. Laser heterostructures based on these triple layer QWs had peak PL near 3.1 µm, i.e.

bandgap was reduced by ~90 meV. Thus the use of the As-rich 3-nm inserts offers ~25 meV stronger bandgap reduction as compared to standard QW thickness increase. This is achieved by reduction of the energy of first quantized conduction band state on absolute energy scale. Further enhancement of the device operating wavelength can be achieved through reduction of the As composition of the central 6-nm-wide layer.

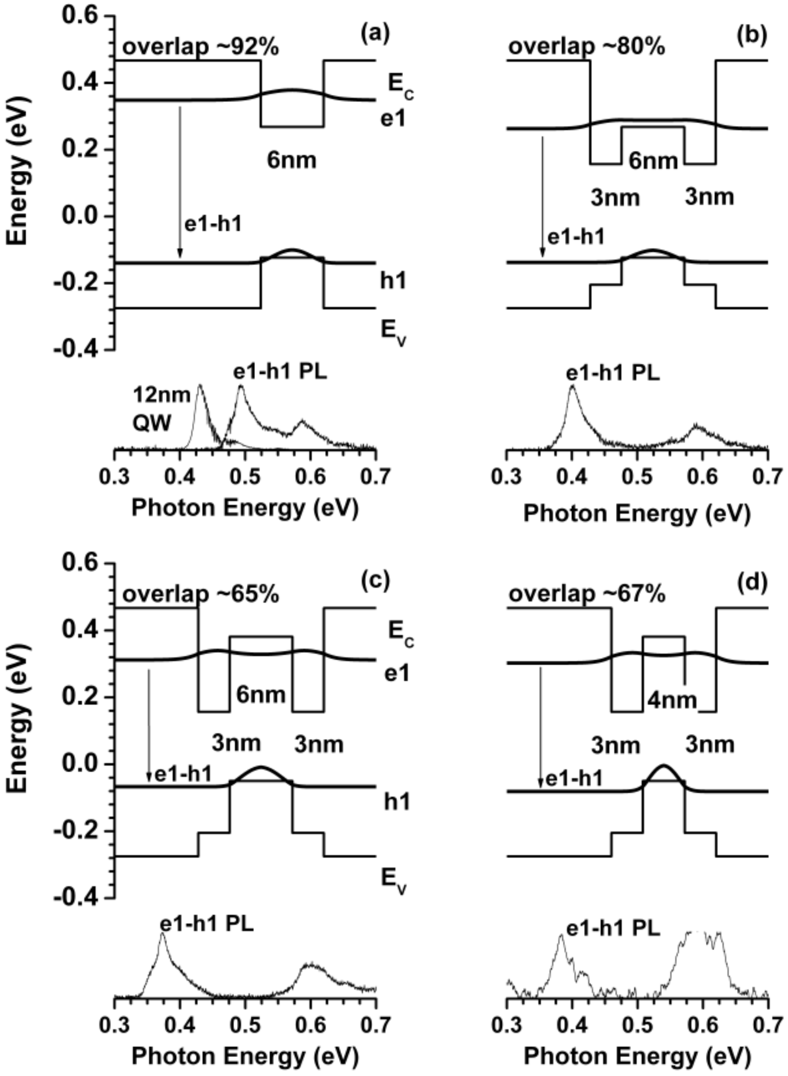

Figure 2.8 Flat band diagrams of QWs and the probability distributions functions corresponding to fundamental electron and hole states. The experimental RT PL spectra are shown for each laser structure. (a) 6 nm $Ga_{50}In_{50}As_{23}Sb_{77}$ - PL peak near 2.5 µm (PL of 12-nm-wide QW with same composition that peaks at ~430 meV is shown for comparison); (b) 6 nm $Ga_{50}In_{50}As_{23}Sb_{77}$ and 3 nm $Ga_{50}In_{50}As_{32}Sb_{68}$ - PL peak near 3.1 µm; (c) 6 nm $Ga_{50}In_{50}As_{15}Sb_{85}$ and 3 nm $Ga_{50}In_{50}As_{32}Sb_{68}$ - PL peak near 3.3 µm; (d) 4 nm $Ga_{50}In_{50}As_{15}Sb_{85}$ and 3 nm $Ga_{50}In_{50}As_{32}Sb_{68}$ - PL peak near 3.24 µm.

Figure 2.8 (c) shows corresponding band diagram with As content of the central section decreased down to nominally 15%. The upward shift of the first quantized valence band state is stronger that of the first quantized conduction band state resulting into reduced optical transition energy. The laser heterostructure based on the QWs from Figure 2.8 (c) demonstrated PL peak above 3.3 μm (~375 meV) at RT. Figure 2.8 (c) shows that both electron and hole confinement energies remain adequate, i.e. similar to those used in 2.9 – 3 μm emitting devices [28]. Standard 12-nm-wide QWs with In content above 55% designed to operate near 3.3 μm have degraded hole confinement barriers due to necessarily increased As composition [28]. It should be noted that utilization of highly strained (~2%) $Ga_{50}In_{50}As_{15}Sb_{85}$ layers for extension of the device operating wavelength above 3 μm is only possible in triple-layer configuration illustrated in Figure 2.8 (c) because of critical thickness considerations.

These modified W-QWs do not have the barriers for hole transport that are present in classical InAs/GaInSb/InAs W-QWs, hence, uniform pumping of multiple QW active region can be achieved more easily. Figure 2.8 (d) shows the band diagram of the 3/4/3-nm-wide QW with the same layer compositions as in QW shown in Figure 2.8 (c). The laser heterostructure with these QWs in active region demonstrates PL near 3.24 μm — a better match for methane absorption line. Thus, like in classical InAs/GaInSb/InAs W-QW design, the fine tuning of the laser operating wavelength is conveniently achieved without changing of the layer composition. One of the penalties for this convenience is reduced overlap of the electron and hole envelope functions in type-II QWs as compared to type-I ones. Rough estimations based on Figure 2.8 calculations predict up to ~40% reduction of the maximum optical gain in triple layer W-QW as compared to wide single layer standard QW. This can lead to reduction of the differential gain with respect to current followed by increase of the threshold current density. The PL peak near

2.1 µm (~590 meV) shown in Figure 2.8 (d) is from other layers rather than QWs, and will be discussed elsewhere. No emission of 2.1 µm is observed from the devices.

2.4.2 Results and discussion

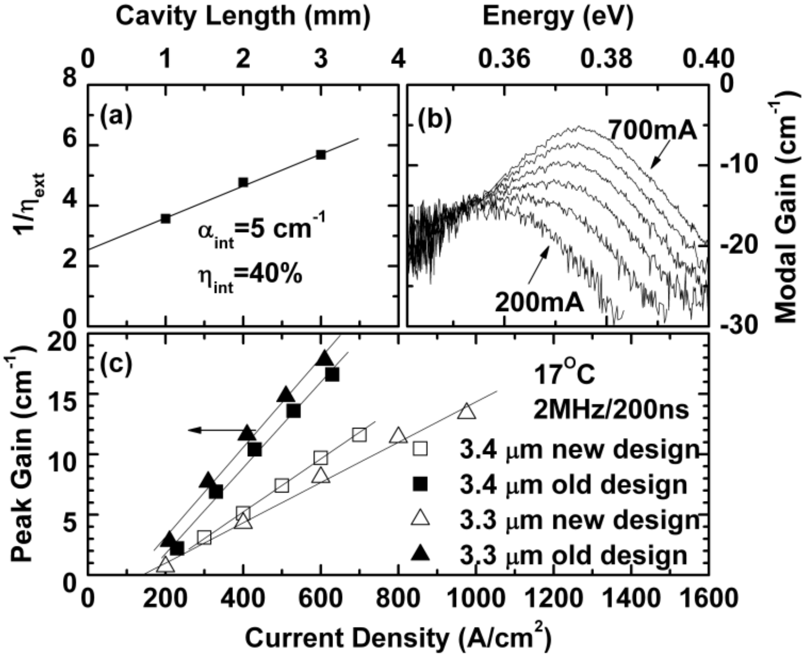

Figure 2.9 Characteristics of modal gains of 3.3 and 3.4 µm devices. (a) Plot of 1/ηext as a function of cavity length L and (b) dependences of current density on the modal gain spectra for 3.4 µm devices. (c) Dependences of current density on the peak modal gain for 1-mm-long uncoated devices measured at 17 ℃ in pulsed excitation mode (2 MHz/200 ns).

Wide ridge dielectric confined diode lasers based on the triple layer W-QWs shown in Figure 2.8 (c) and (d) were designed and fabricated. The devices had laser heterostructure similar to one described in Ref. [41]. The active region of these 3.3 and 3.4 µm lasers contained three W-QWs. The asymmetric laser heterostructure [41] has about 15% and 30% smaller optical confinement as compared to standard symmetric laser heterostructure used in previously reported 3.3 µm and 3.4 µm diode lasers [28], respectively. The modified laser heterostructure is used for studies of the effect of waveguide design on laser optical loss, injection efficiency and beam shape which are not subject of this work and will be discussed elsewhere.

The internal optical loss of the devices reported in this work were estimated from modal optical gain spectra measured by Hakki-Paoli technique [40] (Figure 2.9 (b)) and from cavity length studies for 3.4 µm diode lasers (Figure 2.9 (a)) (1-, 2- and 3-mm-long uncoated lasers were tested) and amounted to about 5 cm^{-1}. Figure 2.9 (c) plots the current dependence of the peak modal gain for 3.3 and 3.4 µm diode lasers based on W-QWs active regions. For comparison the dependences measured for previously reported [28] 3.3 and 3.4 µm devices with symmetric waveguide and standard wide QWs are shown. As expected the differential gain is reduced about twofold in lasers based on W-QWs due to combined effect of the reduced optical confinement and reduced overlap of the electron and hole envelope functions. The reduced differential gain leads to increase of the threshold current density at 17 °C from 600 – 700 A/cm^2 in devices with standard QWs [28] to 800 – 900 A/cm^2 in devices based on W-QWs. The parameter T_0 characterizing exponential increase of the threshold current density with temperature as measured for 1-mm-long uncoated lasers with W-QWs was about 38 and 33 K in temperature range from 15 to 35 °C for 3.3 and 3.4 µm lasers, respectively.

Figure 2.10 plots the power-current characteristics of the epi-down mounted diode lasers based on W-QW active region. Devices based on QWs shown in Figure 2.8 (d) emit near 3.3 µm and demonstrate CW output power above 50 mW per 50-µm-wide aperture at 17 °C. The cavity length was 3-mm-long and neutral/high (NR/HR) reflection coating was utilized. The devices based on QWs shown in Figure 2.8 (c) emitted near 3.4 µm and generated above 30 mW per 100-µm-wide aperture for NR/HR coated 3-mm-long cavity. Despite increased threshold current densities the devices demonstrated somewhat improved maximum CW output power levels as compared to those reported for devices based on standard standard type-I QW active region, namely ~50 and ~30 mW per 100-µm-wide stripe at 3.3 and 3.4 µm [28], respectively. Among possible reasons are reduced values of internal loss that allowed using longer cavity length (3 mm versus 2 mm) with improved thermal footprint. In short pulse regime with minimized Joule heating the devices can operate more efficiently with 1-mm-long cavities and more than 400 mW of power was produced from 100-μm-wide aperture by device based on QWs shown in Figure 2.8 (c).

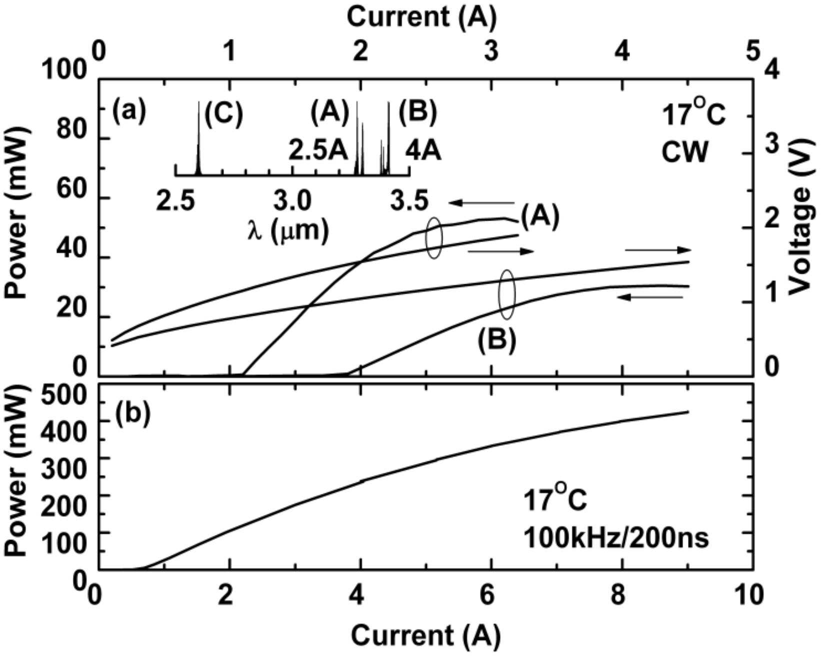

Figure 2.10 Characteristics of modal gains of 3.3 and 3.4 μm devices. (a) Plot of 1/ηext as a function of cavity length L and (b) dependences of current density on the modal gain spectra for 3.4 μm devices. (c) Dependences of current density on the peak modal gain for 1-mm-long uncoated devices measured at 17 ^{o}C in pulsed excitation mode (2 MHz/200 ns).

2.5 Conclusion

In this chapter, we have discussed the novel design and heterostructure optimization on GaSb-based single stage diode lasers in the spectral range of 2.2 to 3.4 μm, and these devices demonstrated improved performance.

High power individual 2.2 μm GaSb-based type-I QW diode lasers and linear laser arrays from the same material have been designed and fabricated. Individual devices generate 1.6 W CW output power from a 100-μm-wide aperture. A linear laser array containing twenty-two 100-

μm-wide elements generates 12 W in CW operation and 27 W in quasi-CW operation. PCE peaked above 20 % and remained above 10 % at the maximum CW output power levels. Lasers demonstrate threshold current densities below 100 A/cm^2 competing with the best numbers obtained for diode lasers at any wavelength. The devices demonstrate excellent temperature stability. The performance improvement was achieved using heavy compressive strain in the relatively narrow QWs in active region with maximized carrier confinement. The results demonstrate the compatibility of the design approach with high power diode laser fabrication.

The internal efficiency of the 3.1 μm emitting GaSb-based type-I QW diode lasers was increased by a factor of 1.5 at RT. This was achieved by elimination of thick quinary AlGaInAsSb layers from laser heterostructure. The new separate confinement heterostructure utilized electron and hole stopper layers minimizing the carrier recombination current outside of active QWs. The design modification improved values and thermal stability of both threshold current and efficiency at RT. The devices with new design demonstrated increased CW output power level of 220 mW at 3.15 μm at RT. The proposed design modification is applicable to GaSb-based type-I QW diode lasers emitting at any $\lambda > 3$ μm since active region remained intact as compared to previous generation of devices. The improvement of device parameters and their thermal stability without changes in electronic structure of the active QWs confirms that current state-of-the-art GaSb-based diode lasers are not fundamentally limited.

3.3 - 3.4 μm diode lasers with W-QW were designed and fabricated. The type-II band alignment was utilized to obtain laser operation at wavelength above 3.3 μm without increase of the In and As content and related loss of the hole confinement. The W-QW based on GaInAsSb layers with the same In and different As compositions allowed eliminating the parasitic barriers for hole transport often present in InAs/GaInAs/InAs W-QW design leading to uniform pumping of the triple-QW active regions. The devices operated in CW regime at RT demonstrated output power levels comparable or better than those previously obtained with standard single layer type-I QWs.

Chapter 3 Cascade Diode Lasers Emitting in 2.4 - 3.3 µm

3.1 Introduction

Semiconductor lasers emitting in mid-infrared spectral region are highly in demand for variety of applications ranging from molecular spectroscopy to medical treatments. After half century of exploration, there are three competing approaches for semiconductor heterostructure lasers in the mid-infrared region been developed at present, known as quantum cascade lasers (QCLs), interband cascade lasers (ICLs), and diode lasers (DLs).

3.1.1 QCLs and ICLs

The cascade pumping concept has been achieved on QCLs and ICLs. The first QCL was demonstrated in Bell Labs [47] in 1994, based on the concept of inter-subband transition in a biased SL, which was originally proposed for light amplification by R. Kazarinov and R. Suris in 1971 [48]. The inter-subband or intraband transition of carriers, usually electrons, enables the generation of photons with energy of the difference between sub conduction bands, which is independent of the band gap. The cascade design of the QCL structure allows one carrier to travel through numerous inter-subband gain sections, and emit multiple photons. Thus, the quantum efficiency of QCLs could be higher than 1, and the cascade pumping concept eventually resulted in CW RT operation of these lasers. Watt-level output power values were obtained with InP-based QCL heterostructures for wavelength above 3.5 µm [33, 49]. However, the extremely fast relaxation process brings strong intersubband optical phonon scattering, resulting in a relatively low efficiency of each active stage and high threshold current for lasing, and the miniband alignment of multiple cascade stages demands quite high driving voltage. All these factors lead to large power consumption, high heat dissipation, and low power conversion efficiency, which obstruct the application of QCLs in some power-efficient circumstances.

Besides, it is difficult for QCLs to reach the spectral range below 3.5 µm with good CW performance in RT, due to the limited conduction band offset for the material system of GaInAs/AlInAs/InP [49].

The ICL is a good option for the spectral range of 3.4 – 4.0 µm. The ICL employed the spatially indirect inter-band transition, which was originally introduced by R. Yang in 1995 [50], in type-II gain sections (InAs/GaInSb) [32]. Although the idea of indirect interband transition was inspired by QCLs, and the format of multiple photons generation from one electron is analogous to that of the QCL, their mechanisms of photon generation are distinct. In ICLs, both electrons in conduction band and holes in valence band of the active QWs are involved in the interband transition, while the holes are absent in the inter-subband transition of QCLs. The GaSb-based type-II QW ICLs utilizing efficient band-to-band tunneling for cascade pumping of bipolar gain sections[50] are characterized by fundamentally lower input threshold power levels. The maximum CW RT power reported for ICLs was about 470 mW near 3.7 µm [32]. But, because of the recombined electrons and holes are not located in the same layer in ICLs, this spatial mismatch simply reduces the overlap of carriers' wavefunctions, and therefore impair laser efficiency and performance. The W-QWs formed by adding the second InAs layer on the other side of QWs, which is a nowadays popular design for ICLs, nevertheless increase the wavefunctions overlaps up to ~70%.

3.1.2 Cascade scheme on GaSb-based type-I QW diode lasers

In the spectral range of 1.9 – 3.4 µm, QCLs and ICLs are not competitive, while the GaSb-based type-I QWs diode lasers are the best solution, owing to the excellent performance, compactness and efficiency. The GaSb-based type-I QWs diode lasers fulfill the CW RT operation gap in the spectral range of 2 – 3.2 µm, which was left by the modern GaAs- and InP-based type-I QWs diode laser technology producing CW $\lambda < 2.2$ μm in RT [51, 52], and the QCLs and ICLs producing CW $\lambda > 3.5$ μm in RT [32, 33, 49]. The best performance of GaSb-based type-I QW single-stage diode lasers operating between 1.9 – 3.4 μm generate up to 1.5 W per 100-μm-wide stripe in spectral region from 1.9 to 2.2 μm and 25 – 350 mW in spectral region 2.9 to 3.4 μm[28].

Conventionally, the heterostructure of the GaSb-based type-I QW diode lasers consist of an active region sandwiched by waveguide layers and adjacent cladding layers. The waveguides energetically confine both electrons and holes in the exactly same QW layers, and have higher refractive index than the claddings. Thus, this heterostructure design has perfect symmetric confinement on both carriers and photons simultaneously in the active region. The spatial wavefunction overlaps of electrons and holes are maximized, and so is the optical confinement factor over QWs, resulting in a high optical gain. It is a huge benefit from type-I diode lasers, which cannot be achieved in QCLs and ICLs. In the past decades, a lot of efforts were made to improve the efficiency and performance of GaSb-based type-I QWs diode lasers. Highly compressive strain in the active region applied to 2.2 μm lasers with broadened waveguide insured low threshold current density and high differential gain by reducing the hole density of state and increasing hole confinement in QWs [30]. The utilization of quinary AlGaInAsSb barriers [16], leading to increased valence band discontinuities in GaInAsSb QWs, allowed the RT CW operation for 3.0 to 3.4 μm lasers with record output power [28]. The low density of states and high optical gain of the narrow bandgap compressively strained type-I QWs resulted into low threshold current densities of about 200A/cm^2 at 20 ^{o}C for 3 μm lasers. However, the quinary alloy impedes carriers transport, presumably because of the low mobilities and low carrier lifetimes in this material. Thus, the broadened waveguide design, which successfully reduced the internal optical loss for GaSb-based diode lasers below 2.7 µm, cannot be applied to the quinary waveguide. Aiming at this issue, a broadened asymmetric waveguide of GaSb and quasi-ternary AlGaAsSb alloy was introduced for 3.1 µm lasers, improving the internal efficiency and output power [41]. In addition, the design of triple-layer GaInAsSb QWs combined with the asymmetric GaSb/AlGaAsSb waveguide realized the fine adjustment of laser operating wavelength above 3.3 µm with decent output power by independent control of the effective electron and hole QW widths [45].

In spite of all these endeavors of enhancing lasers efficiency and performance, there are several limitations from the fundamental physics facts. The free carrier absorption (mainly intervalence band absorption) is increased as the wavelength increased from 2 to 3 µm [53], so does the Auger recombination [54]. These negative factors to laser performance cannot but eliminated by optimization on heterostructure of single stage diode lasers and the CW output power in RT is restricted far below watt level for the GaSb-based type-I QWs single stage didoe lasers emitting 3 µm and above.

In this situation, cascade pumping scheme can be an effective solution to boost the performance of type-I QWs diode lasers. As the successful experience in QCLs and ICLs, the cascade pumping can realize an internal efficiency above 1 by recycling the injected carriers between gain stages. By combining the cascade pumping with type-I QWs, it is a tremendous advantage to exploit the high optical gain and over 100% internal efficiency at the same time. Moreover, the series stacking of multiple gain sections can optimize the waveguide structure to eliminate the carriers transport issue in quinary alloy, and minimize the optical mode overlap on claddings, as well as the threshold current can be decreased, and the temperature sensitivity will be improved.

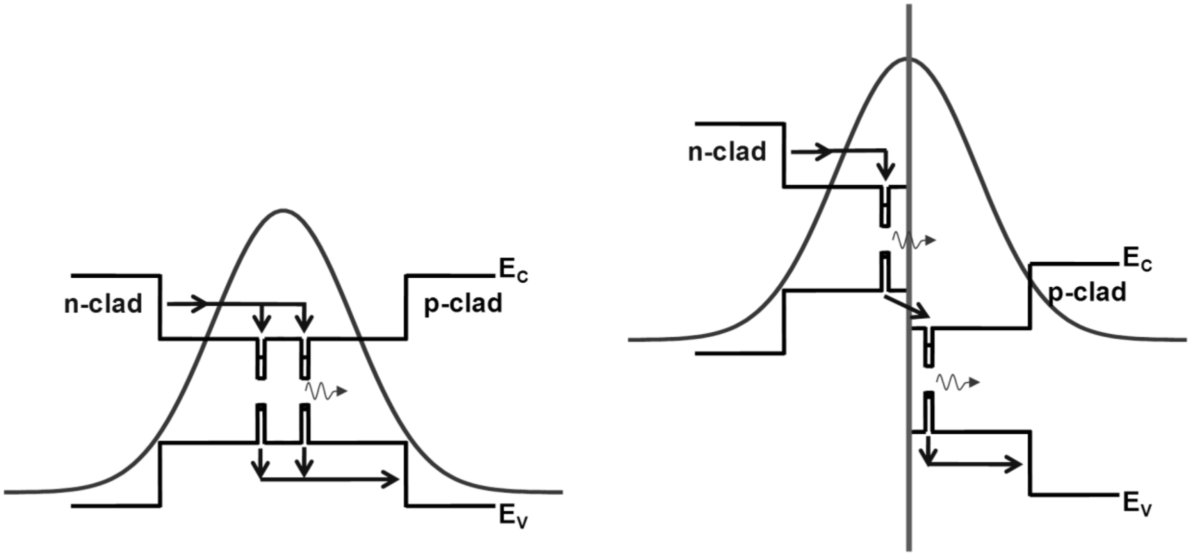

(a) (b)

Figure 3.1 (a) Generic band diagram of the type-I QW diode laser in which two QWs are connected in parallel, and (b) illustration of the hypothetical heterostructure design connecting QWs in series.

Device performance enhancement expected from cascade pumping of the type-I QW gain section is schematically illustrated by Figure 3.1. Figure 3.1 (a) shows generic laser heterostructure with double-QW active region overlapped with corresponding near field pattern. Ambipolar electron/hole transport through separate confinement heterostructure (SCH) layers pump type-I QWs to produce enough gain to compensate for cavity loss. Two QWs can be thought of as connected in parallel taking one half of the pumping current each. Figure 3.1 (b) shows hypothetical type-I QW laser heterostructure in which electron and hole stoppers are placed in between of QWs thus eliminating possibility of their parallel connection. In this pumping scheme the charge carriers can be exchanged between QWs only by means of band-to-band tunneling. This situation corresponds to series connection of two QWs. Given the same intensity of the optical field at location of QWs and ignoring the possible optical loss penalties the Figure 3.1 (b) design is expected to result into twofold reduction of the threshold current and twofold increase of the slope efficiency as compared to Figure 3.1 (a) case.

The voltage drop across laser heterostructure will increase but less than twofold. Extra voltage would be required to establish drift-diffusion transport through two SCH connected in series. However, voltage drop associated with carrier delivery through cladding layers to SCH would remain the same as in case of the standard diode lasers. This in combination with reduced threshold current should lead to increase of the peak PCE. Moreover, the series connection of the QWs should result into improved PCE at high output power levels due to increased laser slope efficiency. Increase of the number of the gain stages above two is expected to lead to further improvement. PCE equations

Enhancement of the device efficiency by connecting two GaAs-based type-I QW laser heterostructures in series was reported [55-58], but so far no success attempts had been achieved for GaSb-based type-I QWs edge emitting devices with decent CW output power in RT, because of either excessively high voltage, or extra optical loss caused by high doping in tunnel junctions, or the waveguide was not well designed for coherent light nor fundamental mode operation for edge emitters.

In work [55], two complete laser heterostructures each with its own waveguide core and claddings were connected in series by means of Esaki tunnel junction reinforced by QW. Two gain stages were operating as individual uncoupled and, hence, incoherent lasers limiting the devices brightness. This design approach is adequate when the efficiency of surface emitting light emitting diode (LED) needs to be increased since LED is inherently incoherent source [59]. The operating voltage of the double-laser or double-LED heterostructures devices increased more than twofold as compared to reference single stage devices due to voltage drop across tunnel pn-junction.

Utilization of the Esaki tunnel junction to accomplish true cascade pumping of two InP-based type-I QW gain stages coupled to the same optical mode was realized [56]. High operating voltage and/or high absorption loss associated with doped but relatively wide bandgap tunnel junction overcame the benefit of carrier recycling and no CW RT operation was demonstrated. GaSb-based vertical cavity surface emitting lasers (VCSELs) with two-stage cascade design and emitting near 2.3 μm [58], and InP-based VCSELs with five-stage cascade design 1.54 μm [57] were reported. The cascade pumping of the gain stages was achieved by utilizing heavily doped (10^{19} cm^{-3}) p++-GaSb / n++-InAs tunnel junction. The tunnel junction was placed at the node of the optical field in order to minimize the detrimental effect of the strong absorption on device threshold and efficiency. This approach is not efficient for development of the high power edge emitting lasers since it would necessitate the device operation at higher order transfers modes producing multiple-lobe divergent far field patterns.

In this chapter, we discuss a novel design of cascade pumping GaSb-based diode lasers based on type-I QWs, demonstrating high CW power edge emitting in fundamental transfer mode at RT. The broken gap or type-III band alignment of GaSb/InAs [50], which usually does not require large bias or heavy doping [32] can provide efficient cascade injection. This tunnel junction of GaSb/InAs is ideal to be applied to GaSb-base diode lasers, thanks to the perfect lattice matching. The doping of GaSb/InAs tunnel junction is moderate and only in InAs layers. Therefore, there is no excessive optical loss caused by absorption, and the lasers are working in fundamental mode, despite that the tunnel junction is located at the peak of the fundamental optical mode.

Based on this design, two-stage cascade type-I QWs diode lasers of 2.4 - 3.3 μm were grown and fabricated. The two-stage cascade pumping scheme led to twofold increase of the slope efficiency, and boosted the CW RT output power levels and enhanced the laser efficiency, as compared to the conventional single-stage diode lasers. 3 µm AR/HR coated lasers with 100-lm-wide aperture and 3-mm-long cavity generated 590 mW of CW output power at RT. Furthermore, the threshold current density and improve device efficiency could be improved by increasing the QW optical confinement factor in the two stage diode laser with optimized cascade heterostructure by eliminating the separations between the QWs and the electron injector, as well as reduced QW numbers. The success of optimized cascade structure lead to the implementation of first GaSb-based type-I QWs cascade diode lasers with three active stages, demonstrating record quasi-watt level (960mW) CW output power in RT at 3 µm.

3.2 3 µm diode lasers with two-stage cascade pumping scheme

The first successful design of the two-stage cascade GaSb-based type-I QWs diode laser heterostructure was achieved on 3 µm emitting lasers [46]. Twofold increase of the slope efficiency was obtained as compared to the reference 3 µm single-stage diode lasers. AR/HR coated lasers with 100-lm-wide aperture and 3-mm-long cavity generated 590 mW of CW output power at RT.

3.2.1 Laser heterostructure and device fabrication

Figure 3.2 shows the schematic flat band diagram of single stage GaSb-based type-I QW diode laser heterostructure with calculated transverse near field intensity distribution. The active region contained two 12-nm-wide GaInAsSb QWs with In content of 50% and compressive strain of 1.6%. The QWs were spaced by 50 nm of barrier $Al_{20}Ga_{55}In_{25}As_{24}Sb_{76}$ quinary alloy and 250-nm-wide layers of the barrier alloy were added on both sides of double-QW active. This laser demonstrated CW RT output power of 360 mW near 3 µm in multimode beam [28]. The CW operation of diode lasers near and above 3 µm was achieved after the quinary AlGaInAsSb barrier material was introduced to improve hole confinement in GaInAsSb QWs [16]. The low density of states and high optical gain of the narrow bandgap compressively strained type-I QWs resulted into low threshold current densities of about 200 A/cm^2 at 20 °C for 3 μm lasers despite dominant role of Auger recombination. The parameter T_0 characterizing the exponential increase of the threshold current with temperature was ~50 K and device internal efficiency was ~50% at 20 °C.

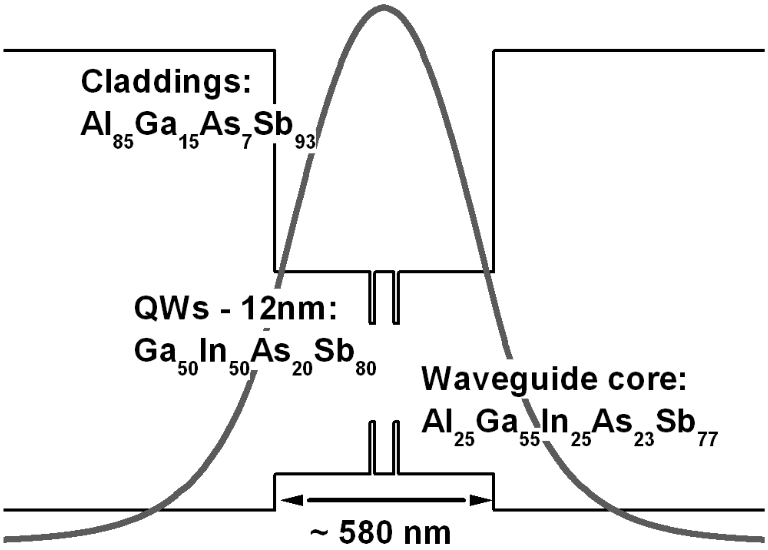

Figure 3.2 Schematic flat band diagram of the λ ~ 3 μm standard single stage type-I QW GaSb-based diode laser heterostructure [28]. The calculated fundamental mode is shown.

Figure 3.3 shows schematic band diagram of the laser heterostructure. The heterostructure contained two optical gain stages. The structure of each gain section was nominally the same as that of single-stage 3 μm lasers, which has two 12-nm-wide GaInAsSb QWs with an Indium concentration of ~50% that yields a compressive strain of ~ 1.6%. Note that neither waveguide core thickness nor locations of the double-QW gain sections have yet been optimized to maximize optical confinement factor.

The electrons are injected from $Al_{80}Ga_{20}As_7Sb_{93}$ n-cladding (left in Figure 3.3) into the GaInAsSb QWs of the first gain section. The electron-hole recombination in the QWs of the first gain section is followed by interband tunneling which transfers the electrons from the valence band states of the first gain section to the conduction band states of the second band section. The interband tunneling process takes place at the tunnel junction located in the center of the waveguide core (insert to Figure 3.3). Tunnel junction/injector was made of 10-nm-thick GaSb layer and ~25-nm-thick chirped AlSb/InAs SL similar to the one described in reference [32]. The AlGaAsSb 100-nm-wide graded composition layer was introduced after the first gain section to stop the electron and to promote the hole transport. Chirped AlSb/InAs SL stopped hole transport from and promoted the electron transport to the second gain section.

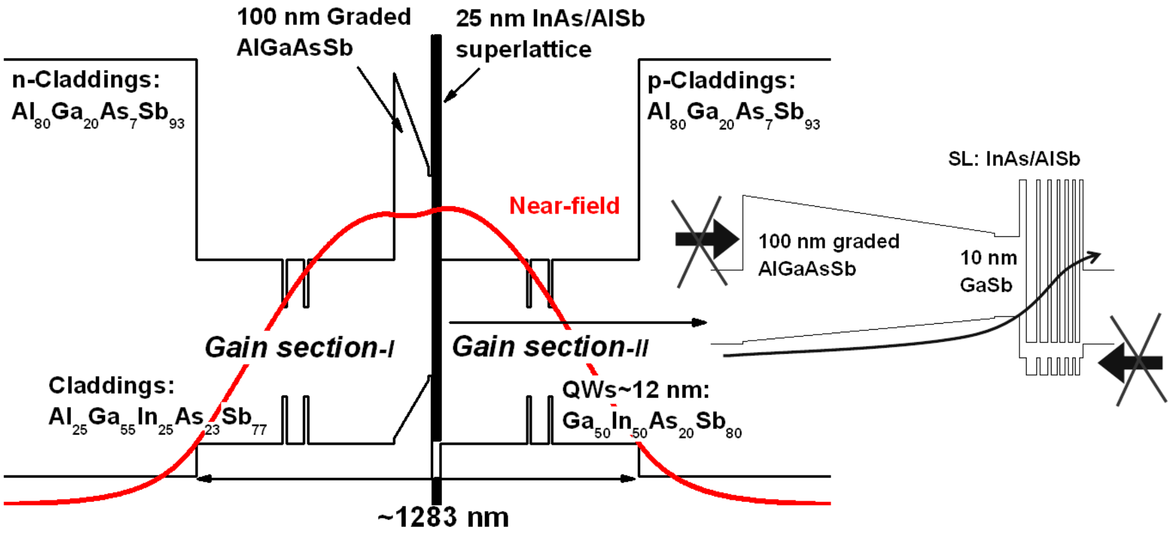

Figure 3.3 Schematic flat band diagram of the cascade pumped two-stage type-I QWs GaSb-based diode laser heterostructure. The calculated fundamental mode is shown. The inset shows the details of the electron/hole injector design.

The wafer was processed into multimode diode lasers with 100-µm-wide Si_3N_4-confined current stripes. The top contact and p-cladding material was wet etched outside of the current stripes. The uncoated 1-mm-long devices were indium soldered epi-up for pulsed characterization (200 ns/100-1000k Hz). The AR/HR (~5% and ~95%) coated 2-mm-long devices were indium soldered epi-down for characterization in CW regime.

3.2.2 Results and discussion

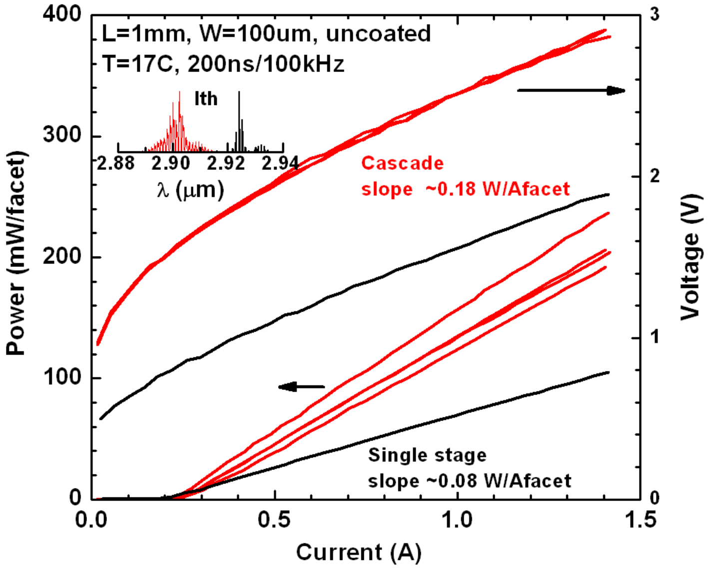

Figure 3.4 Light-current-voltage characteristics measured at 17 °C in short pulse regime (200ns/100kHz) for two-stage cascade lasers and reference single-stage lasers [28].

Figure 3.4 shows the light-current-voltage characteristics measured in pulsed regime at 17 °C for two-stage cascade lasers together with corresponding characteristics of the single-stage standard diode laser from Ref. [28]. The two-stage cascade lasers demonstrated twofold improvement in the slope efficiency and have similar (about 20% higher) threshold current as compared to single-stage reference devices. The voltage drop across two-stage cascade laser heterostructure increases by less than 1V. The increase of the device operating voltage by roughly the bandgap of the barrier material with each added gain section is expected. This is required to arrange for drift-diffusion carrier transport through barrier layers in each gain section. The rearrangement of the electron and hole injector structures to provide for direct delivery of the electrons from valence band state of the QW of the first gain section to conduction band state of the QW of the second gain section can minimize the voltage increase. However, this may compromise the carrier confinement in active QWs and, thus, can dilute the advantage of the high optical gain of the type-I QWs [13].

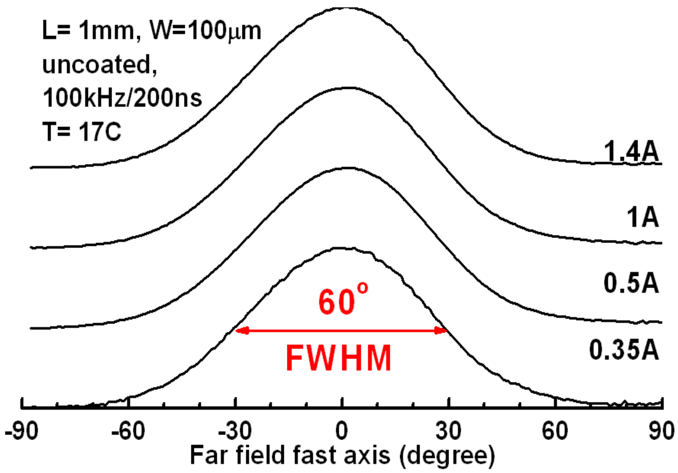

Figure 3.5 Fast axis far field patter measured at several currents above threshold.

It should be noted that the waveguide heterostructure of the two-stage cascade diode laser (Figure 3.3) support two modes. The fundamental mode (shown in Figure 3.3) has maximum coupling to tunnel junction/injector but less than 5% overlap with p-cladding (known source of absorption loss in diode lasers). The first mode (not shown in Figure 3.3) is characterized by almost four time stronger overlap with p-cladding but has almost zero coupling to tunnel junction/injector. Optical confinements with active QWs for both modes are nearly the same. Figure 3.5 plots fast axis far field patters measured for several currents above threshold. The fast axis far field corresponds to single fundamental mode operation. Hence one can conclude that fundamental mode wins mode competition due to lower optical loss despite strong interaction with tunnel junction/injector.

Figure 3.6 (a) plots the current dependence of the modal gain spectra measured by Hakki-Paoli technique [40] for twostage cascade lasers. The internal optical loss estimated from long-wavelength part of the gain spectra amounted to about 8 cm^{-1}. This value is by 4 cm^{-1} higher than that reported for single-stage lasers [28]. Even if the presence of the tunnel junction/ electron injector is solely responsible for internal optical loss increase this increase is not prohibitively high and well overcome by improved internal efficiency (Figure 3.4).

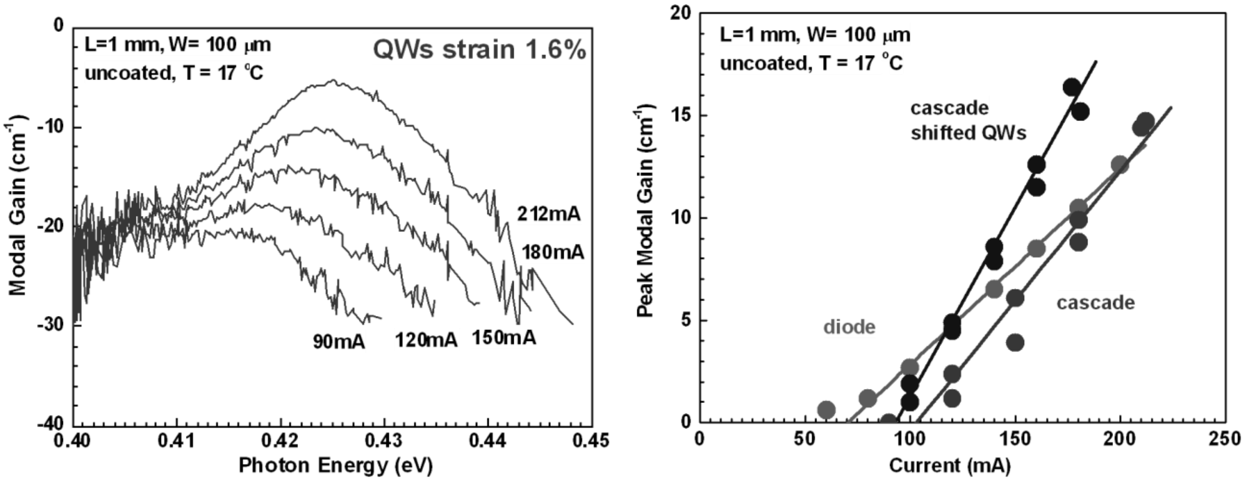

(a) (b)

Figure 3.6 (a) Modal gain spectra measured by Hakki-Paoli method for two-stage cascade laser at different current below threshold.; (b) Current dependences of the peak modal gain for two-stage cascade lasers and reference single-stage laser [28].

Figure 3.6 (b) shows the corresponding current dependence of the peak modal gain (marked “cascade”). Both transparency current and differential gain are similar to those obtained for single-stage lasers [28] (marked “diode”). The transparency current remains nearly unchanged since each double-QW active region should reach transparency condition at nominally the same current as in case of the single-stage lasers. The calculated overall optical confinement factor for fundamental transverse mode remains nearly the same for both single-stage lasers with waveguide width of about 580 nm (Figure 3.2) and two-stage cascade lasers with about twice wider waveguide core (Figure 3.3). Thus despite the injected carriers are recycled in the cascade devices the differential gain is expected to remain nearly the same as in case of single-stage lasers due to roughly twice lower optical field intensity at the location of the double-QW gain sections. Clearly, in optimized design with, for instance, single QW gain stages and maximized optical confinement factor one could expect reduced threshold current density.

Figure 3.6 (b) also shows the current dependence of the peak modal gain for somewhat optimized two-stage cascade laser heterostructure (marked “cascade, shifted QWs”). These data were obtained for lasers with heterostructure similar to one shown in Figure 3 but with modified waveguide width (reduced to ~930 nm) and QWs shifted closer to tunnel junction/injector (50-nm- versus 250-nm-spaced). This modified laser two-stage cascade heterostructure is characterized by about 40% improved optical confinement factor as compared to that of shown in Figure 3.3. The calculated improvement of the optical confinement factor is reflected closely in the experimental value of the increased differential gain with respect to current. Thus one can conclude that optical confinement factor as well as differential gain of novel cascade diode laser heterostructures can be increased by straightforward design optimization of the waveguide structure.

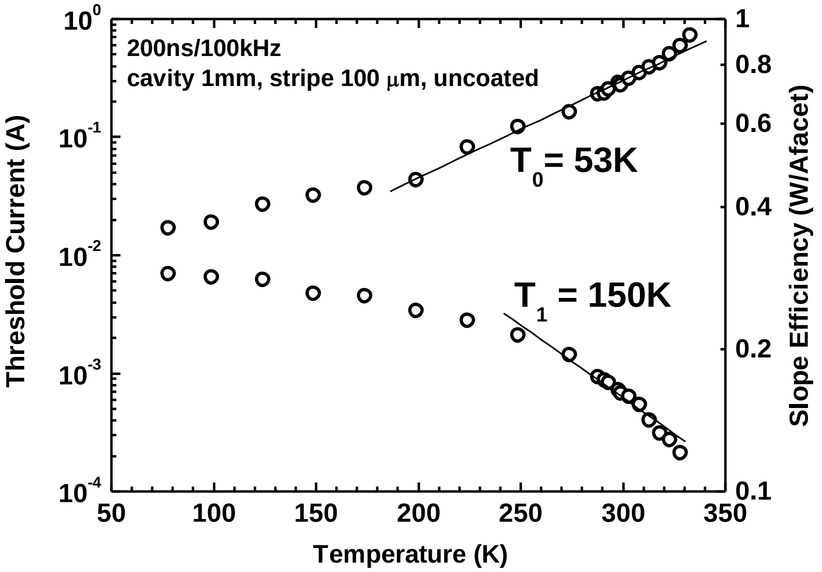

Figure 3.7 Temperature dependences of the threshold current and slope efficiency measured for 1-mm-long uncoated lasers in pulsed regime (200 ns/100 kHz) in temperature range from 77 to 325 K.

Figure 3.7 plots the temperature dependences of the threshold current and slope efficiency of the 1-mm-long uncoated lasers. The parameters T_0 and T_1 characterizing exponential temperature dependence of the threshold current and efficiency near RT are about 50 and 150K, respectively. These values are close to those recorded for single-stage lasers. This is expected since in both single and two-stage lasers the active QWs are pumped to nearly the same concentration level. What makes the difference is the value of the injection efficiency for two-stage cascade lasers. It is above 130% at RT and approaches nearly 200% at 100K, more than twofold improvement as compared to single-stage devices. This observation confirms efficient carrier recycling in two-stage cascade laser heterostructure.

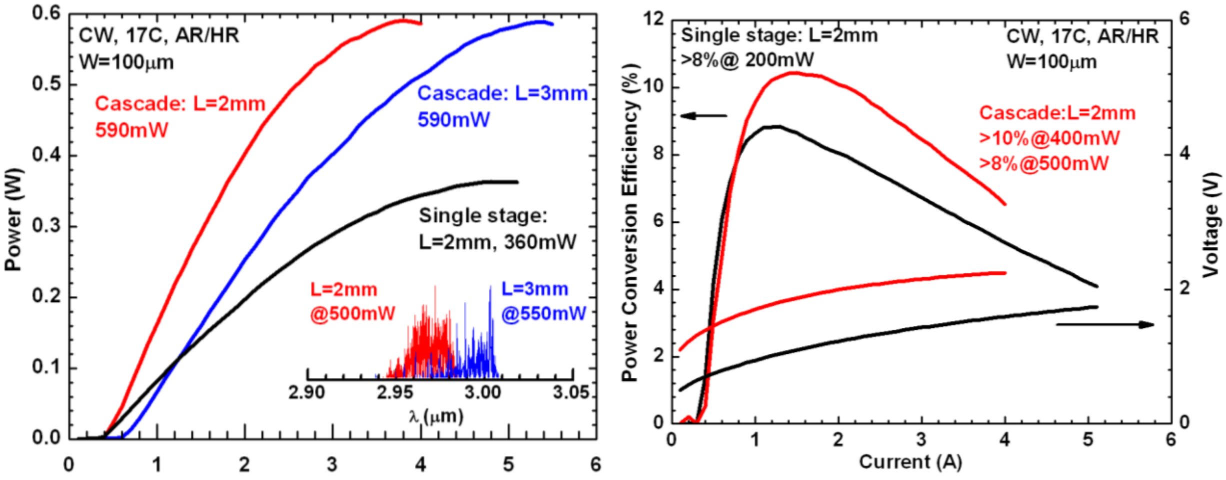

(a) (b)

Figure 3.8 Current dependences of (a) the output power and (b) power conversion efficiency measured in CW regime at heatsink temperature of 17 ^{o}C for 2- and 3-mm-long AR/HR coated epi-down mounted lasers with two-stage cascade design. Insets show the laser emission spectra.

Figure 3.8 shows CW power-current-efficiency characteristics of the two-stage cascade as well as reference single-stage diode lasers emitting near 3 μm. The maximum output power level of both 2- and 3-mm-long lasers is about 590 mW – significant improvement as compared to previous record of about 360 mW obtained for single-stage diode lasers [28]. Not only the two-stage cascade devices generate higher maximum CW power but also they operate more efficiently at high output power levels. The PCE peaked at ~ 11% (Figure 3.8 (b)). The maximum PCE value is reached at higher injection levels in two-stage cascade devices. This is consequence of the higher value of the turn-on voltage—the increase of the current corresponding to peak PCE with turn-on voltage can be confirmed by differentiation of the PCE expression. The outcome is that the single-stage lasers generate only 200 mW of CW power near

3 µm with PCE above 8 % while the two-stage cascade devices generate more than 450 mW of CW power with efficiency approaching 10% for 2-mm-long lasers.

3.3 Two-stage cascade diode lasers emitting in 2.4 - 3.3 µm

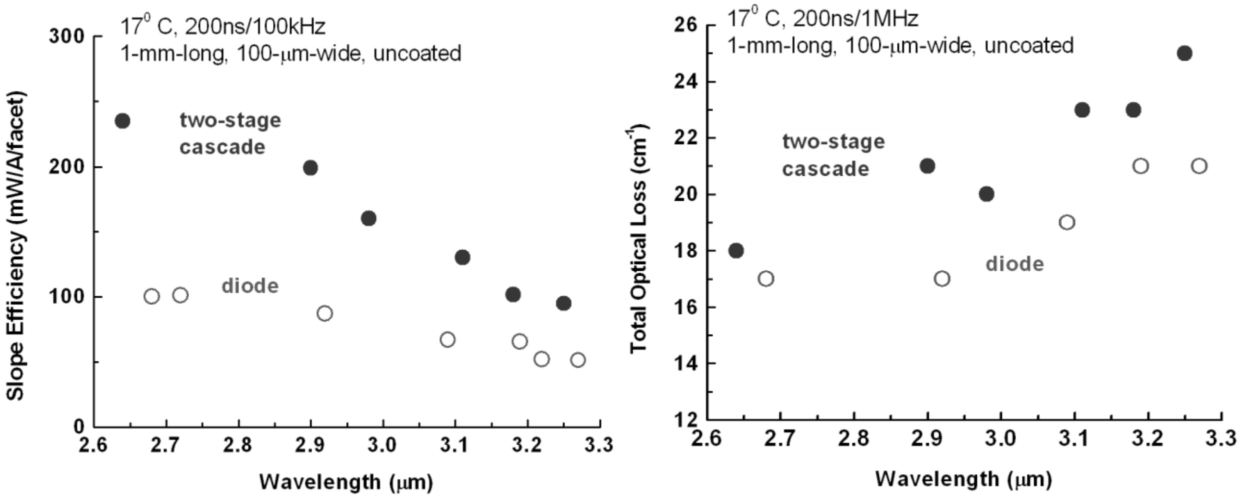

(a) (b)

Figure 3.9 Slope efficiency (a) and total optical loss (b) as measured by Hakki-Paoli technique of the 2.6 – 3.3 µm emitting 1-mm-long uncoated two-stage cascade (solid circles) and reference single stage diode lasers (open circles).

The tunnel junction/injector heterostructure that was used to connect in series two 3 µm emitting gain stages was utilized in devices emitting in wider spectral range. Figure 3.9 shows slope efficiency (a) and total optical loss (b) of several two-stage cascade lasers emitting in spectral region from 2.4 to 3.3 µm [60]. The corresponding parameters of the reference single stage diode lasers designed and developed by our research group are also shown. All lasers emitting at and below 3 µm had double-QW gain sections while devices emitting above 3 µm used triple-QW gain sections. Like in case of 3 µm emitting device the twofold increase of the slope efficiency is accompanied by moderate optical loss increase. All devices operated in fundamental mode of transverse waveguide heterostructure and were characterized by current independent single lobe fast axis far field pattern.

When considering design of cascade lasers emitting at shorter wavelength the possibility of the band-to-band absorption in InAs layers of tunnel junction/injector should be considered. Our calculations show that under operating voltage the cut-off wavelength for band-to-band absorption in the widest (~ 4-nm-wide) InAs QW of AlSb/InAs electron injector (Figure 3.3) is about 2.3 µm at RT. Thus for lasers operating at wavelength near and below 2.3 µm high absorption loss can be anticipated.

3.3.1 2.4 µm two-stage cascade diode lasers

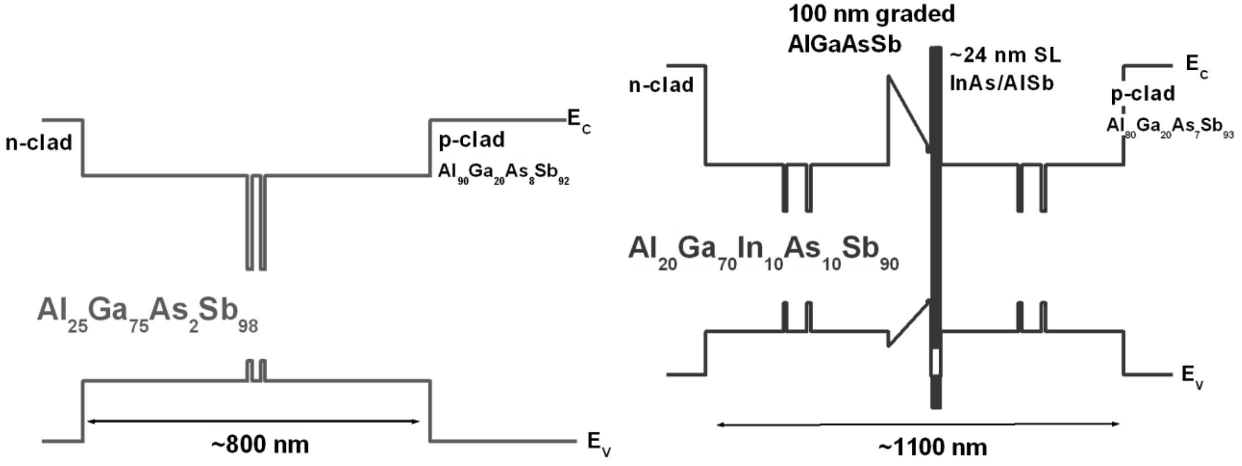

(a) (b)

Figure 3.10 Schematic flat band diagrams of the reference single-stage (a) and two-stage (b) cascade type-I QW GaSb-based diode laser heterostructures emitting near 2.4 µm at RT.

Two-stage cascade diode lasers emitting near 2.4 µm were designed and fabricated [61]. Figure 3.10 shows the calculated flat band diagrams of the reference single-stage (a) and two-stage (b) cascade diode lasers. For this experiment the QW composition and widths were the same for both reference and cascade structures, 10-nm-wide nominally $Ga_{65}In_{35}As_{10}Sb_{90}$ with compressive strain of 1.5%. The thickness of quinary alloy barriers on both side of active region was 200 nm, while the thickness of both n- and p-cladding was 1.5 µm. However, the barrier composition was changed from $Al_{25}Ga_{75}As_3Sb_{97}$ quaternary to $Al_{20}Ga_{70}In_{10}As_{10}Sb_{90}$ quinary alloy. The change was made in attempt to maintain efficient operation of the original design of tunnel junction/injector heterostructure. It can be speculated that graded composition AlGaAsSb and AlSb/InAs chirped SL layers might not effectively stop electrons in first stage and deliver them to next stage, respectively, when $Al_{25}Ga_{75}As_{3}Sb_{97}$ quaternary barriers are used. Clearly, both of these layers can be modified to accommodate this barrier layer but the purpose of this particular experiment was to study lower wavelength limit of the original tunnel junction/injector heterostructure.

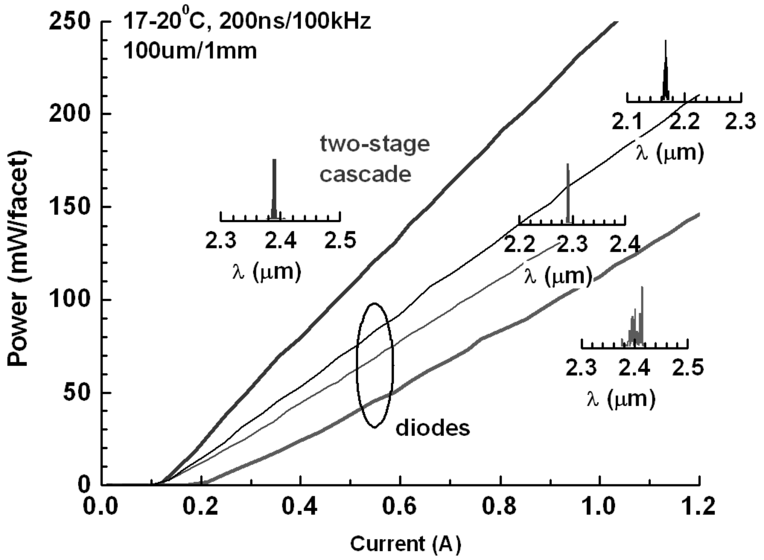

Figure 3.11 Light-current-voltage characteristics measured at 17 oC in short pulse regime (200 ns/100 kHz) for 2.4 μm emitting two-stage cascade lasers and reference single-stage lasers operating in spectral region from 2.15 – 2.4 μm.

Figure 3.11 compares light-current-voltage characteristics of the 2.4 μm two-stage cascade laser and 2.15 – 2.4 μm single-stage diode lasers. The two-stage cascade 2.4 μm devices still demonstrate twofold improvement of the device slope efficiency as compared to reference 2.4 μm laser. Moreover, the slope efficiency of the 2.4 μm device is higher than that of state-of-the art diode lasers operating at shorter wavelength. The far field was measured for 2.4 μm two stage cascade lasers (Figure 3.12), showing a single lobe on the fast axis (transverse direction) with a FWHM value of ~60^{o}, affirming that the fundamental optical mode is dominating in lasing, regardless the waveguide supporting higher modes and the doped tunnel junction locating at the maximum of fundamental mode.

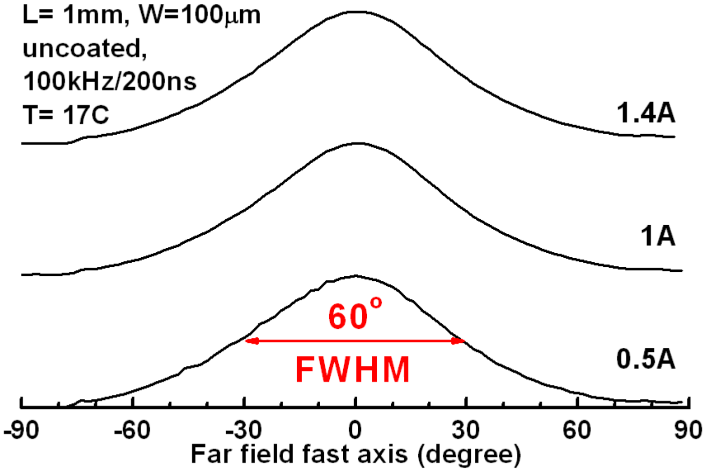

Figure 3.12 Fast axis far field patter measured at several currents above threshold for two-stage 2.4 μm cascade laser.

The modification of the tunnel junction and chirped SL electron injector can be performed to achieve cascade pumping of the lasers with wavelength below calculated cut-off of ~2.3 μm. The modifications might include optimization of the doping profile to blue-shift the absorption edge of InAs QW and use of GaInSb layers in place of GaSb on p-side of the tunnel junction. The valence band is raised on absolute energy scale in GaInSb as compared to GaSb and thus the quantization energy in the first InAs QW in chirped SL can be increased leading to blue shift of the band-to-band absorption edge.

The internal optical losses were estimated by Hakki-Paoli method as 6 cm^{-1} for 2.4 μm (Figure 3.13). Comparing to the single stage lasers, this value is about 1 cm-1 and 4 cm-1 higher. The absorption in the doped tunnel junction is the major cause for this increase of internal optical loss. But this increase is not severe and can be compensated by the high differential gain, which is about 30% higher than the single stage lasers. The high differential gain, as well as the nearly unchanged transparency currents, is the benefit from the design of two-stage gain sections in serial. Based on the value of internal optical loss, the internal efficiency was calculated. In RT, the cascade lasers manifested improved internal efficiency, about 150% for 2.4 µm two-stage cascade lasers. The internal efficiency above 1 verifies that carriers are recycled by the tunnel junction.

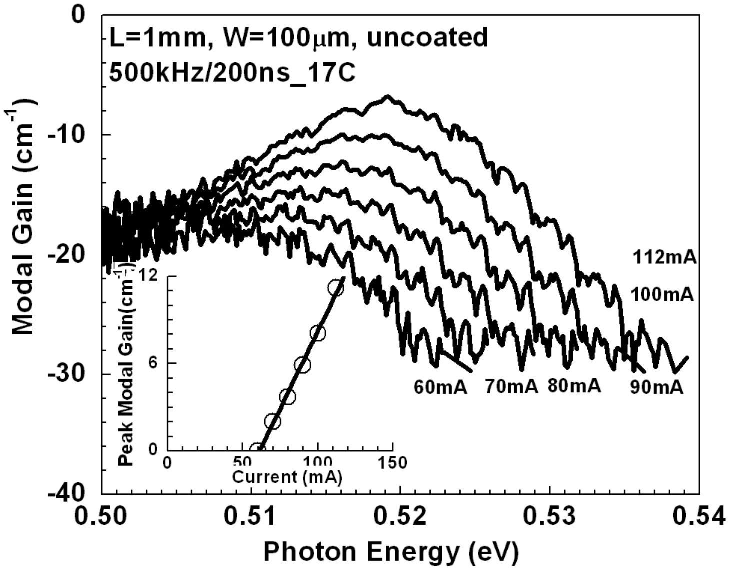

Figure 3.13 Modal gain spectra for 2.4 µm two-stage cascade laser at different current below threshold, inset shows current dependences of the peak modal gain.

Figure 3.14 (a) shows CW power-current-voltage characteristics of the two-stage cascade devices emitting near 2.4 µm. The corresponding characteristics of the reference state-of-the-art single-stage diode lasers [25] are shown on the same figure for comparison. The maximum CW power level was increased in cascade devices as compared to previous records obtained with single stage diode lasers. It should be noted that 2.4 µm devices are based on laser heterostructure shown in Figure 3.10 (a), i.e. they have not optimal barrier alloy composition. This led to parameter T_0 equal to of about 50 K at RT. However, twofold improvement of the device injection efficiency overcome somewhat compromised thermal stability and led to new record CW output power level of 1.2 W. The operating voltage was increased twofold for 2.4 µm emitting lasers, the somewhat excessive voltage drop increase is explained by the fact that tunnel junction/injector used in 2.4 μm emitters was optimized for the barrier material of 3 μm lasers (Figure 3.3) and not for barrier material used in 2.4 μm emitters (Figure 3.10 (b)). The two-stage cascade devices not only generate higher maximum CW power but also they work more efficiently at high output power levels, despite the fact that the cascade lasers requires higher driving voltage than single stage lasers. The PCE peaked at above 13% for 2.4 μm two-stage cascade lasers (Figure 3.14 (b)). At their peak PCE condition, 2.4 two-stage cascade devices produce 300 mW power, while the single stage devices of corresponding wavelengths only produce half amount of the power at the peak PCE. The 2.4 μm two-stage cascade lasers generate up to 1 W with PCE above 10%, while the single stage lasers only generate up to 600 mW.

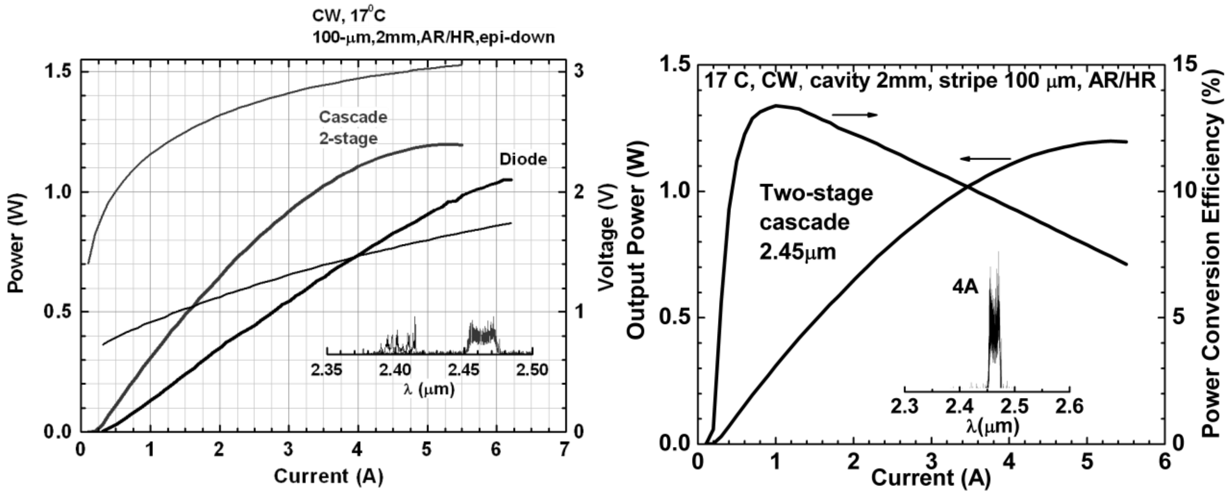

(a) (b)

Figure 3.14 (a) Power-current-voltage characteristics of the 2.4 μm emitting lasers measured in CW regime at heatsink temperature of 17 ^{o}C for 2-mm-long AR/HR coated epi-down mounted lasers (b) current dependences of power conversion efficiency of 2.4 μm two-stage cascade lasers. Inserts show the laser emission spectra.

3.3.2 2.7 µm two-stage cascade diode lasers

Two-stage cascade diode lasers emitting near 2.7 µm were designed and fabricated based on the laser heterostructure in Figure 3.10 (b) but used 10-nm-wide $Ga_{55}In_{45}As_{15}Sb_{85}$ QW [60].

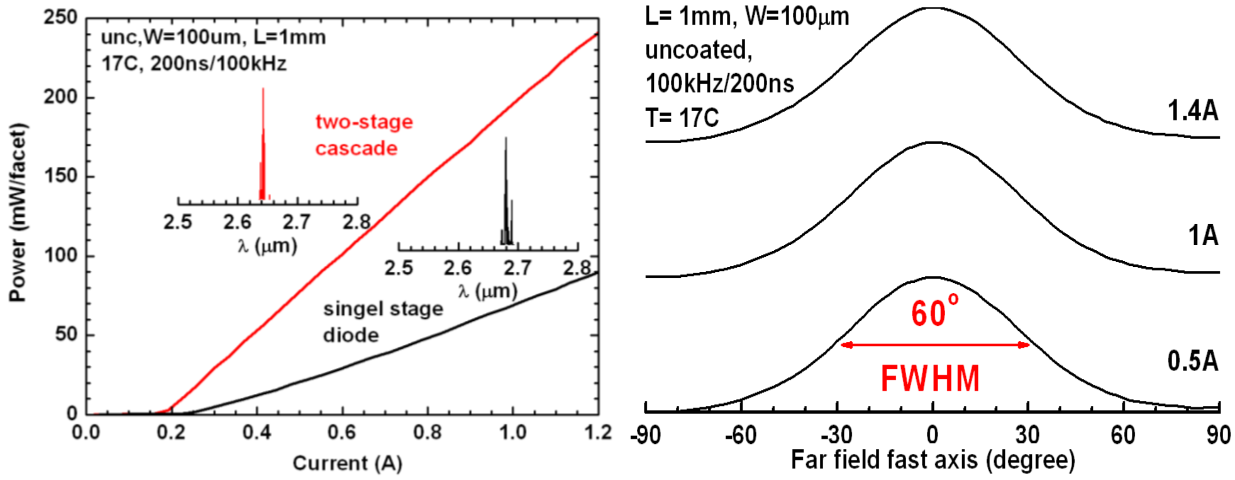

(a) (b)

Figure 3.15 (a) Light-current-voltage characteristics measured at 17 °C in short pulse regime (200 ns/100 kHz) for 2.7 m emitting two-stage cascade lasers and reference single-stage. Inserts show the laser emission spectra. (b) Fast axis far field patter measured at several currents above threshold.

Figure 3.15 (a) compares light-current-voltage characteristics of the 2.7 µm two-stage cascade laser and single-stage diode lasers. The two-stage cascade 2.7 µm devices still demonstrate twofold improvement of the device slope efficiency as compared to reference 2.7 µm laser [62].The far field was measured for 2.7 µm two stage cascade lasers (Figure 3.15 (b)), showing a single lobe on the fast axis (transverse direction) with a FWHM value of ~60°, affirming that the fundamental optical mode is dominating in lasing, regardless the waveguide supporting higher modes and the doped tunnel junction locating at the maximum of fundamental mode.

Figure 3.16 shows CW power-current characteristics and PCE of the two-stage cascade devices emitting near 2.7 µm. The corresponding characteristics of the reference state-of-the-art single-stage diode lasers are shown on the same figure for comparison. The maximum CW power level was increased in cascade devices as compared to previous records obtained with single stage diode lasers. Again, despite lack of optimization efforts the cascade pumping led to new record CW output power level of 750 mW. The operating voltage was increased less then twofold for 2.7 µm emitting devices, and the somewhat excessive voltage drop increase is explained by the fact that tunnel junction/injector used in 2.7 µm emitters was optimized for the barrier material of 3 µm lasers (Figure 3.3) and not for barrier material used in 2.7 µm emitters.

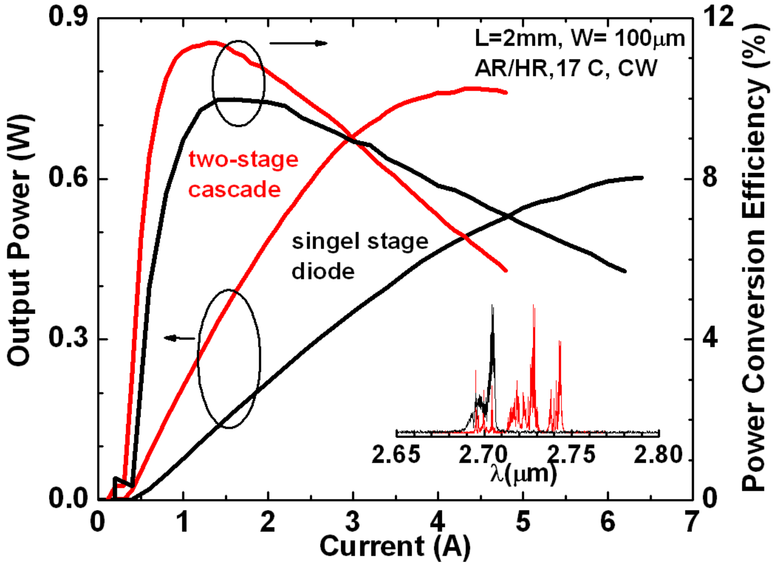

Figure 3.16 Current dependences of the output power and power conversion efficiency of 2.7 µm emitting lasers measured in CW regime at heatsink temperature of 17 °C for 2-mm-long AR/HR coated epi-down mounted devices. Insets show the laser emission spectra.

The PCE peaked at ~ 11% (Figure 3.16). The maximum PCE value is reached at higher injection levels in two-stage cascade devices. This is consequence of the higher value of the turn-on voltage—the increase of the current corresponding to peak PCE with turn-on voltage can be confirmed by differentiation of the PCE expression. The outcome is that the single-stage lasers generate only 450 mW of CW power near 2.7 µm with PCE above 8 % while the two-stage cascade devices generate more than 740 mW of CW power with efficiency approaching 8% for 2-mm-long lasers.

3.3.3 Two-stage cascade diode lasers emitting above 3 µm

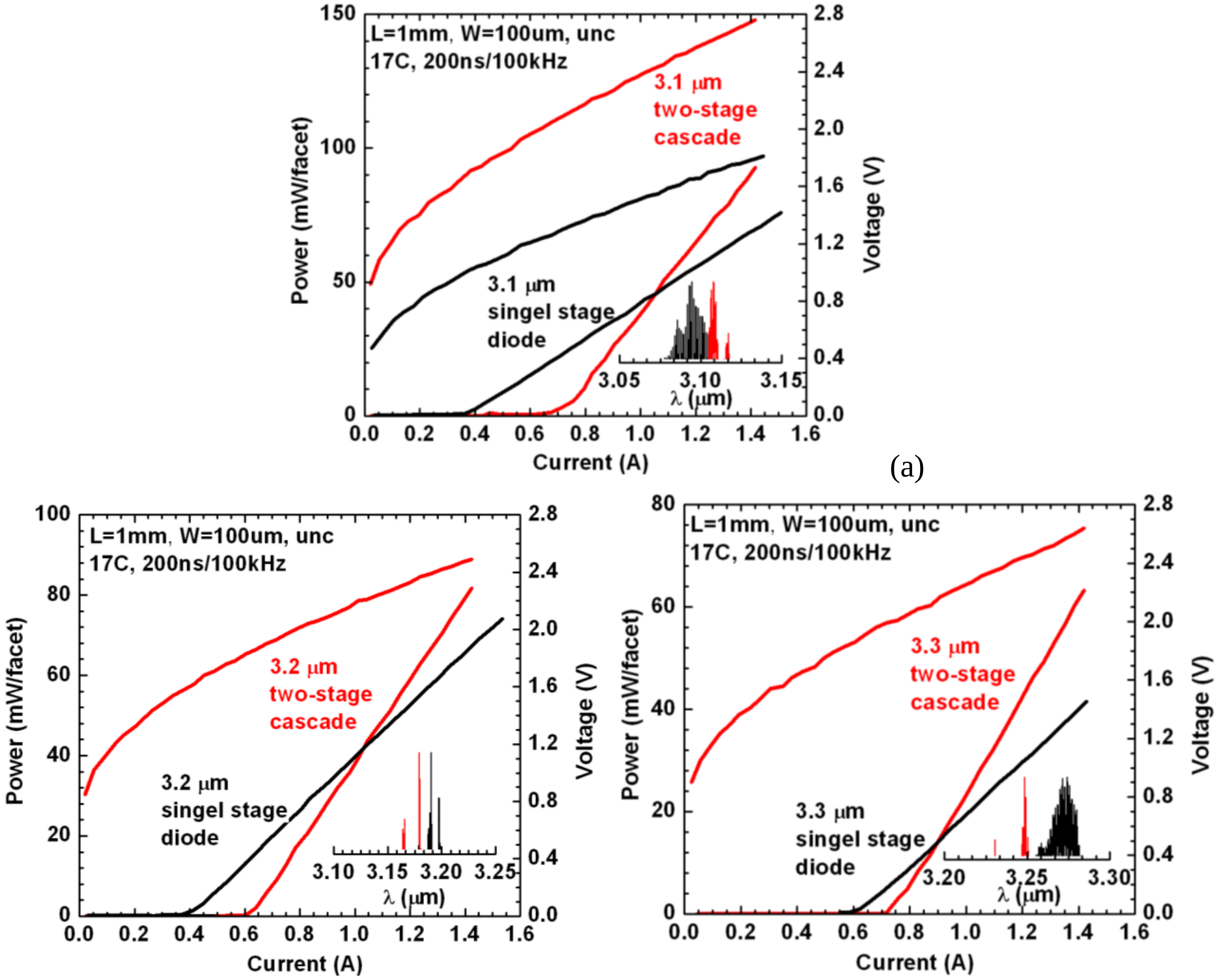

Figure 3.17 Light-current-voltage characteristics measured at 17 oC in short pulse regime (200 ns/100 kHz) for (a) 3.1, (b) 3.2, (c) 3.3 µm emitting two-stage cascade lasers and reference single-stage. Inserts show the laser emission spectra.

Two-stage cascade diode lasers emitting 3.1, 3.2, 3.3 µm were designed and fabricated based on the cascade laser heterostructure in Figure 3.3, but have three QWs in each gain sections [60]. The InGaAsSb QWs are 12-13 nm thick, with a nominal compressive strain near 1.5%m, with space of 50 nm in between. The In composition in QWs was adjusted respectively to match the operating waveguide of 3.1, 3.2, 3.3 µm. The Al composition in the quinary AlGaInAsSb alloy used as barriers/waveguide was increased to 22% from 20% in Figure 3.3, to maintain a sufficient valence band offset for the QWs operating in spectral range above 3 µm. The thickness of quinary alloy waveguide was reduced on inner side to shift the QWs closer to the center of whole active region, where is the maximum of optical field located, for the purpose of increasing QW optical confinement factor.

Figure 3.17 compares light-current-voltage characteristics of the 3.1, 3.2, 3.3 µm two-stage cascade laser and the reference single-stage diode lasers of same operating wavelengths, respectively. The two-stage cascade devices demonstrate twofold improvement of the device slope efficiency as compared to reference lasers in the spectra range of 3.1- 3.3 µm. The threshold currents of the two-stage cascade lasers were increased as compared to the reference single stage lasers [28]. Twofold improvement of the device slope efficiency was observed in the two-stage cascade lasers. The threshold current increase was partially associated with somewhat reduced QW compressive strain leading to compromised hole confinement and reduced differential gain [13]. The voltage drop across the two-stage cascade laser heterostructure was increased by less than 1 V. The increase of the device operating voltage by roughly the bandgap of the barrier material with each added gain section is expected. Therefore, the increased threshold current density, as well as the high driving voltage required for two-stage cascade structures, will introduce extra Joule heat in lasers CW operation, which will cause relatively rapid thermal roll-over of the laser power-current characteristics, despite that the 3.1 – 3.3 µm lasers would suffer worse thermal stability as compared to the lasers emitting below 3 µm. All these factors may limit the CW operation of the two-stage cascade lasers emitting above 3 µm.

With current cascade structure design, only 30 mW and 80 mW CW output power (Figure 3.18) at RT were achieved for the 3.1 and 3.3 µm two-stage cascade lasers, far below the best CW output power at RT from single stage diode lasers with the same wavelength. In order to boost the CW operation for cascade lasers emitting above 3 μm, the cascade structure needs to be optimized to improve the QW confinement factor and driving voltage; moreover, cascade structure with more active stages may be required. These will be discussed in the following sections.

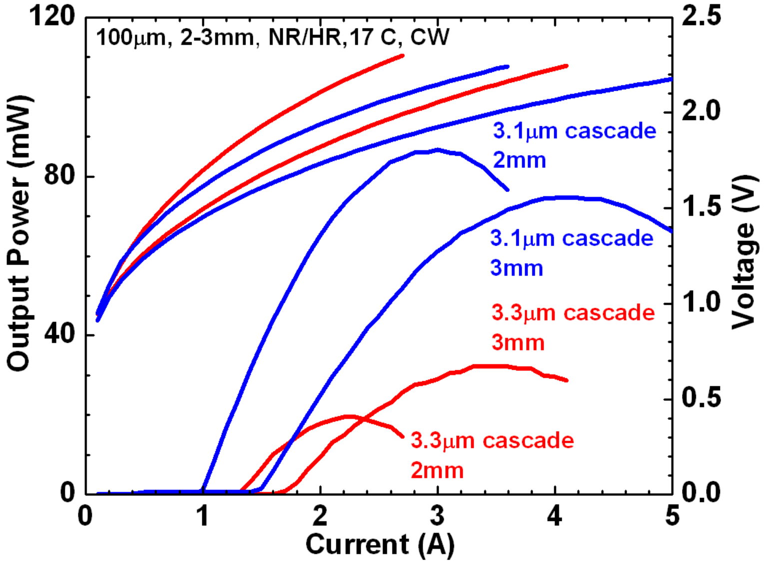

Figure 3.18 Current dependences of the output power measured in CW 17 ^{o}C for 2- and 3-mm-long NR/HR coated epi-down mounted 3.1 and 3.3 μm two-stage cascade lasers.

3.4 Two stage cascade lasers with optimized heterostructure

In previous sections, we have shown [46] that, at least within antimonide material system, the cascade pumping scheme is compatible with type-I QW interband gain sections providing efficient carrier recycling between stages leading to internal efficiencies in excess of 100% and improved high power operation of edge emitting diode lasers. Corresponding high power RT operated 2.4 – 3.3 μm two-stage cascade diode lasers were fabricated [60]. Experiment confirmed that interband tunnel junction followed by electron injector located near antinode of the laser mode did not lead to excessive internal optical loss. In devices reported previously [46] , the separation between active QWs and electron injector was above 200 nm (Figure 3.19(a)). Large spacing eliminated any interaction between gain section and injector but led to reduced

QW optical confinement factor. Consequently a potential of the cascade pumping scheme to minimize threshold current density was not realized.

In this section, we eliminated the separations between the active QWs and the electron injector (Figure 3.19). This design was implemented in order to reduce threshold current density and improve device efficiency. New generation of 3 μm cascade diode lasers demonstrated CW RT threshold current densities as low as 100 A/cm^2. Peak PCE in CW regime at RT was 16% for two-stage 2-mm-long 100-μm-wide ridge coated lasers [63].

3.4.1 Laser heterostructure and device fabrication

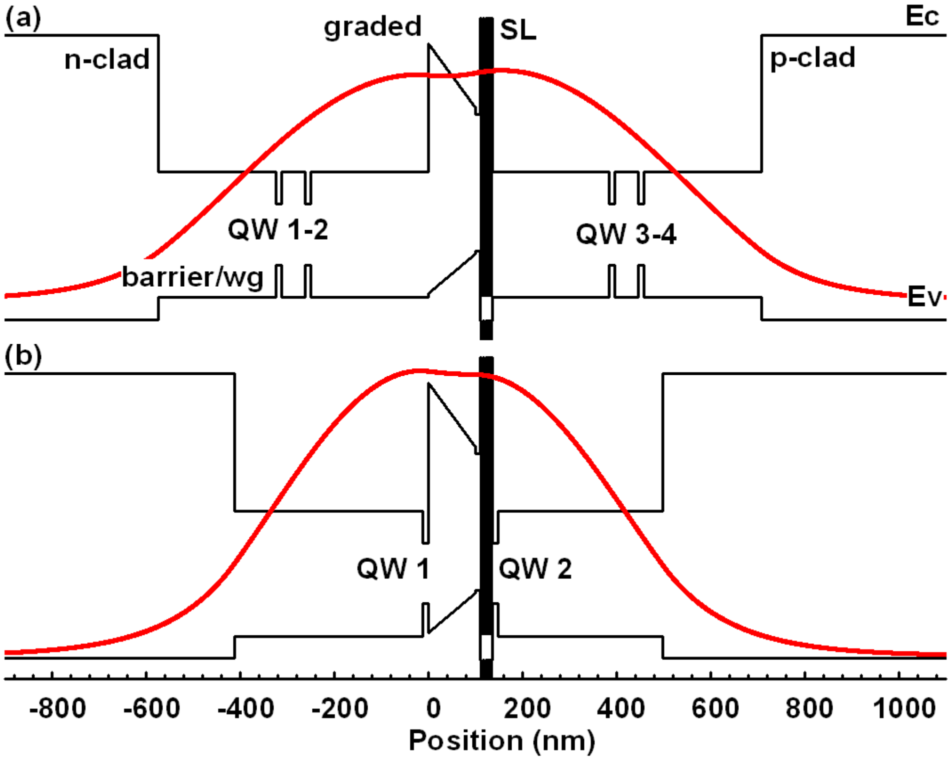

Figure 3.19 Schematic band diagram of the cascade laser heterostructures under flat band condition and the simulated optical near field: (a) original 3 μm two-stage cascade lasers [46] and used as a benchmark in this section; (b) optimized two- stage cascade lasers designed for improved optical confinement and minimized threshold current density.

Figure 3.19 shows band diagram schematics of the original and optimized cascade laser heterostructure, which was grown by solid-source MBE on GaSb substrates with the following common characteristics. The n- and p-cladding layers were made of $Al_{80}Ga_{20}As_{7}Sb_{93}$ doped with Te and Be, respectively. The barrier and waveguide core layers were nominally undoped $Al_{20}Ga_{55}In_{25}As_{23}Sb_{77}$ [16]. Compressively strained (~1.5%) 12 nm-wide GaInAsSb layers, with ~50% Indium, comprised the QWs responsible for the RT optical gain near 3 µm. Graded layer was nominally undoped AlGaAsSb with Al composition changing from 50% down to ~5% over thickness of 100 nm. The graded layer was followed by tunnel junction and electron injector comprised of nominally undoped 10-nm-thick GaSb, 2.5-nm-thick AlSb, and Te-doped 6-period InAs/AlSb chirped SL.The grown structures were processed into 100-µm-wide dielectric confined ridge lasers.

Original two-stage cascade structure (Figure 3.19 (a)) depicts the design of the original type-I QW GaSb-based diode laser [46], which is discussed in Section 3.1, and used in this section as a baseline reference sample. It was designed so that the fundamental optical mode overlapped the two double-QW narrow waveguide laser active regions separated by a tunnel junction and electron injector with 1.2-nm-thick AlSb layers. This two-stage cascade laser design exhibited a slope efficiency twice that reported for standard single stage type-I QWs GaSb based diode laser heterostructures [10]. Note, however, that neither the differential gain nor the threshold current density of the cascade lasers utilizing original cascade structure improved, because of a nearly twofold reduction of the optical confinement factor per QW.

Optimized two-stage cascade structure (Figure 3.19 (b)) was developed specifically to increase the optical confinement factor of active QWs and to minimize threshold current density. To accomplish this, the QWs were moved close to the anti-node of the fundamental waveguide optical mode and, thus, located adjacent to the graded and electron injector layers. Also, the number of QWs in each cascade was reduced to one. It was expected that modified cascade structure would reduce the threshold current density by a factor of 2 and thereby enhance the PCE.

The PCE can be written using a piecewise model of current-voltage characteristics as

$$PCE(I) = \frac{\eta \times (I - I_{TH})}{I \times (V_0 + I \times R_S)} \tag{2.1}$$

Where η is the device slope efficiency, I is the current, I_{TH} is the threshold current, V_0 is the voltage drop across active region, and R_S is series resistance. The peak PCE can be estimated by differentiating Equation. 2.1 (and ignoring the effects of Joule heating):

$$PCE_{MAX} = \frac{\eta}{I_{TH} \times R_S} \times \left(1 + \sqrt{1 + \frac{V_0}{I_{TH} \times R_S}}\right)^{-2} \tag{2.2}$$

Clearly, both reduction of the threshold current and increase of the slope efficiency are beneficial, but the latter has a more pronounced effect.

3.4.2 Results and discussion

Figure 3.20 shows RT plots of Hakki-Paoli modal gain spectra [40] acquired from 100-μm-wide 1-mm-long uncoated lasers based on original and modified two-stage cascade structures. They all had net cavity losses (horizontal solid lines in Figure 3.20) between 20 and 22 cm^{-1}, which corresponded to internal optical losses of 8–10 cm^{-1}.The bandwidth of the gain spectra (measured at the locations of the estimated cavity loss level indicated by the vertical arrows shown in Figure 3.20) was less than 40 meV near threshold for the devices based on original two-stage cascade structure. This gain bandwidth was comparable to that typically measured for standard GaSb-based type-I QW diode lasers emitting near and above 3 μm [10]. The latter observation is predictable since two-stage cascade lasers based on structure R utilize the same symmetric QWs as standard diode lasers do. In modified cascade structure, the QWs have asymmetric barriers and QW2 (Figure 3.19) is grown directly on top of the last AlSb layer of chirped InAs/AlSb SL electron injector. The nominal thickness of all AlSb layers in electron injector of both original and modified structures was 1.2 nm. Devices based on original and modified demonstrated nearly twofold increase in threshold gain bandwidth (middle plot in Figure 3.20).

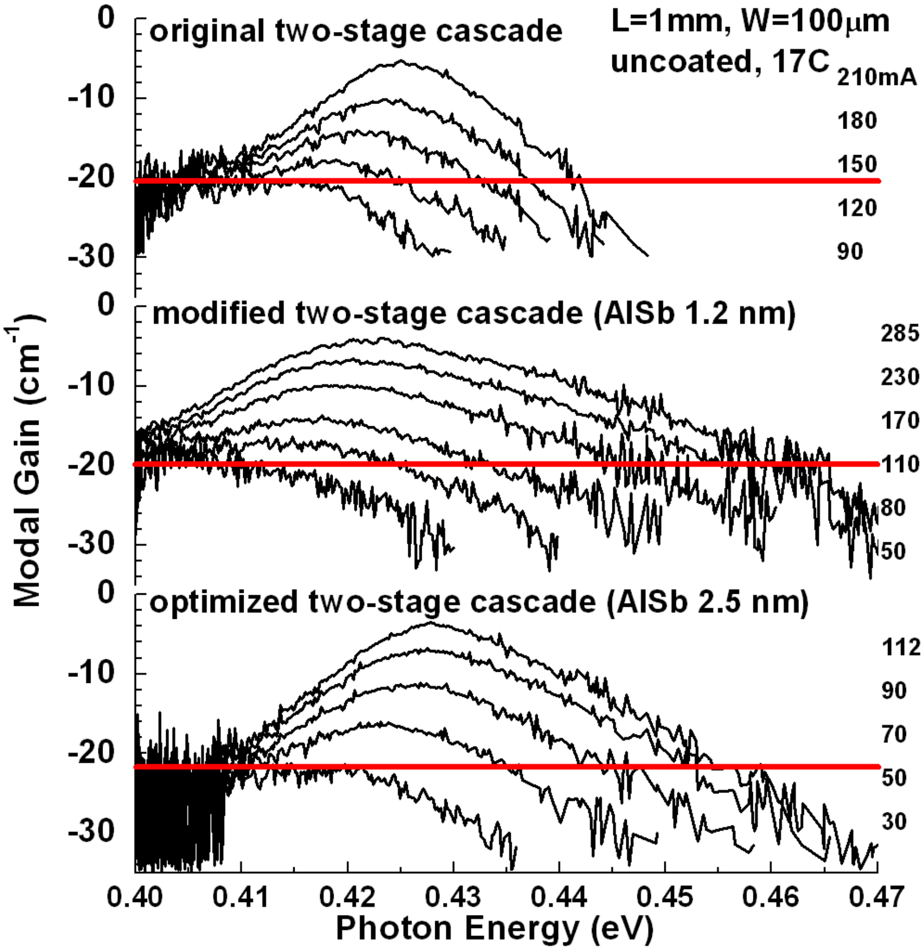

Figure 3.20 Modal gain spectra measured by Hakki-Paoli method for original, modified (AlSb 1.2 nm) and optimized (AlSb 2.5 nm) two-stage cascade lasers. The measurement was done at 17 oC for 1-mm-long, 100-μm-wide uncoated lasers in pulsed regime

Gain broadening was accompanied by severe suppression of differential gain with respect to current (close downward triangles in Figure 3.21) leading to threshold current degradation. In optimized structure, the thickness of only the last (directly preceding QW2) AlSb layer of electron injector was increased from 1.2 to 2.5 nm. This modification resulted in a diminished gain bandwidth (bottom plot in Figure 3.20) and significantly improved differential gain with respect to concentration (close upward triangles in Figure 3.21).

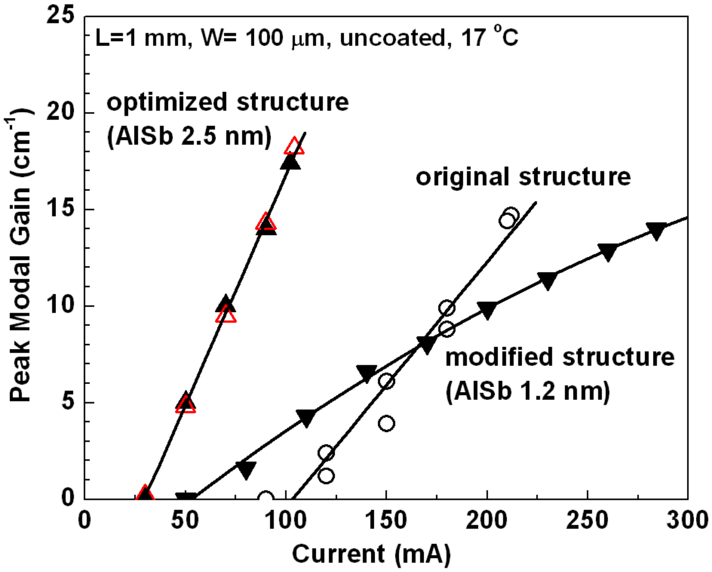

Figure 3.21 Current dependences of the peak modal gain of two-stage cascade lasers based on original structure (open circles), modified structure (solid down triangles), optimized structure (solid upward triangles), optimized structure with undoped last 4 periods of SL (open upward triangles).

It was notable that eliminating the Te doping from the last four layers of InAs/AlSb SL of the optimized cascade structure did not lead to further improvements of the modal gain (e.g., compare open to close triangle of Figure 3.21) or the gain bandwidth. This suggested that the gain broadening observed for lasers based on modified structure (Figure 3.20) could be attributed to enhanced effect of surface roughness scattering [64] in QW2 associated with a the narrow AlSb barrier. This contention was further corroborated by previously performed independent experiments that demonstrated that replacing the right barrier of QW1 with graded layer while keeping QW2 barriers symmetric like in original structure had only minor effects on gain bandwidth.

One can speculate that penetration of the electron envelope function associated with QW2 into InAs/AlSb SL leads to a decreased intrasubband dephasing time. Presumably surface roughness scattering that occurs at the InAs/AlSb heterointerface nearest to QW2 contributes the most to gain broadening. In addition, the increased net wave function overlap with heterointerfaces can lead to increased Auger16 and other nonradiative recombination rates. Therefore, we posit that both gain broadening and reduced carrier lifetime contribute to the decrease of the differential gain with respect to current observed in lasers based on modified cascade structure.

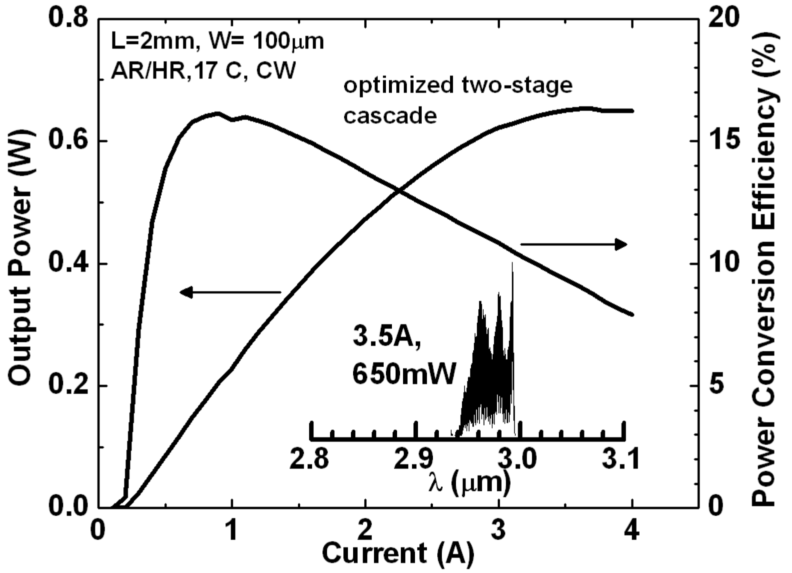

Figure 3.22 CW light-current-power conversion characteristics measured at 17 °C for 100-μm-wide, 2-mm-long AR/HR coated two-stage cascade lasers. Inset shows laser spectra at maximum power level.

Figure 3.22 shows plots of CW power and power conversion versus current acquired at 17 °C from 100-μm-wide, 2-mm-long AR/HR coated two-stage lasers based on optimized two-stage cascade structure. The threshold current density was ~100 A/cm^2; the maximum power was ~650 mW. The PCE reached ~16% and remained well above 10% for output powers above ~600 mW. All of these characteristics surpassed those of the previous state-of-the-art 3 μm lasers (i.e., original reference structure) [46]. Of particular note was the early twofold reduction of the threshold current density and corresponding improvement of the PCE predicted by Equation 2.2.

3.5 Three-stage cascade lasers

3.5.1 3 µm three-stage cascade lasers

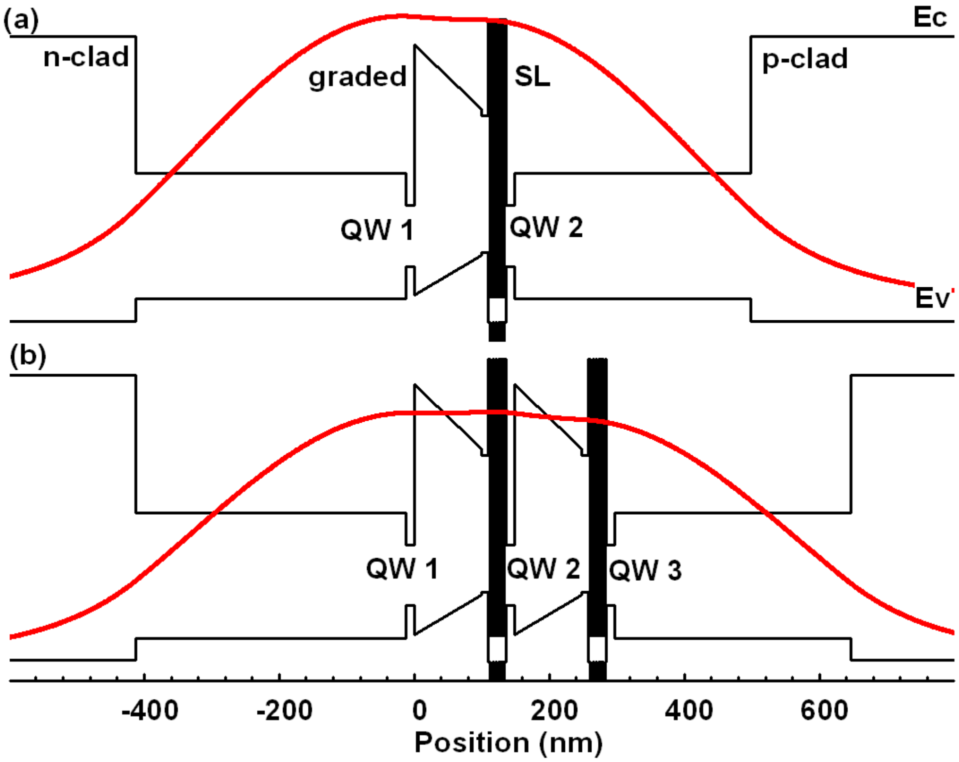

Figure 3.23 Schematic band diagram of the cascade laser heterostructures under flat band condition and the simulated optical near field: (a) optimized two-stage cascade lasers; (b) three-stage cascade lasers designed based on (a).

The three-stage cascade diode laser emitting 3 µm was designed based on the optimized two-stage cascade structure (Figure 3.19 (b)) by adding an extra single-QW gain stage [63]. It was expected that the efficiency, threshold current, and voltage drop across active region would scale with number of gain stages. However, our results indicated that the extent of this scaling depended heavily on the interaction between the QWs and adjacent electron injectors. Figure 3.23 shows band diagram schematics of optimized two-stage and three-stage cascade laser heterostructure. The three-stage cascade structure was grown by solid-source MBE on GaSb substrates with the same characteristics as two-stage cascade lasers. The grown wafer was processed into 100-µm-wide dielectric confined ridge lasers.

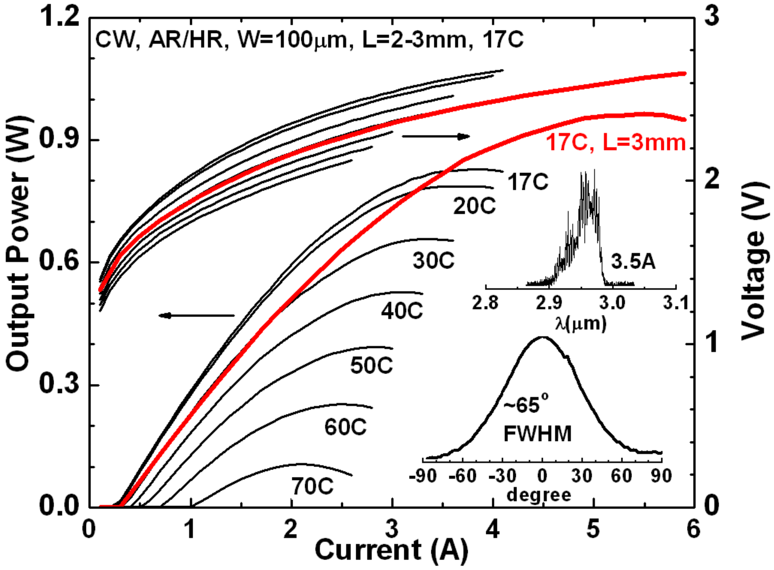

Figure 3.24 CW L-I-V characteristics of 100-μm-wide, 2- and 3-mm-long AR/HR coated three-stage cascade lasers. Insets show spectra of the 2-mm-long laser at 17 °C at maximum output power level and fast axis far field pattern.

Figure 3.24 shows CW light-current-voltage data acquired from AR/HR coated lasers fabricated from material grown according to Figure 3.23 (b) (i.e., three-stage cascade lasers). Data were acquired from a 100-μm-wide, 2-mm-long laser at temperatures between 17 and 70 °C. The design improvements incorporated into three-stage cascade structure increased this device's CW output power to 830mW 17 °C. The three-stage cascade lasers had T_0 and T_1 values above 50K and above 110 K, respectively, and a 70 °C maximum output power greater than 100 mW. The output power of 100-μm-wide, 3-mm-long three-stage laser was increased to ~960 mW at 17 °C; thanks to improved thermal footprint. The fast-axis far field beam divergence of three stage lasers was smaller than that of the two-stage device with narrower waveguide core (compare 65° in Figure 3.24 versus 69° of the optimized two-stage cascade lasers). Optical gain measurements indicated that the two- and three-stage devices had nearly the same internal optical loss. The internal efficiency of the 100-μm-wide three-stage cascade laser was ~190% at RT which confirmed the effect of three fold carrier recycling, specifically when compared to the single stage (regular diode devices) having 50 – 60% internal efficiencies [10]. However, the threshold current density for the threes-stage lasers was not lower than that of the two-stage devices (compare Figure 3.24 and Figure 3.22). We hypothesize that this results from the barrier energy asymmetries pushing the electron envelope wave functions in QW2 of the three-stage structure toward the SL side and thereby intensifying adverse interface interactions. At this moment, there are insufficient experimental evidences to isolate this fundamental phenomenon from the effects of growth-to-growth variation on carrier localization and lifetimes.

3.5.2 3.3 µm three-stage cascade lasers

The three-stage cascade diode laser emitting 3.3 µm was designed based on the cascade structure (Figure 3.23 (b)) but used different QWs. The composition of 13 nm thick, 1.5 % compressively strained QW was adjusted to $Ga_{42}In_{58}As_{30}Sb_{70}$ to extend the wavelength to 3.3µm, additional 5 nm thick $Al_{22}Ga_{46}In_{32}As_{30}Sb_{70}$ barriers were added between the QW and the graded/SL tunnel junctions, to maintain sufficient valence band offset. The grown wafer was processed into 100-µm-wide dielectric confined ridge lasers.

Figure 3.25 shows CW L-I-V characteristics of the three-stage cascade devices emitting near 3.3 µm. The corresponding characteristics of the reference state-of-the-art single-stage diode lasers are shown on the same figure for comparison [28]. The maximum CW power level was increased in cascade devices as compared to previous records obtained with single stage diode lasers. The 2- and 3-mm-long three-stage devices demonstrated maximum CW output power of 110 and 120 mW in RT, while the previous best output power obtained from single stage diode lasers of the same operating wavelength was about 50 mW. As compared with the previous two-stage cascade lasers of 3.3 um (section 3.3.3), which cannot produce better CW output power than the single stage lasers, the three-stage structure based on optimized cascade design improve the CW RT output performance at 3.3 um significantly.

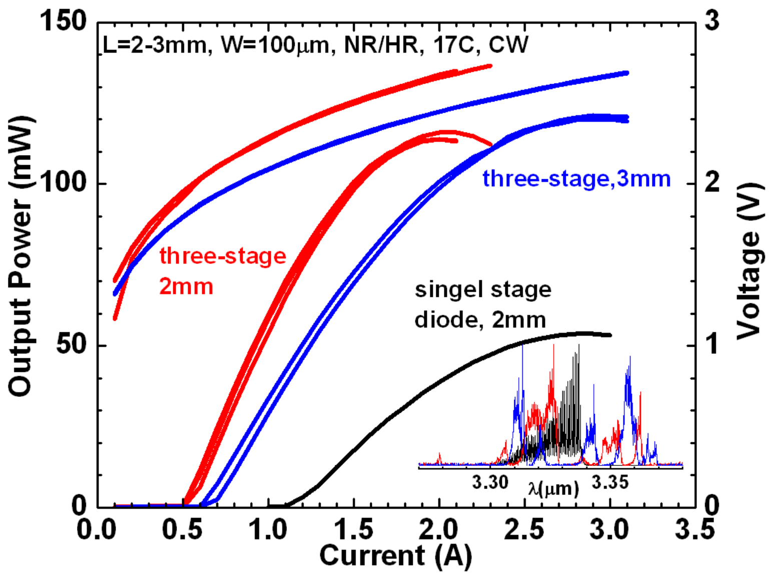

Figure 3.25 L-I-V characteristics of the 3.3 μm emitting three stage cascade lasers measured in CW regime at heatsink temperature of 17 ^{o}C for 2- and 3-mm-long NR/HR coated epi-down mounted lasers, as compared to the single stage diode lasers of the same wavelength. Inserts show the laser emission spectra.

3.6 Conclusion

In this chapter, we discussed the design and fabrication GaSb-based type-I QWs cascade diode lasers in the spectral range of 2.4 to 3.3 μm, with improved efficiency and CW operation performance in RT. The cascade pumping of the type-I QW gain sections was achieved utilizing efficient interband tunneling through "leaky" window in band alignment at GaSb/InAs heterointerface. Staggered band alignment between InAs-rich and GaSb-rich materials is critical component for development of the efficient bipolar cascade pumped lasers. The interband tunneling at type-III interface requires neither high doping nor large reverse bias leading to efficient device operation, and does not generate excessive absorption losses despite being located near the transfer mode peak.

Two-stage 2.4 – 3.3 μm cascade type-I QW diode lasers demonstrated twofold increase of the device efficiency and only moderate enhancement of the internal optical loss as compared to reference single-stage diode lasers. The internal efficiency of the two-stage cascade lasers were above 100% at RT and nearly 200% at 100 K. Cascade pumping led to record CW output power levels at RT in spectral region from 2.4 – 3 μm, namely 1200 mW, 750 mW and 590 mW at 2.4μm, 2.7 μm and 3 μm, respectively.

The two-stage cascade structure was optimized by utilizing single QW gain stages and removing waveguide materials between QWs and tunnel junctions, to improve the threshold current density and the QWs optical confinement factors. The 3 μm densely stacked two-stage cascade lasers demonstrated high differential gain, CW threshold current densities near 100 A/cm^2, a twofold improvement over the previous world record, that resulted in peak power conversion efficiencies increasing to 16% at 17 ^{o}C. Based on the optimized cascade structures, three-stage multimode cascade lasers emitting 3 – 3.3 μm were designed and fabricated, and demonstrated a maximum CW output power of near Watt level (960mW) for 3 μm, and 120 mW for 3.3 μm at RT, respectively.

The CW output power in RT from cascade devices were the new record maximum power for the GaSb-based type-I QWs diode lasers emitting in the spectral range of 2.4 – 3.3 μm, improved tremendously as compared to the single stage devices. This cascade approach is promising for increasing the output power of type-I QWs GaSb-based diode lasers operating in wide spectral range. The efficiency and output power may be further improved by optimization of the number of cascades and injector structure.

Chapter 4 Diffraction-Limited and DFB Diode Lasers Emitting near 3 µm and above

4.1 Introduction

4.1.1 Diffraction-limited lasers

For a certain given wavelength, if the potential of a beam to be focused to the smallest spot is as high as possible, this beam is a diffraction-limited beam, or for a given waist radius, the diffraction-limited beam has a minimum possible beam divergence. In detail, the beam waist with a certain beam radius of a beam being focused by an optical objective is related with the minimum beam divergence in possible. The most frequent beam shape of diffraction-limited beam is the Gaussian beam, where the transverse light intensity profile can be described by the Gaussian equation. The beam radius is the measurement of the transverse extension of a light beam, it can be defined as the distance from the beam axis where the intensity is $1/e^2$ of the value on the beam axis where is the maximum. The beam waist is where the beam has the minimum beam radius. The beam divergence represents how fast a beam expands as get far away from the focus spot in the far-field. Beam quality is a parameter representing how tightly a beam can be focused under certain conditions. The beam quality can be quantified as the beam parameter product (BPP), which is the product of the beam radius at the beam waist with the far-field beam divergence angle. Another way is the M^2 factor, which is defined as the beam parameter product divided by the one from a diffraction-limited Gaussian beam of the same wavelength. For the diffraction-limited Gaussian beam, the best possible beam quality can be achieved, when the $M^2 =1$.

The diffraction-limited lasers are the lasers output diffraction-limited beam. The diffraction-limited lasers usually operate on a single spatial mode, which means have single resonator mode in both transverse and lateral mode. The single mode is usually the fundamental resonator mode, of which the beam shape is usually close to Gaussian beam. Some intracavity beam distortions, for example in the gain medium, and the design of the resonator cavity, like the lateral width of the resonator and index difference, could cause the non-ideal beam quality, and even embarrass the laser to reach the diffraction-limited output.

Because of the fact that the single spatial mode on both transverse and lateral mode, the diffraction-limited lasers have the significant advantages in different applications, for instant, the fiber-coupled lasers prefer to have single spatial mode. More usually, the single spatial mode of the narrow ridge lasers is prerequisite for tunable diode laser spectroscopy sources based on either distributed feedback (DFB) [65] or external cavity concept [66]. The high power single spectral mode laser operating at RT in CW regime is required for the highly sensitive and compact tunable laser spectroscopy system, which is in great demand for the remote sensing, gas detection, medical diagnosis, industrial safety, process monitoring and environmental studies [67]. Fabrication of the single spatial mode laser with narrow ridge is a critical step to achieve single spectral mode operation and sensitive tunable laser spectroscopy.

For our regular GaSb-based type-I QWs laser edge emitting devices, the beam shape on transverse direction (the growth direction) basically follows the single mode, with a typical FWHM divergence angle of 65^o to 40^o, due to the relatively small transverse width of the resonator, which is the thickness of the waveguide core, about 0.5 to 1 μm. This direction is also called the fast axis of far field. Meanwhile the beam shape on the lateral direction (perpendicular to the growth direction) is not a single mode, due to the relatively large lateral width of the resonator, which is about 100 μm for the wide ridge lasers.

To achieve the diffraction-limited beam or single spatial mode from our GaSb-based type-I QWs lasers, the key is to realize the single mode on the lateral direction. This means the lateral width of the resonator which is defined by the ridge width must be controlled to go down to the wavelength level, about less than 10 μm, to eliminate the other mode rather than the fundamental mode. This requires high accurate lithography and etching. Otherwise, the etching depth is also need to be accurately controlled, because the depth will affect the index difference between the ridge and neighboring areas, and then affect the beam mode.

In our research group, a novel two-step selective wet etching technique was developed [68] and utilized to fabricate narrow ridge diffraction-limited GaSb-based diode lasers emitting from 2.0 [69] to 3.0 μm [70], demonstrating decent performance and output power. Although the wet etching technique is convenient and low-cost, the etching profile and depth by this method is not perfectly controllable. The devices may suffer from extra optical loss, current spreading and distorted beam shape, which are caused by the etching roughness, imperfect narrow ridge and non-vertical sidewalls.

Good control over ridge geometry is achieved by dry etching, like inductively coupled plasma reactive ion etching (ICP-RIE), although it requires costly equipment. Narrow ridge waveguide GaSb-based type-I QW diode lasers emitting near 3 μm fabricated by RIE have been reported [71-73]. However, the device's RT CW output power was limited to several mW level.

In this chapter, we will discuss various etching techniques, including wet etching, Cl_2-free and Cl_2-based ICP-RIE, which we developed to improve the etching profile and lasers performance. Diffraction-limited and distributed feedback diode lasers with narrow ridge waveguide were designed and fabricated by these etching techniques, using single stage or two-stage cascade diode laser structures. Diffraction-limited two-stage cascade lasers demonstrated

CW output power of 100 mW at 3 μm, and 40 mW at 3.15 μm in RT, respectively. 3.27 μm DFB diode lasers demonstrated CW output power of 15 mW at RT.

4.1.2 Review of 2 – 3 um diffraction-limited lasers fabricated by wet etching

In this section, the narrow ridge diffraction-limited GaSb-based diode lasers emitting from 2.0 to 3.0 μm fabricated by novel two-step selective wet etching technique will be reviewed.

Firstly, diffraction-limited 2 – 2.2 μm ridge waveguide lasers with CW output power near 100 mW at RT were fabricated with a two-step wet etching technique using the interface between the top cladding and waveguide core materials as an etch stopper [69]. The devices did not suffer from lateral current spreading. The second optical mode was suppressed by the low lateral confinement. Experiments showed that reducing the ridge width below 6 μm did not affect the device efficiency or the output beam quality but led to an increase of the transparency current density.

Table 4.1. Recipe of two-step wet etching etchants.

etchant (i)	sodium hydrogen tartrate: H_2O: H_3PO_4: H_2O_2	5 g : 90 ml : 30 ml : 30 ml
etchant (ii)	HCl: H_2O_2: H_2O	50 ml : 1 ml : 50 ml

The two types of etchants used to fabricate the narrow ridge devices are shown in Table 4.1. Figure 4.1 shows scanning electron microscope (SEM) images of the fully processed laser mirrors. The contrast between the claddings and the waveguide core materials allows observing that the etching was stopped at the interface between the p-cladding and the waveguide core. The lower Al composition waveguide core material served as an etch stopper for the HCl-based etchant. The SEM images show that the demonstrated wet etching methodology is capable of yielding ridge widths below 4 μm and relatively vertical sidewalls. The dashed arrows in Figure

4.1 (a) and (b) indicate the interface between the grading layer and the p-cladding layer. The projection with the length of about 150 nm in Figure 4.1 (a) is originated due to the longer etching time with the HCl based etchant to form the narrower ridge width compared to the device shown in Figure 4.1 (b). This can be avoided by balancing the p-contact metal width and the etching time with the tartrate based solution.

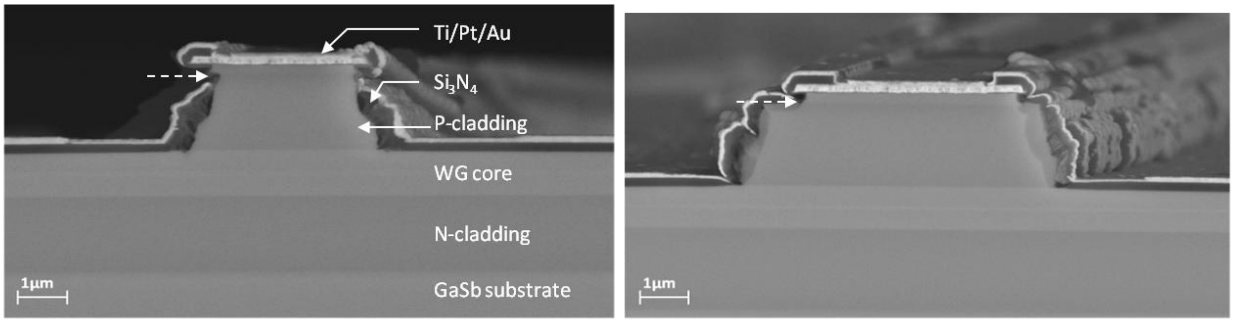

(a) (b)

Figure 4.1 SEM images of the completed narrow ridge lasers: (a) 2 μm laser with W = 3.5 μm, (b) 2.2 μm laser with W = 6 μm.

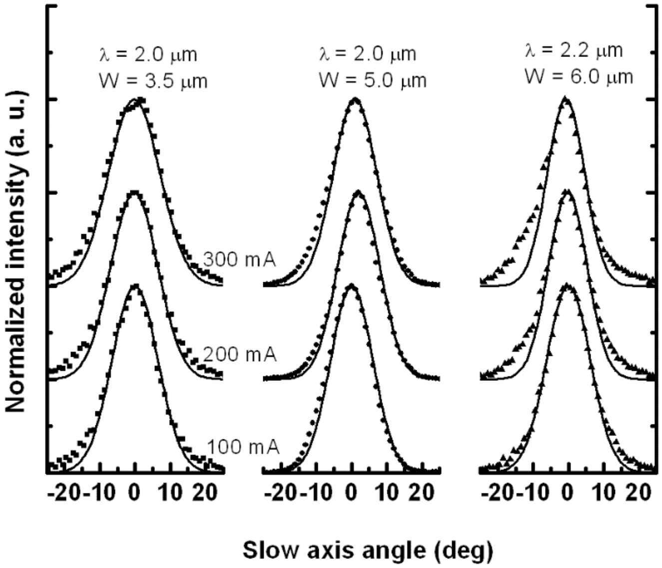

Figure 4.2 The far field divergence (symbols) along the slow axis for all narrow ridge lasers as a function of pulsed bias current (100 kHz/200 ns) from 100 mA to 300 mA at 20˚C. The solid lines are the Gaussian fittings.

Figure 4.2 plots the current dependence of far field patterns measured for the 3.5-μm-wide and 5-μm-wide 2 μm lasers and for the 6-μm-wide 2.2 μm lasers. Stable far field patterns with about 14˚ FWHM were observed for all devices. The measured far field patterns are in accordance with those calculated from the beam waist measurements described above.

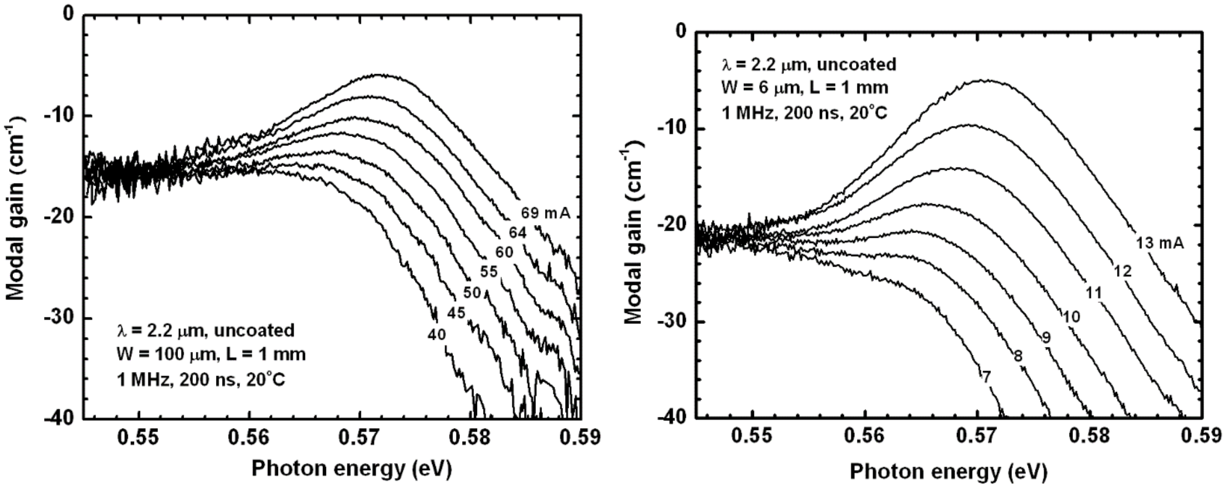

(a) (b)

Figure 4.3 Modal gain spectra of 2.2 μm 1-mm-long uncoated lasers measured by Hakki-Paoli method [40] in pulsed regime (1 MHz/200 ns) at 20˚C: (a) 100-μm-wide, (b) 6-μm-wide.

Figure 4.3 reveals the differences in the shapes of the modal gain spectra of the wide and narrow ridge 2.2 μm devices. As compared to the 100-μm-wide ridge lasers, the modal gain spectra of narrow ridge lasers indicate there is an extra optical loss of about 5 cm^{-5}. In the narrow ridge lasers, the modal size can be larger than the pumped area, for ridges etched down to the p-cladding/waveguide core interface, the current spreading arguably occurs only due to ambipolar carrier diffusion in the waveguide core and active QWs. This is in contrast to shallow ridge waveguide designs where the p-cladding material remaining outside of ridge can lead to a wider current spreading profile. The QW material outside the current path acts as an absorber optically pumped by the mode itself. Hence population inversion only under the ridge is insufficient. This scenario can explain distortion that can be noticed in the modal gain spectra of the 6-μm-ridge lasers.

The CW L-I-V characteristics of the 2-mm-long coated (AR=5%, HR=95%) lasers measured at 20˚C are shown in Figure 4.4. The inset shows the spectra of the lasers measured at 100 mA. The 2 and 2.2 µm lasers generate output power above 100 mW and 90 mW, respectively. Devices operate at voltage about 2 V at the highest bias current. The differential quantum efficiencies are about 45% for the 6-µm-wide lasers compared to 64% for the 100-µm-wide lasers. Somewhat unstable output power was observed within a certain range of applied CW current but this effect disappeared in pulse mode indicating it is a thermal effect.

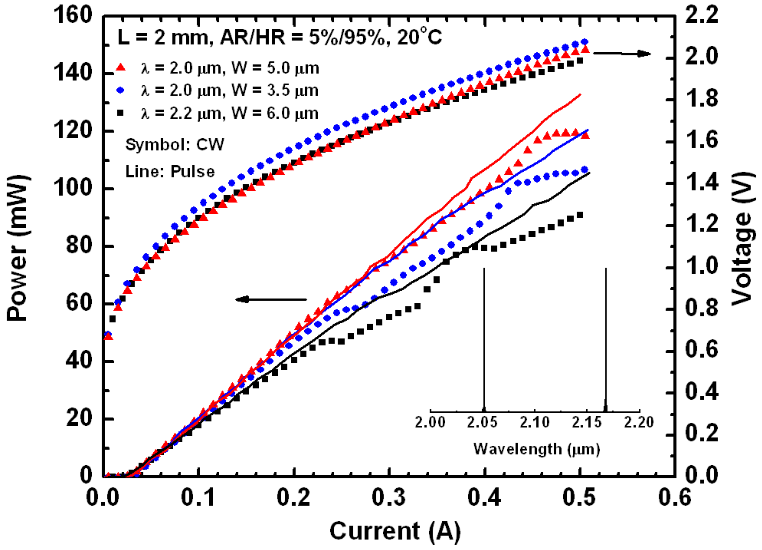

Figure 4.4 L-I-V of the 2-mm-long coated (AR/HR = 5%/95%) narrow ridge lasers under pulse mode (solid line, 100 kHz/200 ns) and CW mode (symbol) at 20˚C. The inset is the wavelength of each laser measured at 100 mA.

Secondly, 3 µm single spatial mode GaSb-based type-I QW diode lasers with 5.5mm-wide ridge waveguides were fabricated by selective wet etching technique [70]. The devices demonstrated CW output power above 15 mW at RT.

The narrow ridge devices were fabricated by two-step selective wet etching using the two types of etchants (Table 4.1). This procedure resulted in formation of the 5.5-µm wide 1.8-µm tall ridges with rather steep walls (Figure 4.5). The etching stopped at the p-cladding/waveguide core interface due to high selectivity of the etchant (ii) to Al content. Hence, AlGaInAsSb quinary waveguide core layer with 20% Al was utilized as an etch stop layer.

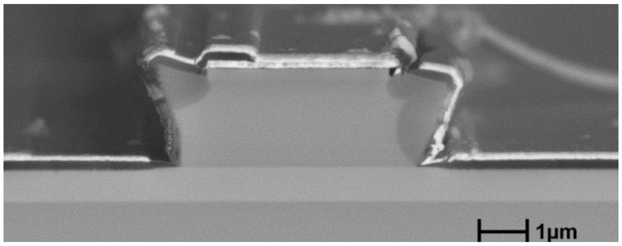

Figure 4.5 SEM image of 3 μm narrow ridges devices fabricated by selective wet etching.

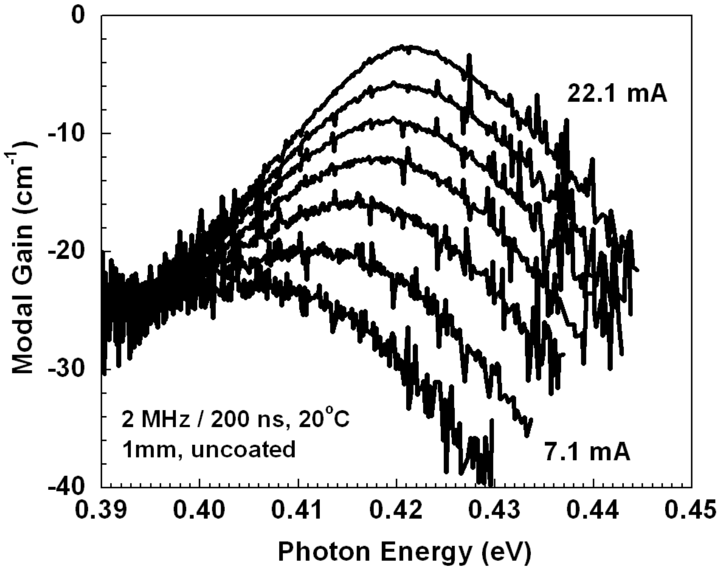

Figure 4.6 Modal gain spectra of 3 μm 1-mm-long uncoated lasers measured in pulsed regime (2 MHz/200 ns) at 20°C.

Figure 4.6 shows Gain spectra of narrow ridge device measured by Hakki-Paoli technique [40] for 1-mm-long uncoated lasers on the current density. Total optical loss values of 16 cm^{-1} were estimated for 100-μm-wide ridge waveguide multimode lasers. Narrow ridge single spatial mode devices demonstrated total optical loss of about 24 cm^{-1}. Thus the narrow ridge waveguide fabrication resulted in the additional internal optical loss of about 8 cm^{-1}. Presumably, the source of extra loss is the interaction of the optical field with metal in the deep ridge waveguide lasers and light scattering at ridge sidewalls. The internal quantum efficiencies for all devices were calculated to be about 55%.

Figure 4.7 shows the CW light-current-voltage characteristics of AR/HR coated 5.5-μm-wide 2-mm-long ridge waveguide lasers at 20 °C. Maximum power of 16 mW was obtained at the wavelength of 2.95 μm under the current of 0.5 A. The CW threshold current density was about 500 A/cm^2. The inset to Figure 4.7 shows the narrow ridge device maintains the single spatial mode operation with FWHM of about 30 °.

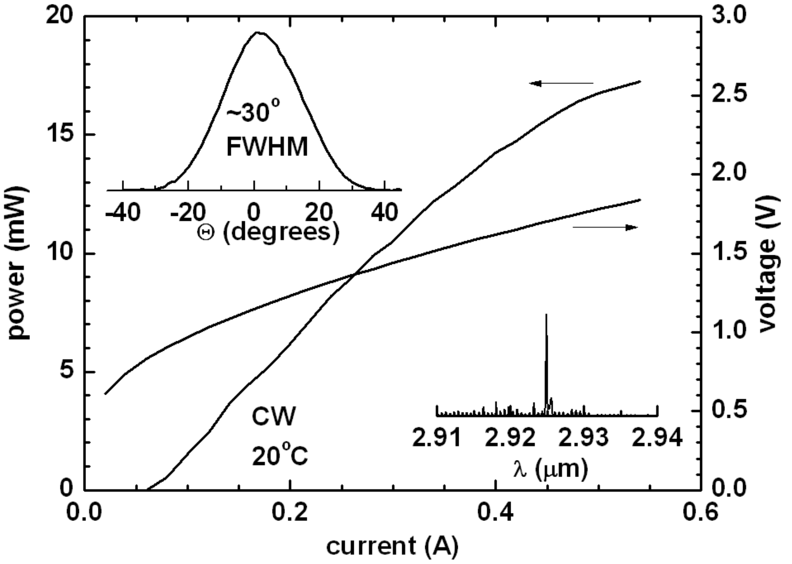

Figure 4.7 CW light-current-voltage characteristics of AR/HR coated 5.5-μm-wide 2-mm-long ridge waveguide lasers at 20 °C. Insets show the spectrum and far-field pattern.

4.2 3 μm diffraction-limited single stage diode lasers fabricated by Cl_2-free RIE

The GaSb-based diffraction limited lasers fabricated by two-step selective wet etching technique have record output power levels and extra optical loss as well [69, 70]. The devices emitting near 3 μm had ~5.5-μm-wide ridges etched down to the interface between p-cladding and waveguide core since this interface served as an etch stopper. The deep ridge design and relatively rough ridge side walls led to extra internal losses and diffraction limited devices demonstrated reduced efficiency as compared to reference 100-μm-wide ridge multimode lasers made of the same laser heterostructure material. The Cl_2-based dry etching technology enables precise control of etching profile but requires extensive operational costs.

In this section, we discuss the development of the GaSb-based diffraction-limited 3 μm lasers fabricated by ICP-RIE technique using Cl_2-free gas mixture of $H_2/CH_4/Ar$ [74]. This RIE chemistry is substantially less equipment maintenance demanding than Cl_2-based one and was previously utilized for fabrication of various devices [75] except for narrow ridge diode lasers. The ICP-RIE allowed for precise control over etching profile as well as produced much smother ridge side walls as compared to wet etching. Thus the diffraction limited diode lasers demonstrated no penalty in slope efficiency as compared to reference broad stripe multimode lasers. The 5.5-μm-wide ridge lasers generated more than twofold improved output power level of 35 mW in CW regime at 17 ℃ in the beam with slow axis divergence of about 10 °FWHM.

4.2.1 Device fabrication

The laser heterostructure used in this work was emitting near near 3 μm at RT and was grown on Tellurium-doped GaSb substrate by solid-source MBE using Veeco GEN-930 modular system equipped with valved cracker cells for both arsenic and antimony. The design of the laser heterostructure was very similar to the one reported in Ref [70]. The wafer was processed into dielectric confined ridge waveguide lasers with the ridge width of 5.5 and 100 μm wide. Broad ridge multimode lasers were used as reference devices to quantify the effect of the narrow ridge on laser parameters.

Table 4.2. Recipe of H_2/CH_4-based ICP-RIE.

$H_2/CH_4/Ar$ (sccm)	Pressure (mTorr)	RIE (W)	ICP (W)	DC bias (V)	Etching Rate (nm/min)
25/65/65	30	400	400	-400	~230

The ~300-nm-thick Si_3N_4 mask was used for ICP-RIE for both narrow and wide ridge definition. Table 4.2 shows details of the plasma etching parameters corresponding to etching rate of about 230 nm/min used in this work. The ridges were about 2.1-μm-tall that corresponded to about 250 nm of p-cladding material left on top of quinary waveguide core material outside of the ridges. The etched ridges were covered by 300 nm of Si_3N_4 and device processing was completed following standard procedure [70]. Figure 4.8 shows the SEM image of the cleaved facet of the fully processed 5.5-μm-wide ridge lasers. The SEM image confirms that sidewalls are nearly vertical and smooth. For pulsed characterizations, 1-mm-long uncoated devices were mounted epi-side up on Au-coated polished copper blocks. 2-mm-long devices with AR (~3%) and HR (~95%) coated facets were indium-soldered epi-side down for CW characterization.

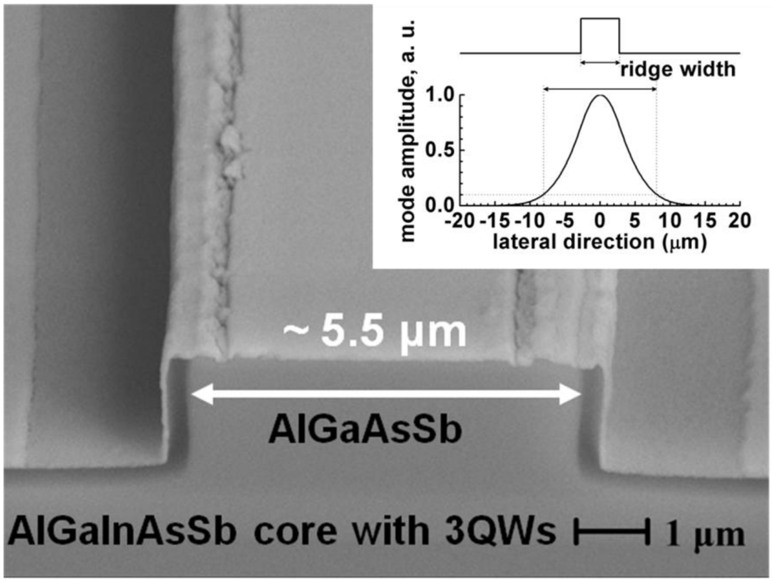

Figure 4.8 SEM image of the cleaved facet of 5.5- μm-wide ridge lasers. Inset: Simulated lateral near field pattern of 5.5- μm-wide ridge lasers.

4.2.2 Results and discussion

Figure 4.9 plots the dependence of the normalized light output (output power divided by ridge widths) on nominal current density (A/cm^2) measured in pulsed regime (100 kHz/200 ns). The 5.5 μm-wide ridge lasers demonstrate about threefold increased nominal threshold current densities as compared to 100 μm-wide ridge lasers. Both types of lasers demonstrated similar slope efficiencies of -0.15 W/A. This is in contrast to observed degradation of the slope efficiency in wet etched deep ridge lasers based on a similar laser heterostructure [70].

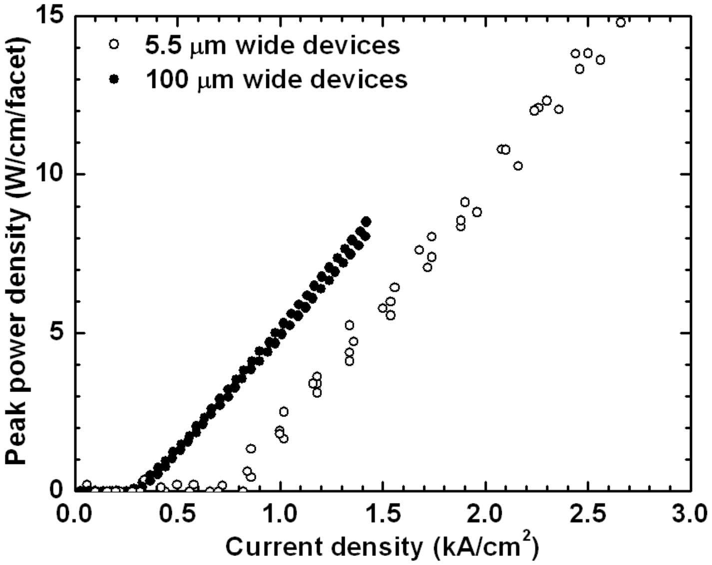

Figure 4.9 Dependences of output power density on injected current density (A/cm^2) of 1-mm-long uncoated devices under pulsed excitation (100 kHz/200 ns) at 17 ℃.

The modal gain spectra were measured using the Hakki-Paoli method [40]. Spatial filtering technique was utilized to record amplified spontaneous emission (ASE) of the fundamental lateral mode of 100-μm-wide lasers. No spatial filtering was needed to acquire high contrast ASE spectra for 5.5-μm-wide ridge devices, confirming their single spatial mode operation even below threshold. The right side of Figure 4.10 shows the modal gain spectra for 5.5 and 100 μm-wide devices, respectively. Total optical loss for the both devices was about 26 cm^{-1}. Previously reported 5.5 μm-wide deep wet etched lasers demonstrated about 8 cm^{-1} of internal loss increase as compared to reference 100-μm-wide devices [70]. Thus the efficiency of the well-controlled shallow ridge formation by Cl$_2$-free ICP-RIE was confirmed.

The left side of Figure 4.10 plots the dependence of the peak modal gain on nominal current density for the both types of devices. The nominal transparency current density increased and differential gain with respect to nominal current density decreased in 5.5 as compared to 100 µm-wide ridge devices. This can be ascribed to lateral current spreading in shallow ridge waveguide lasers. However, no penalty due to lateral current spreading was observed in the value of device slope efficiency above threshold. A possible explanation of this experimental observation is based on the match between the lateral current spreading profile and the lateral dimension of the laser mode. The simulated near field is shown in the inset to Figure 4.8 and it can be seen that the fundamental mode extends laterally over nearly three times the width of the 5.5-µm-wide ridge. Open circles in Figure 4.10 denote dependence of the peak modal gain of the 5.5-µm-wide ridge devices on threefold scaled nominal current density. It can be seen that dependence of the peak modal gain on current density for the 100-µm-wide device nearly matched the scaled version of this dependence for 5.5-µm-wide ridge devices.

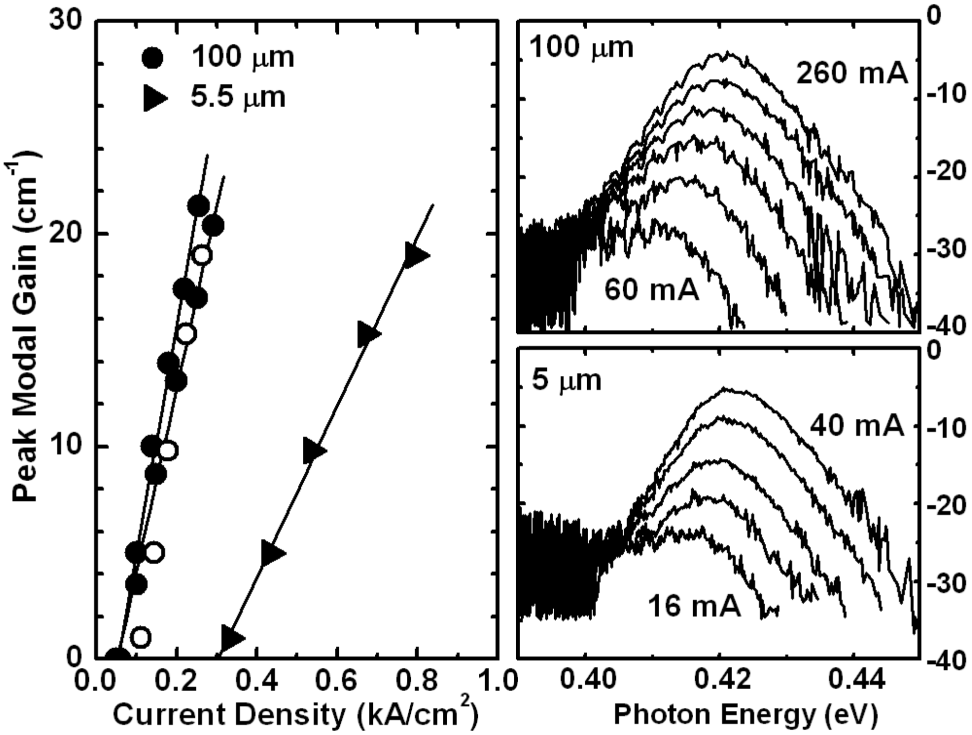

Figure 4.10 Current dependence of modal gain spectra for 5.5 and 100 µm-wide ridge devices (right side) and dependences of peak modal gain on current density (left side) for 1 mm-long uncoated devices measured at 20 ℃ in pulsed regime (2 MHz/200 ns).

The CW light-current-voltage characteristic measured for 5.5-μm-wide ridge diffraction limited lasers is shown in Figure 4.13. The devices demonstrated the record output power of 37 mW at 17 ℃. This is more than a twofold improvement as compared to the previous record of about 15 mW CW obtained for wet etched lasers [70]. The dry etched devices maintained the single spatial mode operation with 10 ° FWHM far-field pattern (inset to Figure 4.13) from threshold to the current corresponding to the maximum output power. The measured lateral far-field pattern is nearly matched to simulation results based on the near-field profile shown in Figure 4.8 (inset to Figure 4.13).

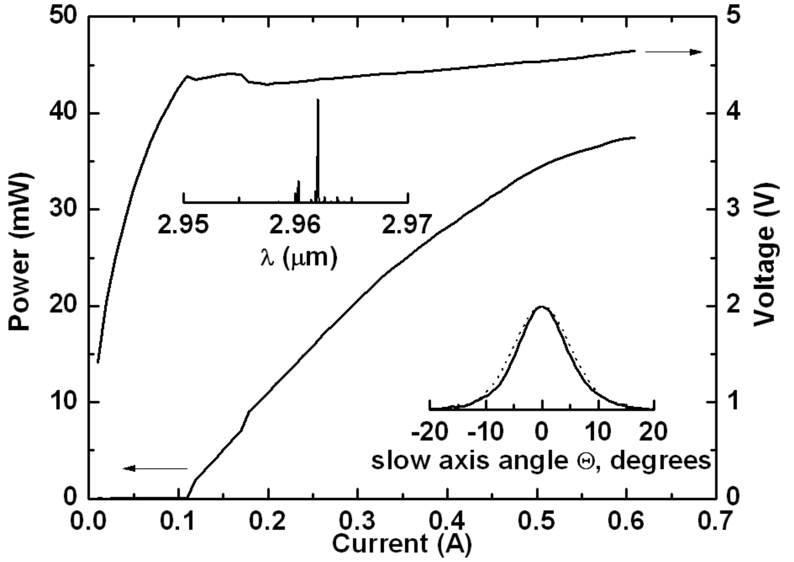

Figure 4.11 CW light-current-voltage characteristics of AR/HR coated 5.5 μm wide 2 mm-long devices measured at 17 ℃.

The CW output power of the dry etched devices was limited by thermal rollover caused by excessive voltage drop. The IV characteristics of the 5.5-μm-wide ridge laser and properly scaled version of the IV of the reference 100-μm-wide ridge shown in Figure 4.13 are very different. The ICP-RIE procedure used in this work led to plasma induced increase of the turn-on voltage in narrow ridges presumably due to surface ion-induced damage and/or hydrogen passivation of the p-contact layers. Once the RIE induced extra voltage drop across narrow ridge lasers is eliminated a further twofold improvement of the CW output power level could be expected.

4.3 3.15 µm diffraction-limited two-stage cascade lasers fabricated by $SiCl_4$-based RIE

The 5-µm-wide diffraction limited single stage diode lasers fabricated by Cl_2-free H_2/CH_4/Ar RIE-ICP demonstrated 37 mW of CW output power at 17 ℃, and single mode far-field pattern. However, due to the surface ion-induced damage and/or hydrogen passivation of the p-contact layers, the as-fabricated devices suffer a high-voltage issue, which is unfavorable for high power operation. This result indicates that the Cl_2-free H_2/CH_4/Ar RIE-ICP is good to define the narrow ridge profile, but inappropriate to the devices aiming for high power CW operation in RT. New dry etching technique is needed.

In this section, we discuss the development of 3.15 µm diffraction-limited lasers using two-stage cascade structure which are fabricated by Cl_2-based ICP-RIE [76]. The development Cl_2-based ICP-RIE technique is done at Center for Functional Nanomaterials (CFN), Brookhaven National Laboratory (BNL), for the purpose of eliminating surface ion-induced damage and/or hydrogen passivation of the p-contact layers by Cl_2-free H_2/CH_4/Ar RIE-ICP, and improving the devices CW output power in RT, together with the cascade design. We demonstrate that cascade pumping scheme is capable of multifold improvement of the type-I QWs diode laser efficiency at longer wavelength and it is compatible with shallow ridge waveguide fabrication of diffraction limited emitters. The 6-µm-wide ridge waveguide lasers were fabricated by Si_3Cl_4-based ICP-RIE. The narrow ridge lasers generated more than 40 mW of CW power at RT in diffraction limited beam, which was more than a fourfold improvement comparing to the previously reported 9 mW obtained from 3.15 µm narrow ridge single stage diode lasers [73].

4.3.1 Device fabrication

The laser heterostructure was grown by solid-source MBE on Te-doped GaSb substrates. The laser heterostructure used here is the same to the 3.1 µm two-stage cascade laser discussed in section 3.3.3, and the 100-µm-wide multimode devices are used as reference here. The ~6-µm-wide narrow ridge diffraction-limited devices (Figure 4.14) were fabricated by Si_3Cl_4-based ICP-RIE in Oxford Plasmalab System 100 at CFN, BNL. The RIE recipe is shown in Table 4.3. The etching rate was ~800 nm/min.

Table 4.3. Parameters of $SiCl_4$-based ICP-RIE.

$SiCl_4/N_2/Ar$ (sccm)	Pressure (mTorr)	RIE (W)	ICP (W)	DC bias (V)	Etching Rate (nm/min)
10/5/20	2	60	250	-210	~800

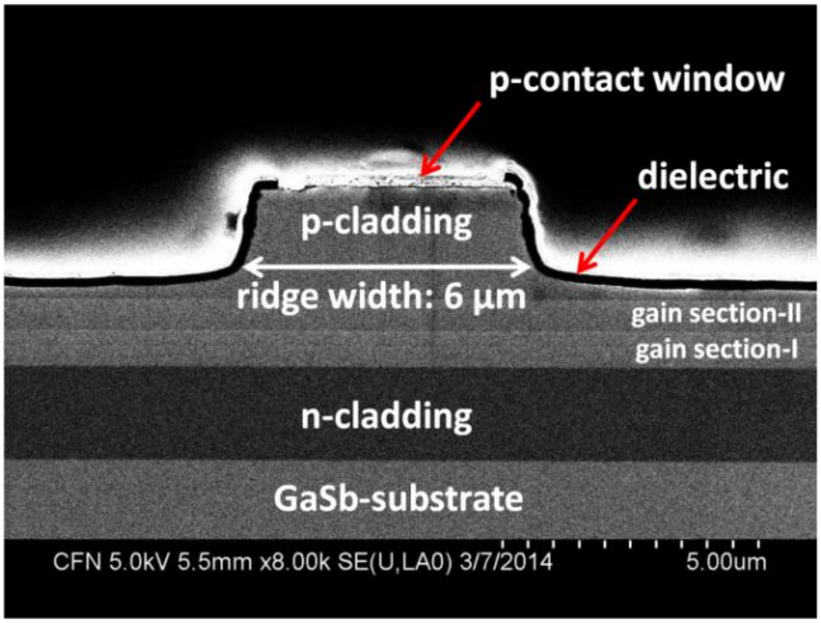

Figure 4.12 SEM image of the as cleaved mirror of the narrow ridge waveguide diode laser showing ridge width of ~6 µm.

The uncoated 1-mm-long devices were indium soldered epi-up for pulsed characterization (200 ns/100-500 kHz). The AR/HR (~5% and ~95%) coated 2-mm-long devices were indium soldered epi-down for characterization in CW regime.

4.3.2 Results and discussion

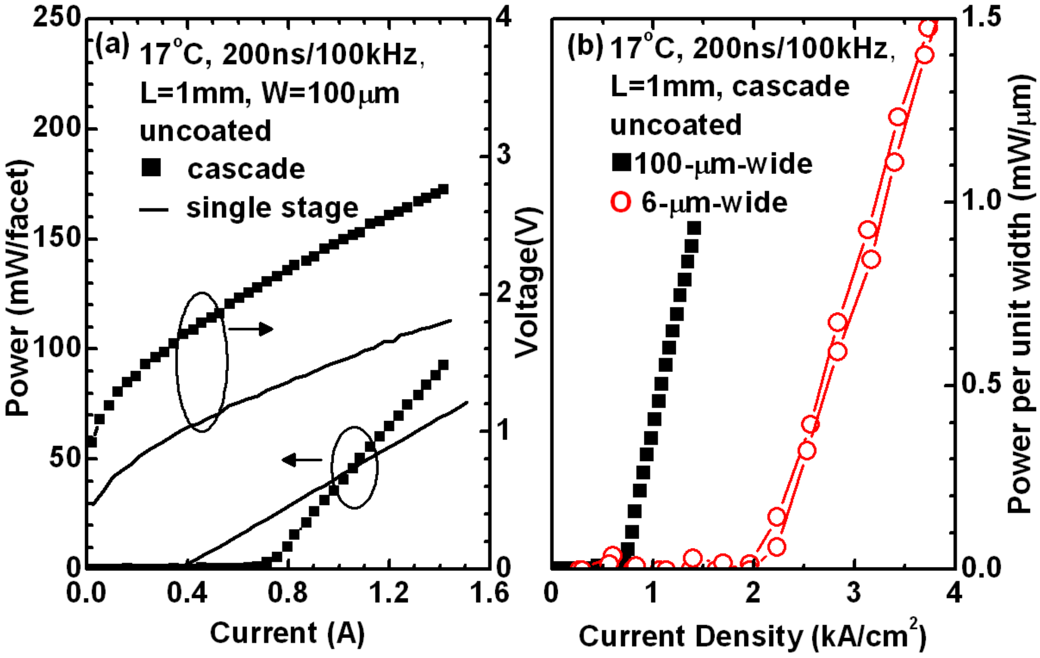

Figure 4.13 (a) Light-current-voltage characteristics measured at 17 ℃ in short pulse regime (200 ns/100 kHz) for 1-mm-long, uncoated 100-µm-wide two-stage cascade device (square), and 100-µm-wide single stage device (line). (b) Dependence of normalized output power density on nominal current density (kA/cm^2) of 1 mm-long uncoated 100- (square) and 6-µm-wide (circle) cascade lasers measured under the same condition (200 ns/100 kHz, 17 ℃).

Figure 4.13 shows the light-current-voltage characteristics measured in pulsed regime (200 ns/100 kHz) at 17 ℃ for the uncoated 1-mm-long, 100-µm-wide two-stage cascade devices and reference single stage diode lasers [28]. Twofold improvement of the device slope efficiency was observed in the two-stage cascade lasers. Figure 4.13 (b) plots the normalized light-current characteristics (output power per unit width of the ridge versus current divided by nominal contact area) measured in pulsed regime (200 ns/100 kHz, 17 ℃) for the broad and narrow ridge cascade lasers. Narrow ridge lasers demonstrated about threefold increase of the nominal threshold current density and about 30% decrease of slope efficiency as compared to the 100-μm-wide cascade lasers. Parameters T_0 and T_1 measured in temperature range from 15 to 50 ℃ for the broad ridge cascade lasers were 42 K and 90 K, respectively.

The current dependences of the laser modal gain spectra (Figure 4.14) were determined by the Hakki-Paoli method [40]. Spatial mode filtering optics was used to measure amplified spontaneous emission (ASE) spectra of broad ridge multimode lasers, while the corresponding measurements of the narrow ridge devices required no modal filtering to obtain high contrast ASE spectra. Thus the single spatial mode operation below threshold was confirmed. The total loss, estimated from the long wavelength part of the modal gain spectra, was about 21 cm^{-1} for 100-μm-wide (Figure 4.14 (b)) and 27 cm^{-1} for 6-μm-wide cascade lasers (Figure 4.14 (c)), respectively. Assuming the mirror loss was about 12 cm^{-1} for 1-mm-long uncoated devices, the internal optical loss of 9 cm^{-1} could be calculated for the broad ridge cascade lasers. For the 6-μm-wide cascade lasers, the internal optical loss was about 15 cm^{-1}. Given the measured slope efficiency and optical loss, the internal quantum efficiencies for both broad and narrow ridge devices were calculated as 110-120%. Internal efficiency of the reference single stage lasers was ~55%. Twofold improvement of the internal efficiency in two-stage cascade devices confirms 100% efficient carrier recycling between stages.

The dependence of the peak modal gain on nominal current density is plotted in Figure 4.14 (a) for the broad and narrow ridge devices. The nominal transparency current density increased and differential gain with respect to nominal current density decreased nearly twofold in 6-μm-wide narrow ridge devices as compared to 100-μm-wide ones. This could be explained by the lateral current spreading of the narrow ridge lasers. Certain amount of the lateral current spreading is beneficial for the narrow ridge devices with lateral mode width exceeding the ridge width. The peak modal gain versus twofold scaled current density is plotted in Figure 4.14 (a) and it nearly matches the corresponding dependence of broad ridge devices (open triangle in Figure 4.14(a)). The higher values of thus scaled threshold current density of the narrow ridge lasers as compared to that of broad ridge ones results from increased internal optical loss.

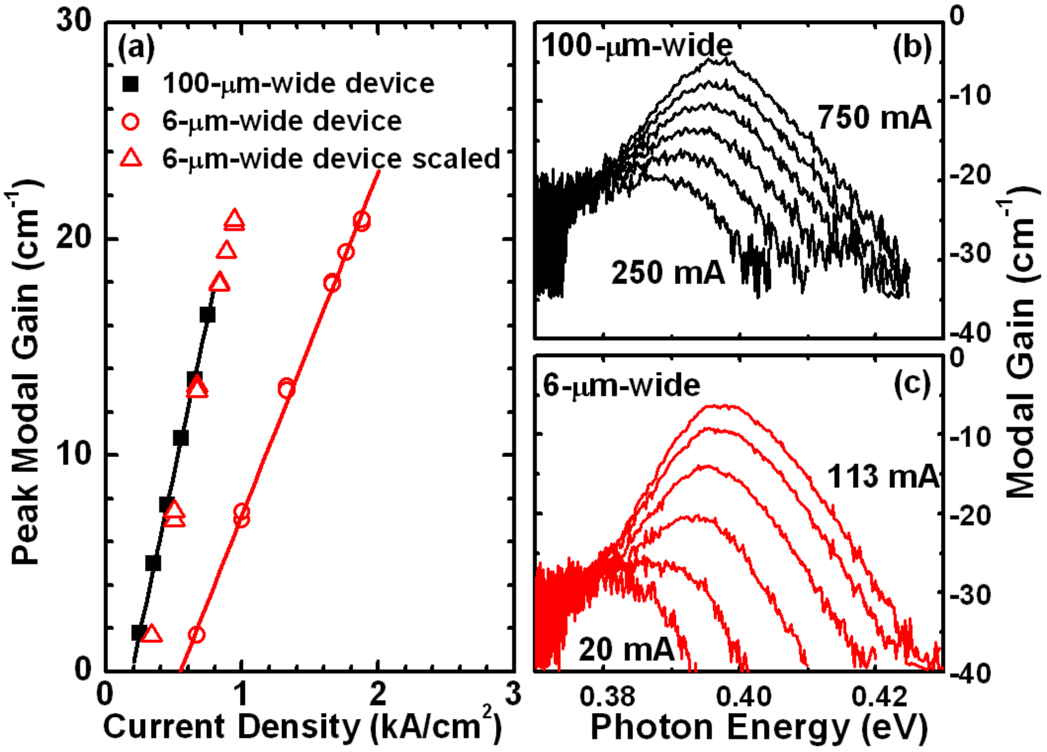

Figure 4.14 (a) Dependences of peak modal gain on current density for 1-mm-long uncoated, 100- (square) and 6-μm-wide (circle, scaled version in triangle) devices measured at 17 ℃ in pulsed regime (200 ns/500kHz). (b) Current dependence of modal gain spectra for 100-μm-wide cascade lasers and (c) 6-μm-wide cascade lasers at 17 ℃ in 200 ns/500kHz.

The far-field patterns of narrow ridge devices were measured by means of scanning the single photodetector (Figure 4.15). The current independent single lobe far-field pattern confirmed stable single spatial mode operation above threshold. The divergence angle in slow axis was ~11 ° FWHM and ~67 ° FWHM in fast axis (Figure 4.15 (a)). Fast axis far-field divergence angle of the single stage lasers was somewhat wider (>70 ° FWHM) because of narrower waveguide core width and, hence, narrower vertical near field as compared to cascade devices. The magnified lateral near-field patterns were measured by FLIR SC6700 infrared camera (Figure 4.15b). The near-field images were also current independent with about 6 μm FWHM in slow axis direction. The full width (defined at $1/e^2$ of the maximum intensity) of this fundamental mode was about ~11 μm. Thus, the lateral current spreading (assumed above in the context of Figure 4.14 (a) data) leading to twofold increase of the effective current path cross-section is beneficial.

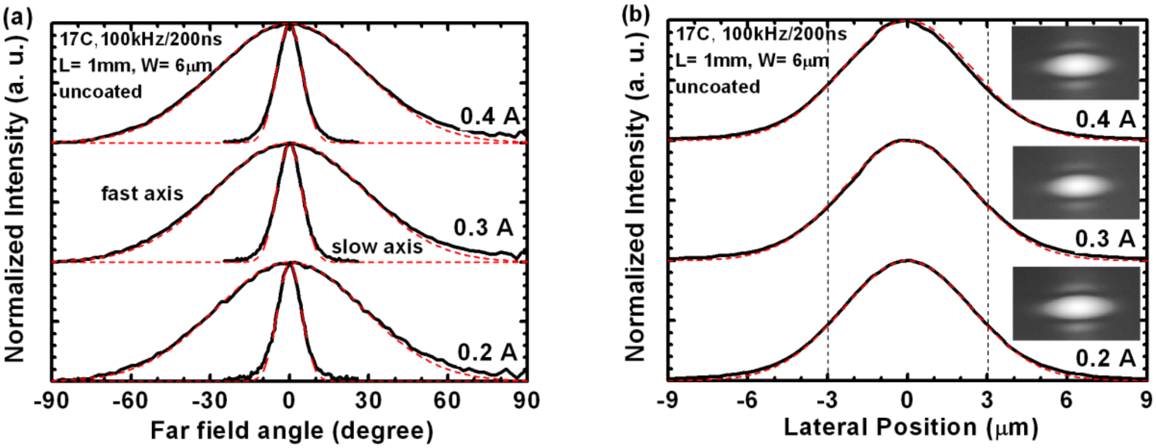

Figure 4.15 (a) Fast and slow axis far-field pattern (solid lines) of narrow ridge two-stage cascade diode lasers (epi-up mounted) measured at different currents at 17 ℃. The dash lines are the Gaussian fit. (b) Current dependence of the lateral profiles of near field intensity measured at 17 ℃, two vertical dash lines indicate the nominal narrow ridge width, the dash lines are the Gaussian fit. The insets show the near filed image.

In order to understand the nature of the extra ~7 cm^{-1} of internal optical loss observed in narrow ridge lasers, the modal structure was simulated using BeamPROP [77]. Since the ridge sidewalls were not perfectly vertical (Figure 4.12), a stepped model of ridge was used (Figure 6a). The refractive indices of the materials used in the simulation are shown in Table 4.4. The refractive indices (both *n* and *k*) of metals (Ti/Pt/Au) and Si_3N_4 were taken from Ref. [78]. The real parts of the refractive indices of individual semiconductor layers were estimated following Ref [39]. The refractive index of quinary AlGaInAsSb alloy was estimated to be the same to that of GaSb (~3.82). This estimation is somewhat justified by the fact that both materials have nearly the same bandgap according to our photoluminescence studies. The imaginary parts of the refractive indices of individual layers were calculated from the corresponding absorption coefficients, which were firstly estimated from Ref. [79] and then adjusted based on the comparison of simulation with experimental results.

Table 4.4. Real (n) and imaginary (k) parts of material refractive indices used in the simulation.

Material	n	k
Au	1.62	19.72
Pt	3.10	10.95
Ti	2.40	4.56
Si_3N_4	1.98	0
GaSb cap (10^{19} cm^{-1} doped)	3.82	0.33
p-cladding (10^{18} cm^{-1} doped)	3.23	0.033
p-cladding (10^{17} cm^{-1} doped)	3.23	0.0033
quinary waveguide	3.82	0
injector	3.82	0.0017
n-cladding (10^{18} cm^{-1} doped)	3.23	0.033

The far-field and near-field patterns generated from the stepped narrow ridge model are shown in Figure 4.16 (b) and (c). The far-field pattern indicated a FWHM divergence angle of ~11.9 ° on slow axis and ~69 ° on fast axis. The near-field pattern showed a FWHM width of ~6 μm on lateral direction. The simulation results are in agreement with the experimental results (Figure 4.15). The calculated internal optical loss for 100-μm-wide cascade lasers was about 9 cm^{-1} (k = 0.000222), matching the value estimated by Hakki-Paoli method. However, the calculation did not predict ~6 cm^{-1} increase of the internal loss for 6-μm-wide lasers. The calculation predicted the experimental values of the internal optical loss for narrow ridge lasers when absorption coefficients were artificially scaled up 10 times in the stepped sidewall parts of the ridge model (Figure 4.16 (a)). Excessive sidewall scattering can account for reduced Diffraction-Limited device efficiency and thus should be minimized through etching process optimization.

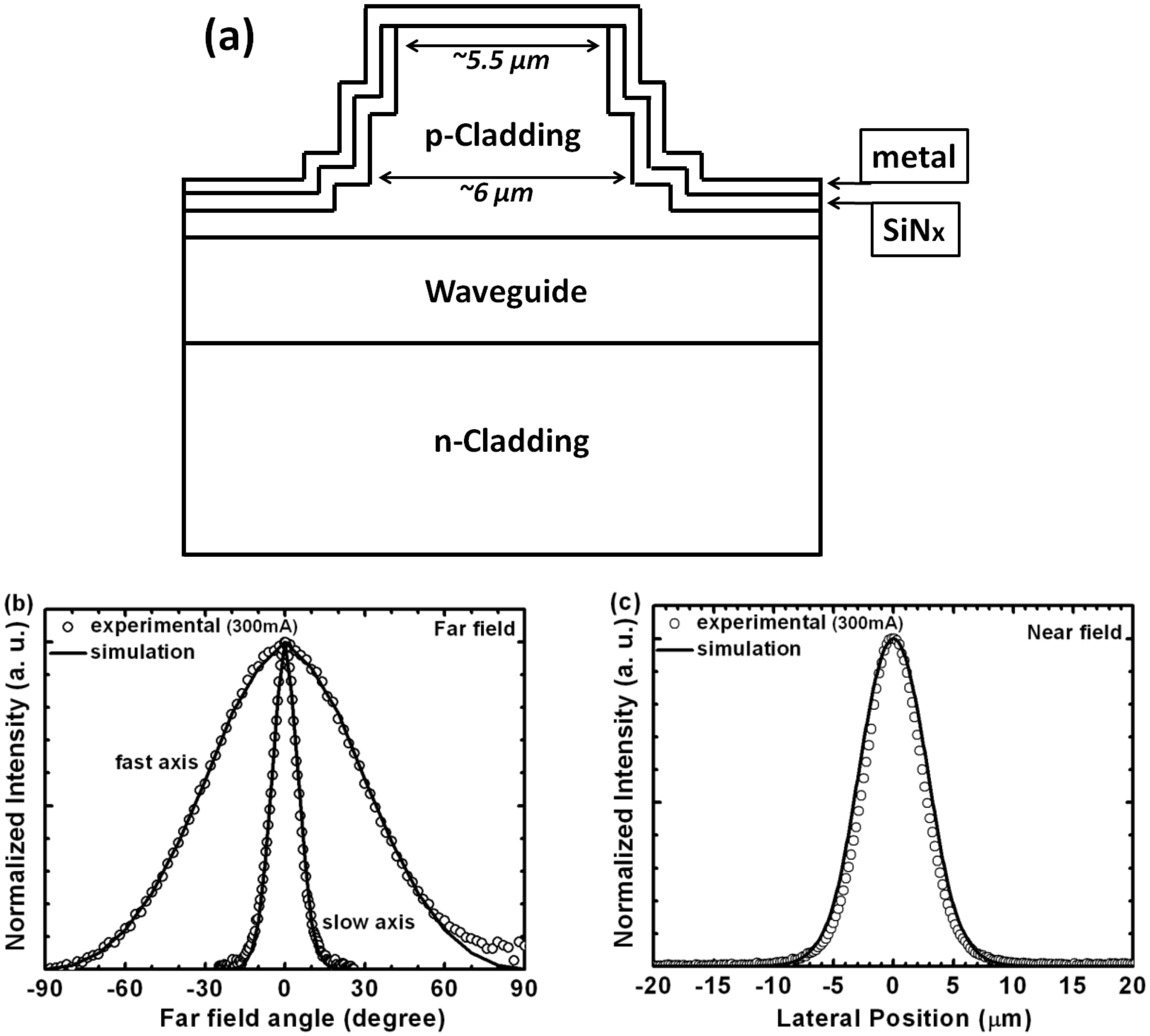

Figure 4.16 (a) Schematic cross section view of the stepped model for the6- μm-wide narrow ridge lasers. (b) Far- and (c) near-field pattern simulated by BeamPROP. The experimental results are shown in circle.

The far-field and near-field patterns generated from the stepped narrow ridge model are shown in Figure 4.16 (b) and (c). The far-field pattern indicated a FWHM divergence angle of ~11.9 ° on slow axis and ~69 ° on fast axis. The near-field pattern showed a FWHM width of ~6 μm on lateral direction. The simulation results are in agreement with the experimental results (Figure 4.15). The calculated internal optical loss for 100-μm-wide cascade lasers was about 9 cm^{-1} (k = 0.000222), matching the value estimated by Hakki-Paoli method. However, the calculation did not predict ~6 cm^{-1} increase of the internal loss for 6-μm-wide lasers. The calculation predicted the experimental values of the internal optical loss for narrow ridge lasers when absorption coefficients were artificially scaled up 10 times in the stepped sidewall parts of the ridge model (Figure 4.16 (a)). Excessive sidewall scattering can account for reduced Diffraction-Limited device efficiency and thus should be minimized through etching process optimization.

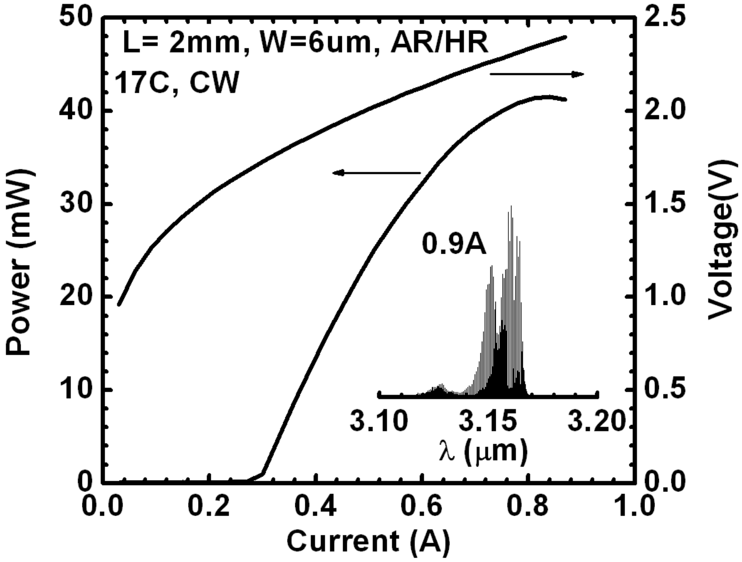

Figure 4.17 CW power-current-voltage characteristics of 2-mm-long AR/HR coated narrow ridge cascade lasers at 17 ℃ (inset shows the emission spectra at 0.9 A).

Light-current-voltage characteristics in CW regime at 17 ℃ were measured for the AR/HR coated 2-mm-long narrow ridge devices (Figure 4.17). The laser's spectrum was centered near 3.15 μm at 0.9 A (inset to Figure 4.17). The CW output power reached 42 mW.

4.4 3.27 µm DFB diode lasers fabricated by $SiCl_4$-based RIE

The Si_3Cl_4-based ICP-RIE was used to successfully fabricate ~6-µm-wide narrow ridge two-stage cascade lasers with decent diffraction-limited output power. This result validates the application of Si_3Cl_4-based ICP-RIE on processing for narrow ridge waveguide and other fine feature.

With this Si_3Cl_4-based ICP-RIE and the narrow ridge lasers technique we have demonstrated before, we will develop DFB lasers. Robust and efficient single spectral mode 3.27 µm diode lasers operating near RT in CW regime are required for methane TDLAS. Both DFB and external cavity single frequency diode lasers operating in CW near RT near methane absorption band were reported [65, 66, 80, 81]. The available CW output power was limited to several mW so far though higher values are often desirable for improved system sensitivity.

In this section we discuss the design and development of the 3.27 µm emitting DFB lasers based on efficient diode laser heterostructure similar to one reported [11]. The devices demonstrate single frequency operation in wide temperature range with CW output power level well above 15 mW. Lasers operated in multimode CW regime below -30 ℃ and above +20 ℃ because of gain detuning from ~3.27 µm DFB line.

4.4.1 Device fabrication

Three QWs laser heterostructure was grown by solid-source MBE on Te-doped GaSb substrates. Narrow ridge waveguide laterally coupled distributed feedback lasers were defined by e-beam lithography and fabricated by Si_3Cl_4-based ICP-RIE in Oxford Plasmalab System 100 at CFN, BNL. The etching was performed using ~300-nm-thick Si_3N_4 masks and under conditions given in Table 4.3.

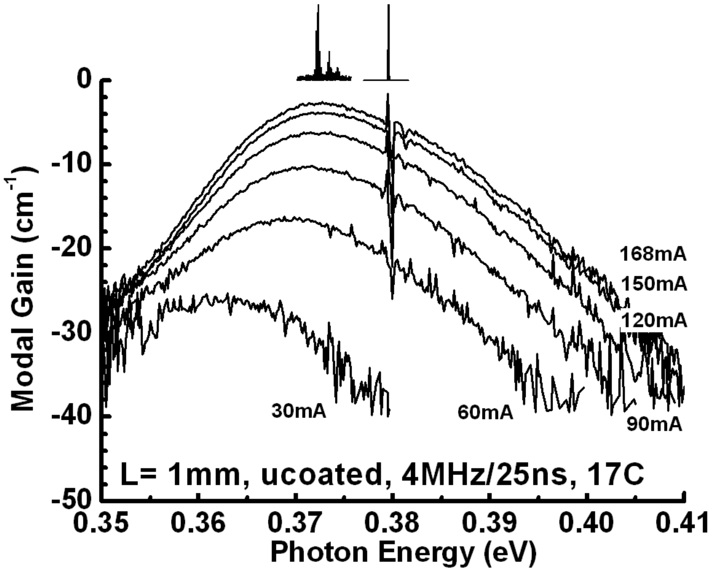

Figure 4.18 Current dependence of modal gain spectra for 1-mm-long, uncoated DFB diode lasers. Insert shows the lasing spectra corresponding to operation at Fabry-Perot cavity mode and at grating defined Bragg wavelength.

Narrow (~6-µm-wide) ridge lasers emitted in fundamental mode below and above threshold. Modal gain spectra were measured by Hakki-Paoli technique [40] with no spatial filtering applied thanks to stable single spatial mode operation. The parameters of compressively strained GaInAsSb QWs yielded the modal optical gain peak near 3.33 µm (372 meV) at 17 °C (Figure 4.18). The grating related distortion near 3.27 µm (379 meV) was apparent in measured gain spectra. The mode frequency was enforced by index grating with period of 480 nm etched on both sides of narrow ridge waveguide (Figure 4.19). Measured lateral near field pattern (insert to Figure 4.19) confirmed that extension of the lateral grating by ~10 µm from the ridge sidewalls was adequate to couple most of the optical field. The coupling coefficient κ was estimated to be ~8 cm^{-1} following Ref. [82]. The overlap of the fundamental mode with grating region of ~0.15% was estimated based on measured lateral near field distribution and calculated vertical near field distribution calibrated by measured fast axis far field pattern.

The uncoated 1-mm-long devices were indium soldered epi-up for pulsed characterization (200 ns/100-500 kHz). The AR/HR (~5% and~95%) coated 2-mm-long devices were soldered epi-down onto polished gold plated copper blocks for characterization in CW regime.

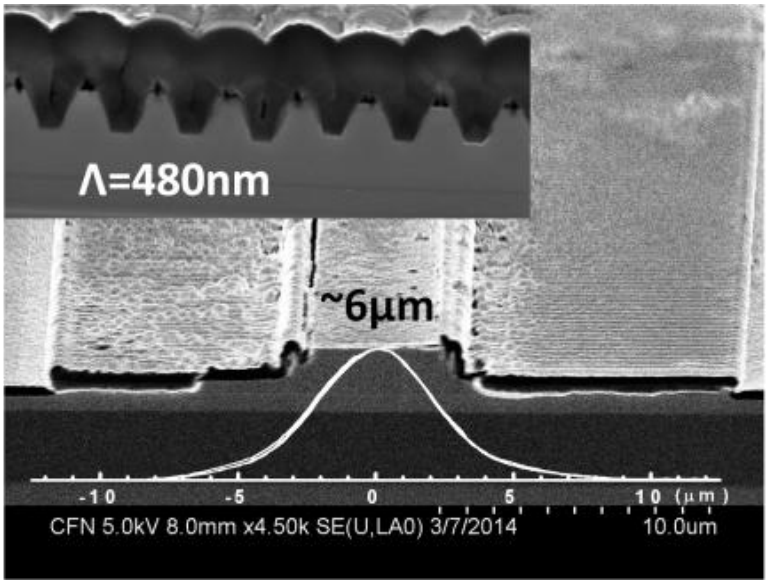

Figure 4.19 SEM image of as cleaved mirror of the fully processed DFB diode laser. The upper inset shows the cross section view of etched gratings. The lower insert shows the lateral near-field profiles measured for currents in the range from 200 to 500 mA at RT.

4.4.2 Results and discussion

Figure 4.20 shows the light-current-voltage characteristics measured in CW regime for the AR/HR coated 2-mm-long devices. Single frequency output power reached above 10 mW and 40 mW at +20 ℃ and -20 ℃, respectively. The inserts to Figure 4.20 show the representative laser spectrum and lateral far field pattern. The devices demonstrated stable single frequency operation for the detuning less than about ~3 meV at -30 ℃ and less than ~7 meV at 20 ℃ (Figure 4.21). The asymmetry is explained by combination of the steeper decrease of the gain at blue side of the spectrum and temperature dependence of the gain bandwidth.

Modal gain spectra measured at 17 ℃ (Figure 4.18) allowed estimating the total loss of Fabry-Perot cavity (from long wavelength part of the gain spectra) to be about ~ 27 cm^{-1}. Assuming the mirror loss of about 12 cm^{-1} for 1-mm-long uncoated devices, the internal optical loss of ~15 cm^{-1} could be calculated. This value was comparable to that obtained for 3.15 μm emitting narrow ridge lasers without gratings fabricated with the similar ridge geometry and etching technique [76]. Thus the addition of the lateral index gratings did not result in much noticeable increase of internal optical loss, in contrast to the laterally coupled DFB lasers based on metal gratings [83, 84].

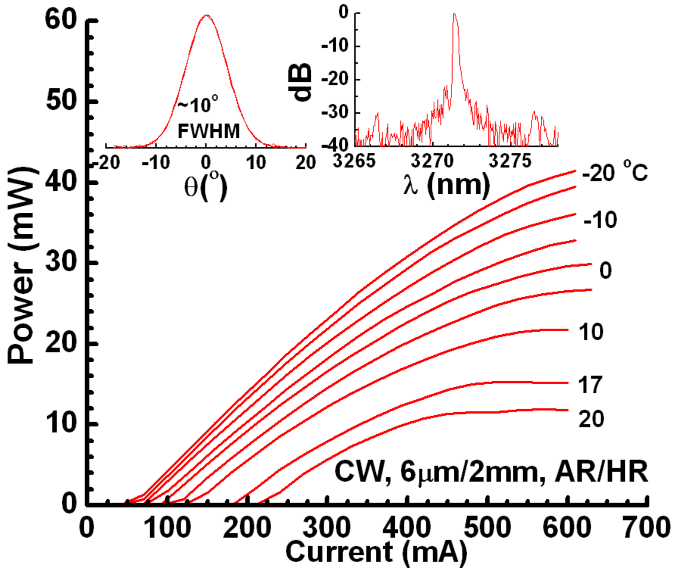

Figure 4.20 CW power-current characteristics of 2-mm-long AR/HR coated DFB diode lasers measured in temperature range from -20 to 20 ℃. The insert on right shows the laser spectrum measured at 17 ℃ at 400mA of CW current. The insert on left shows the slow axis far-field pattern measured in current range from 300 to 500 mA at RT.

The difference in optical gain at peak and at DFB line of about 3 cm^{-1} at 17 ℃ (Figure 4.18) can serve as an estimation of the effect of the grating distributed reflection on net mirror loss. At 17 ℃, somewhat under coupled lasers with cavity length L = 1mm operated often at both FP and DFB modes simultaneously (insert to Figure 4.18). Thus, the gain difference of ~3 cm^{-1} determined the critical detuning value. By lowering the operating temperature, the detuning decreased and better coupled 2-mm-long (κ*L>1.5) devices operated in stable continuously tunable DFB mode from threshold to maximum power level (Figure 4.21). It should be noted that 2-mm-long lasers used for CW characterization were AR/HR coated and thus operated in energy gap mode regime naturally characterized by improved stability [85]. Bragg wavelength of about 3.27 μm allowed estimating the fundamental mode effective index as ~3.41 at RT. The temperature tuning rate of Bragg wavelength was ~0.27 nm/K (Figure 4.21) - value comparable to the tuning characteristics of GaSb-based DFB lasers of shorter wavelength [86]. DFB lasers discussed were operating in negative detuning regime (Figure 4.18) at RT which has advantage of the improved differential gain and, thus, minimized linewidth enhancement factor [87-89]. However, excessive detuning at 20 ℃ leads to operation at Fabry-Perot cavity modes at currents above 300 mA (insert to Figure 4.21).

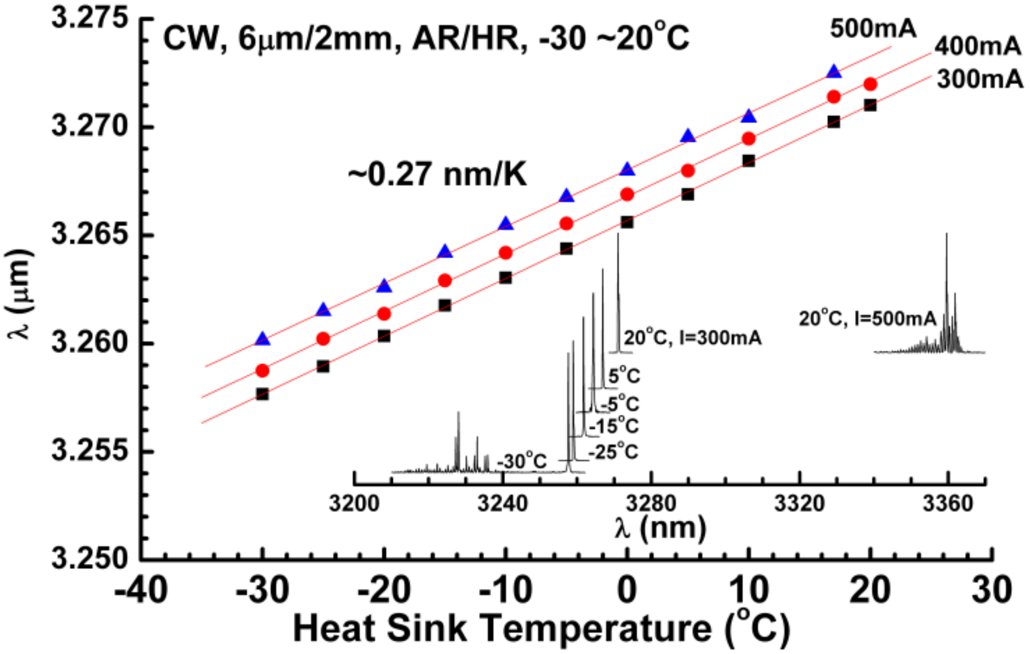

Figure 4.21 Temperature dependences of the Bragg wavelength measured at CW currents of 300, 400 and 500 mA – corresponding to output power greater than 10 mW. Insert shows the temperature dependence of the laser spectra measured at CW current of 300 mA..

4.5 3 μm diffraction-limited two-stage cascade lasers fabricated by BCl$_3$/Cl$_2$-based RIE

With the Si$_3$Cl$_4$-based ICP-RIE technique, 3.15 μm diffraction-limited two-stage cascade lasers and 3.27 μm DFB diode lasers were fabricated and demonstrated decent CW output power and performance. However, due to the roughness and non-vertical sidewall from this etching technique, the narrow ridge lasers demonstrated extra optical loss as compared to the broad ridge lasers. Since the dry-etched devices somehow suffer the similar extra optical loss issue with the wet-etched narrow ridge devices, another Cl_2-based ICP-RIE technique was developed using BCl_3/Cl_2 gas mixture. With this new Cl_2-based ICP-RIE technique, diffraction-limited devices with narrow ridge waveguide are expected to have vertical sidewall, and no extra optical loss. The DFB grating teeth fabricated by new dry etching are expected to have rectangular shape, rather than trapezoid.

In this section, we discuss the 3 μm diffraction-limited two-stage cascade lasers fabricated by BCl_3/Cl_2-based ICP-RIE. The narrow ridge of the devices has near perfectly vertical sidewalls, and no extra optical loss is observed as compared to the broad ridge devices from the same laser heterostructure. The AR/HR coated 2-mm-long narrow ridge two-stage cascade lasers demonstrated diffraction limited output power of 107 mW in CW regime at RT, which is a threefold increase as compared to the previous reported 3 μm diffraction-limited two-diode lasers [74].

4.5.1 Device fabrication

The 3 μm laser heterostructure used here is the same to the 3. μm two-stage laser with optimized cascade structure discussed in section 3.3.4, which has demonstrated outstanding efficient and CW output power. The 100-μm-wide multimode devices are used as reference here. The BCl_3/Cl_2-based ICP-RIE was developed and optimized on the Oxford Plasmalab System 100 at CFN, BNL, and ~5-μm-wide narrow ridge diffraction-limited devices were fabricated. The RIE recipe is shown in Table 4.5. The etching rate was ~500 nm/min.

Table 4.5. Recipe of BCl_3/Cl_2-based ICP-RIE.

$BCl_3/Cl_2/Ar$ (sccm)	Pressure (mTorr)	RIE (W)	ICP (W)	DC bias (V)	Etching Rate (nm/min)
10/5/17	2	200	300	-450	~500

The SEM image (Figure 4.22 (a)) shows the cleaved narrow ridge fabricated by this dry etching. The vertical sidewall of the narrow ridge indicated the BCl_3/Cl_2-based ICP-RIE has good control on etch profile, and could be utilized to fabricate rectangle-shaped DFB grating teeth with vertical sidewalls (Figure 4.22 (b)).

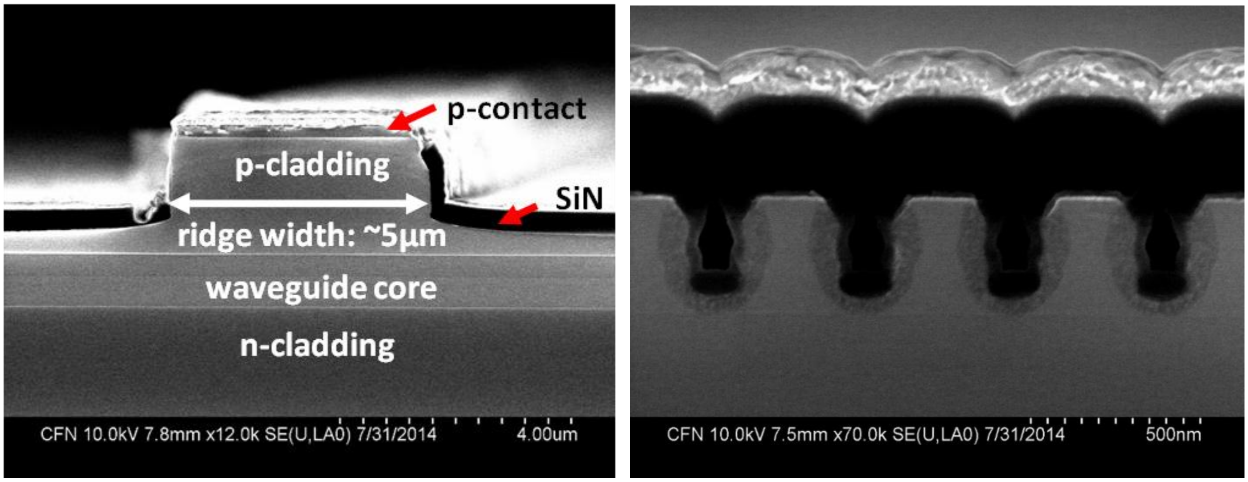

(a) (b)

Figure 4.22 SEM image of (a) the as cleaved mirror of the narrow ridge waveguide λ~ 3 µm two-stage cascade laser showing ridge width of ~5 µm; (b) the side view of the cleaved DFB grating teeth fabricated by the BCl_3/Cl_2-based ICP-RIE in pre-study experiment.

4.5.2 Results and discussion

The current dependences of the laser modal gain spectra (Figure 4.23) determined by the Hakki-Paoli method [40]. were compared for 100- and 5-µm-wide devices. Spatial mode filtering optics was used to measure amplified spontaneous emission (ASE) spectra of broad ridge multimode lasers, while the corresponding measurements of the narrow ridge devices required no modal filtering to obtain high contrast ASE spectra. Thus the single spatial mode operation below threshold was confirmed. The total loss, estimated from the long wavelength part of the modal gain spectra, was about 21 cm^{-1} for both 100- and 5-µm-wide cascade lasers (Figure 4c), respectively, and the internal optical loss of 9 cm^{-1} could be calculated. Thus, no extra optical loss was observed for the 5-µm-wide cascade lasers, the efficiency of the well-controlled narrow ridge and vertical sidewalls formation by BCl_3/Cl_2-based ICP-RIE was verified.

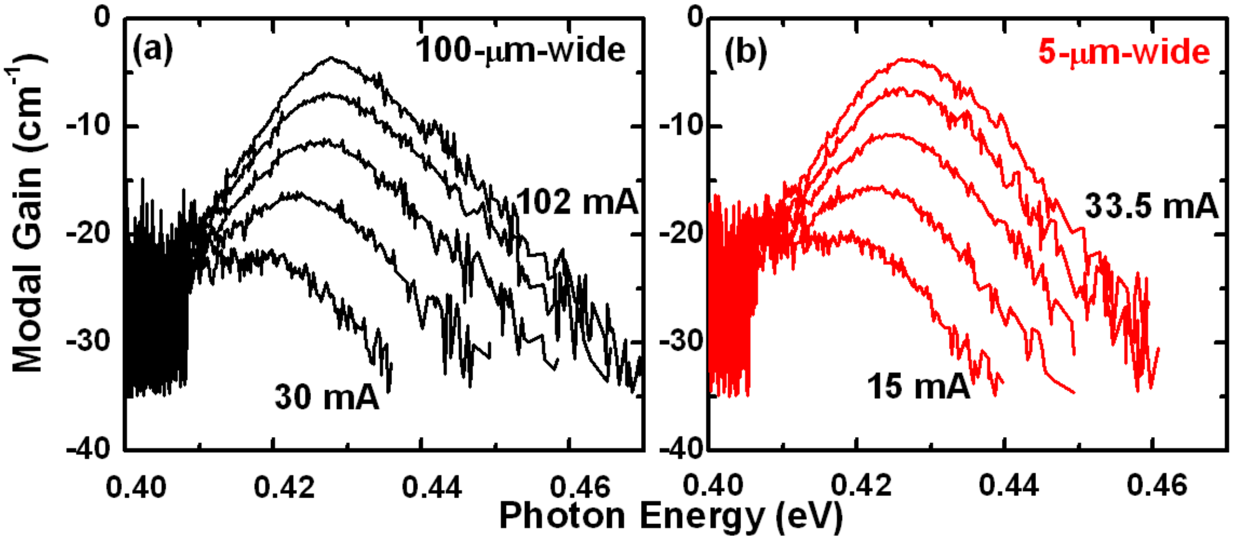

Figure 4.23 Current dependence of modal gain spectra for (a) 100-µm-wide (b) 6-µm-wide cascade lasers at 17 ℃ in 200 ns/500kHz.

The far-field patterns of narrow ridge devices were measured by means of scanning the single photodetector (Figure 4.24) for both fast and slow axis at several currents. The current independent single lobe far-field pattern confirmed stable single spatial mode operation above threshold. The divergence angle in slow axis was ~8 °FWHM and ~69 °FWHM in fast axis. This result verified that these narrow ridge devices operated with diffraction-limited mode.

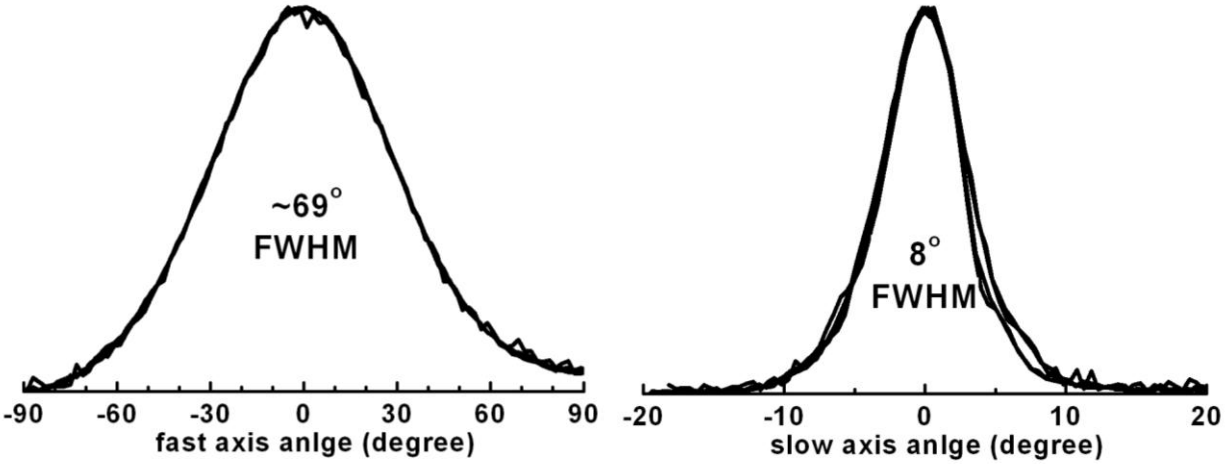

Figure 4.24 (a) Fast and (b) slow axis far-field pattern of narrow ridge two-stage cascade diode lasers (epi-up mounted) measured at different currents at 17 ℃.

L-I-V characteristics in CW regime at 17 ℃ were measured for the AR/HR coated 2-mm-long narrow ridge devices (Figure 4.25). The maximum CW output power reached 107 mW, which is a threefold increase as compared to the previous reported 37 mW from 3 μm diffraction-limited two-diode lasers fabricated by Cl_2-free ICP-RIE [74].

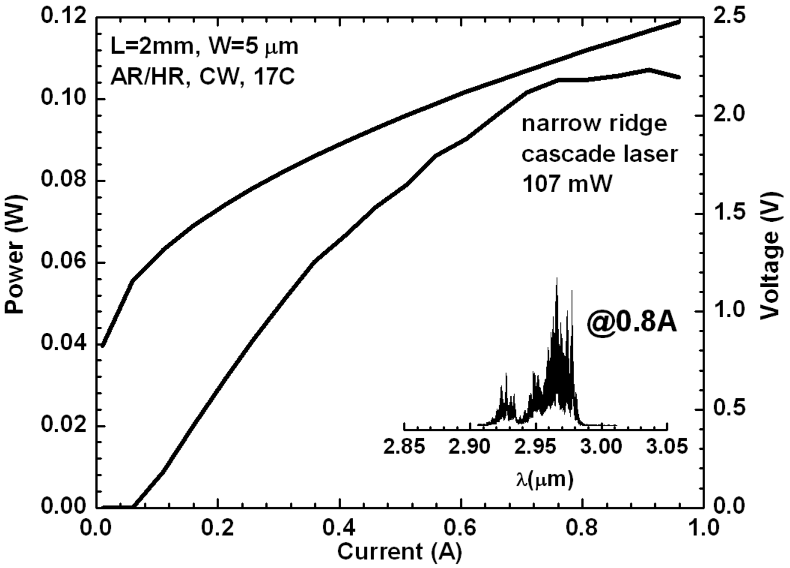

Figure 4.25 CW power-current-voltage characteristics of 2-mm-long AR/HR coated narrow ridge cascade lasers at 17 ℃ (inset shows the emission spectra at 0.8 A).

4.6 Conclusion

In this chapter, we discussed the design and fabrication of several diffraction-limited and distributed feedback diode lasers using single stage diode and two-stage cascade heterostructures. The narrow ridge waveguide of diffraction-limited lasers were fabricated by different etching techniques, including two-step selective wet etching, Cl_2-free H_2/Ch_4-based ICP-RIE, $SiCl_4$-based ICP-RIE, and BCl_3/Cl_2-based ICP-RIE, which were developed to improve the etching profile and lasers performance.

Diffraction-limited narrow ridge single stage diode lasers emitting 2, 2.2, and 3 μm were fabricated by two-step selective wet etching. The devices demonstrated stable single spatial mode operation in far field patterns. The 2 – 2.2 μm narrow ridge lasers generated more than 100 mW CW output power at RT, while the 3 μm narrow ridge lasers generated 16 mW CW output power at RT. These devices suffered from extra optical loss, this may be introduced by the roughness on narrow ridge and non-vertical sidewalls which were resulted by the wet etching.

Diffraction-limited 5.5-μm-wide narrow ridge single stage diode lasers emitting 3 μm were fabricated by Cl_2-free H_2/CH_4-based ICP-RIE. This dry etching technique does not introduce extra optical loss on narrow ridge devices, but cause extra operating voltage by plasma damage. The 2-mm-long AR/HR coated lasers indium soldered epi-down onto copper heatsink demonstrated 37 mW of output power at 17℃. The device far-field pattern remained nearly current independent up to the maximum output.

Diffraction-limited 6-μm-wide narrow ridge two-stage cascade lasers emitting 3.15 μm were fabricated by $SiCl_4$-based ICP-RIE. The cascade pumping achieved by efficient interband tunneling, resulted in twofold increase of the slope efficiency, and the internal efficiency was above 100%. The single spatial mode operation was confirmed by the far-field and near-field measurements. The far-field divergence showed single-lobe Gaussian-like pattern with FWHM of ~11 ° and ~67 ° on slow and fast axis, respectively. The measured lateral near-field modal dimension matched the lateral current spreading estimated from gain measurements. The scattering of the device fundamental mode on sidewall irregularities was suggested to explain observed ~6 cm^{-1} increase of the internal optical loss in narrow ridge devices. The 2-mm-long, AR/HR coated narrow ridge cascade diode lasers demonstrated diffraction-limited output power of 42 mW in CW regime at RT (17 ℃).

RT operated 3.27 μm single frequency mode diode lasers with output power level above 15 mW were designed and fabricated using GaSb-based type-I diode laser heterostructures. The laterally couple DFB lasers were fabricated using e-beam lithography and $SiCl_4$-based ICP-RIE. The 10-μm-wide first order index grating with period 480 nm was formed on both sides of the ~6-μm-wide ridge waveguide. AR/HR coated 2-mm-long devices demonstrated stable DFB operation in the temperature range from -20 ℃ to +20 ℃, with Bragg wavelength temperature tuning rate of 0.27 nm/K.

Diffraction-limited 5-μm-wide narrow ridge two-stage cascade lasers emitting 3 μm were fabricated by BCl_3/Cl_2-based ICP-RIE. This dry etching technique produces well defined narrow ridge profile with vertical sidewalls, and does not introduce extra optical loss or extra operating voltage on narrow ridge devices. The 2-mm-long AR/HR coated lasers demonstrated more than 100 mW of diffraction-limited output power in CW regime at 17 ℃, which was about threefold increasing as compared to the previous results from diffraction-limited single stage lasers. The BCl_3/Cl_2-based ICP-RIE technique can be utilized to fabricate rectangle-shaped DFB grating teeth with vertical sidewalls.

Chapter 5 Conclusion

In conclusion, the GaSb-based type-I QWs diode lasers emitting in the spectral range of 2.2 – 3.4 µm with CW operation at RT are very important, compact and efficient light sources for many applications. In this work, we are focusing on the development of single stage devices, multi-stage cascade devices, diffraction-limited and DFB devices for the 2.2 – 3.4 µm GaSb-based type-I QWs diode lasers.

Firstly, the three types of novel design and heterostructure optimization on GaSb-based single stage diode lasers in the spectral range of 2.2 to 3.4 µm were discussed. The 2.2 µm diode lasers and arrays with heavily strained active region demonstrated reduce threshold current densities, and output power of 1.6 W in CW from single emitter, 12 W in CW and 27 W in quasi-CW from linear arrays at RT. The 3.1 µm diode lasers with asymmetric separate confinement heterostructure demonstrated improved efficiency, and CW output power of 220 m W in RT. The 3.3 - 3.4 µm diode lasers diode lasers with triple-layer GaInAsSb QWs demonstrated decent CW output power and fine adjustment of operating wavelength.

Secondly, the cascade pumping scheme with GaSb-based type-I QWs were proposed, and two-and three- stage cascade diode lasers emitting in the spectral range of 2.4 to 3.3 µm were designed and fabricated. The cascade pumping was achieved utilizing efficient interband tunneling through "leaky" window in band alignment at GaSb/InAs heterointerface, and improved lasers' efficiency and CW operation performance in RT by carriers recycling. Two-stage cascade devices demonstrated record CW output powers of 1200 mW for 2.4µm, 750 mW for 2.7 µm and 830 mW for 3 µm at RT, respectively. Three-stage cascade devices demonstrated record CW output powers of 960 mW for 3 µm, and 120 mW for 3.3 µm at RT, respectively.

Last but not least, diffraction-limited and DFB devices emitting 3 μm and above were designed and fabricated using single stage and cascade diode lasers. Several fabrication techniques, including two-step selective wet etching, Cl_2-free H_2/Ch_4-based RIE, $SiCl_4$-based and BCl_3/Cl_2-based RIE were developed and optimized to improve the etching profile and qualities. By developing new etching techniques, the extra optical loss and high voltage issues were eliminated for narrow ridge devices. Diffraction-limited devices demonstrated CW output power of 37 mW for 3 μm single stage diode lasers, 42mW for 3.15 μm and 107 mW for 3 μm two-stage cascade lasers at RT, respectively. DFB single stage devices demonstrated CW output power of 15 mW for single wavelength of 3.27 μm at RT, and stable DFB operation in the temperature range from -20 ℃ to +20 ℃, with Bragg wavelength temperature tuning rate of 0.27 nm/K.

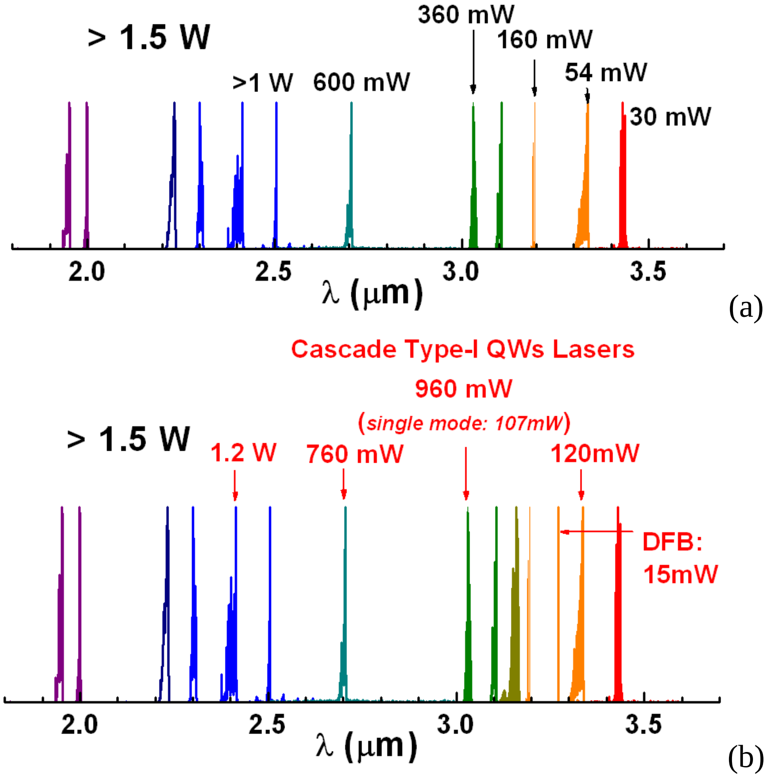

Figure 5.1 Comparison of the CW output power achieved in RT for the GaSb-based diode lasers emtting 3 μm and above at Stony Brook University for (a) multimode single stage devices by 2010, (b) cascade multimode, diffraction-limited and DFB devices by 2014.

References

[1] R. N. Hall, R. O. Carlson, T. J. Soltys, G. E. Fenner, and J. D. Kingsley, "Coherent Light Emission from Gaas Junctions," *Physical Review Letters,* vol. 9, pp. 366-&, 1962.

[2] M. I. Nathan, W. P. Dumke, G. Burns, F. H. Dill, and G. Lasher, "Stimulated Emission of Radiation from Gaas P-N Junctions," *Applied Physics Letters,* vol. 1, pp. 62-64, 1962.

[3] T. M. Quist, R. H. Rediker, R. J. Keyes, W. E. Krag, B. Lax, A. L. Mcwhorter, *et al.*, "Semiconductor Maser of Gaas," *Applied Physics Letters,* vol. 1, pp. 91-92, 1962.

[4] R. Hibst and U. Keller, "Experimental Studies of the Application of the Er Yag Laser on Dental Hard Substances .1. Measurement of the Ablation Rate," *Lasers in Surgery and Medicine,* vol. 9, pp. 338-344, 1989.

[5] C. Bader and I. Krejci, "Indications and limitations of Er : YAG laser applications in dentistry," *American Journal of Dentistry,* vol. 19, pp. 178-186, Jun 2006.

[6] A. Vicet, D. A. Yarekha, A. Perona, Y. Rouillard, S. Gaillard, and A. N. Baranov, "Trace gas detection with antimonide-based quantum-well diode lasers," *Spectrochimica Acta Part a-Molecular and Biomolecular Spectroscopy,* vol. 58, pp. 2405-2412, Sep 2002.

[7] L. S. Rothman, I. E. Gordon, Y. Babikov, A. Barbe, D. C. Benner, P. F. Bernath, *et al.*, "The HITRAN2012 molecular spectroscopic database," *Journal of Quantitative Spectroscopy & Radiative Transfer,* vol. 130, pp. 4-50, Nov 2013.

[8] H. D. Tholl, J. Wagner, M. Rattunde, S. Hugger, and F. Fuchs, "Mid-Infrared Semiconductor Lasers for Power Projection and Sensing," *Technologies for Optical Countermeasures Vii,* vol. 7836, 2010.

[9] D. Z. Garbuzov, H. Lee, V. Khalfin, R. Martinelli, J. C. Connolly, and G. L. Belenky, "2.3-2.7-mu m room temperature CW operation of InGaAsSb-AlGaAsSb broad waveguide SCH-QW diode lasers," *Ieee Photonics Technology Letters,* vol. 11, pp. 794-796, Jul 1999.

[10] L. Shterengas, G. Kipshidze, T. Hosoda, J. Chen, and G. Belenky, "Diode lasers emitting at 3 mu m with 300 mW of continuous-wave output power," *Electronics Letters,* vol. 45, pp. 942-U37, Aug 27 2009.

[11] T. Hosoda, G. Kipshidze, L. Shterengas, and G. Belenky, "Diode lasers emitting near 3.44 mu m in continuous-wave regime at 300K," *Electronics Letters,* vol. 46, pp. 1455-1456, Oct 14 2010.

[12] G. D. Sanders and Y. C. Chang, "Effects of Uniaxial-Stress on the Electronic and Optical-Properties of Gaas-Alxga1-Xas Quantum Wells," *Physical Review B,* vol. 32, pp. 4282-4285, 1985.

[13] J. F. Chen, D. Donetsky, L. Shterengas, M. V. Kisin, G. Kipshidze, and G. Beleaky, "Effect of Quantum Well Compressive Strain Above 1% On Differential Gain and Threshold Current Density in Type-I GaSb-Based Diode Lasers," *IEEE Journal of Quantum Electronics,* vol. 44, pp. 1204-1210, Nov-Dec 2008.

[14] L. Shterengas, G. L. Belenky, J. G. Kim, and R. U. Martinelli, "Design of high-power room-temperature continuous-wave GaSb-based type-I quantum-well lasers with lambda > 2.5 mu m," *Semiconductor Science and Technology,* vol. 19, pp. 655-658, May 2004.

[15] T. Newell, X. Wu, A. L. Gray, S. Dorato, H. Lee, and L. F. Lester, "The effect of increased valence band offset on the operation of 2 mu m GaInAsSb-AlGaAsSb lasers," *Ieee Photonics Technology Letters,* vol. 11, pp. 30-32, Jan 1999.

[16] M. Grau, C. Lin, O. Dier, C. Lauer, and M. C. Amann, "Room-temperature operation of 3.26 mu m GaSb-based type-I lasers with quinternary AlGaInAsSb barriers," *Applied Physics Letters,* vol. 87, Dec 12 2005.

[17] T. Hosoda, G. Kipshidze, L. Shterengas, S. Suchalkin, and G. Belenky, "200 mW type I GaSb-based laser diodes operating at 3 mu m: Role of waveguide width," *Applied Physics Letters,* vol. 94, Jun 29 2009.

[18] H. Takashi, *GaSb-based Type-I Diode Lasers Operating at 3 m and above: Design, Fabrication and Characteristics of Novel GaSb-based Type-I Diode Lasers*: LAP LAMBERT Academic Publishing, 2012.

[19] D. Z. Garbuzov, R. U. Martinelli, H. Lee, P. K. York, R. J. Menna, J. C. Connolly, *et al.*, "Ultralow-loss broadened-waveguide high-power 2 mu m AlGaAsS/InGaAsSb/GaSb separate-confinement quantum-well lasers," *Applied Physics Letters,* vol. 69, pp. 2006-2008, Sep 30 1996.

[20] Y. Rouillard, F. Genty, A. Perona, A. Vicet, D. A. Yarekha, G. Boissier, *et al.*, "Edge and vertical surface emitting lasers around 2.0-2.5 mu m and their applications," *Philosophical Transactions of the Royal Society of London Series a-Mathematical Physical and Engineering Sciences,* vol. 359, pp. 581-597, Mar 15 2001.

[21] G. W. Turner, H. K. Choi, and M. J. Manfra, "Ultralow-threshold (50 A/cm(2)) strained single-quantum-well GaInAsSb/AlGeAsSb lasers emitting at 2.05 mu m," *Applied Physics Letters,* vol. 72, pp. 876-878, Feb 23 1998.

[22] M. Garcia, A. Salhi, A. Perona, Y. Rouillard, C. Sirtori, X. Marcadet, *et al.*, "Low threshold high-power room-temperature continuous-wave operation diode laser emitting at 2.26 mu m," *Ieee Photonics Technology Letters,* vol. 16, pp. 1253-1255, May 2004.

[23] M. T. Kelemen, J. Gilly, M. Haag, J. Biesenbach, M. Rattunde, and J. Wagner, "Diode laser arrays for 1.8 to 2.3 mu m wavelength range," *Novel in-Plane Semiconductor Lasers Viii,* vol. 7230, 2009.

[24] L. Shterengas, G. L. Belenky, A. Gourevitch, D. Donetsky, J. G. Kim, R. U. Martinelli, *et al.*, "High-power 2.3-mu m GaSb-based linear laser array," *IEEE Photonics Technology Letters,* vol. 16, pp. 2218-2220, Oct 2004.

[25] L. Shterengas, G. Belenky, M. V. Kisin, and D. Donetsky, "High power 2.4 mu m heavily strained type-I quantum well GaSb-based diode lasers with more than 1 W of continuous wave output power and a maximum power-conversion efficiency of 17.5%," *Applied Physics Letters,* vol. 90, Jan 1 2007.

[26] J. F. Chen, G. Kipshidze, and L. Shterengas, "High-Power 2 mu m Diode Lasers With Asymmetric Waveguide," *IEEE Journal of Quantum Electronics,* vol. 46, pp. 1464-1469, Oct 2010.

[27] S. Simanowski, N. Herres, C. Mermelstein, R. Kiefer, J. Schmitz, M. Walther, *et al.,* "Strain adjustment in (GaIn)(AsSb)/(AlGa)(AsSb) QWs for 2.3-2.7 mu m laser structures," *Journal of Crystal Growth,* vol. 209, pp. 15-20, Jan 2000.

[28] G. Belenky, L. Shterengas, G. Kipshidze, and T. Hosoda, "Type-I Diode Lasers for Spectral Region Above 3 mu m," *IEEE Journal of Selected Topics in Quantum Electronics,* vol. 17, pp. 1426-1434, Sep-Oct 2011.

[29] D. Botez, "Design considerations and analytical approximations for high continuous-wave power, broad-waveguide diode lasers," *Applied Physics Letters,* vol. 74, pp. 3102-3104, May 24 1999.

[30] R. Liang, J. F. Chen, G. Kipshidze, D. Westerfeld, L. Shterengas, and G. Belenky, "High-Power 2.2-mu m Diode Lasers With Heavily Strained Active Region," *IEEE Photonics Technology Letters,* vol. 23, pp. 603-605, May 15 2011.

[31] A. Bauer, K. Rossner, T. Lehnhardt, M. Kamp, S. Hofling, L. Worschech, *et al.*, "Mid-infrared semiconductor heterostructure lasers for gas sensing applications," *Semiconductor Science and Technology,* vol. 26, Jan 2011.

[32] I. Vurgaftman, W. W. Bewley, C. L. Canedy, C. S. Kim, M. Kim, C. D. Merritt, *et al.*, "Interband Cascade Lasers With Low Threshold Powers and High Output Powers," *IEEE Journal of Selected Topics in Quantum Electronics,* vol. 19, Jul-Aug 2013.

[33] F. Capasso, "High-performance midinfrared quantum cascade lasers," *Optical Engineering,* vol. 49, Nov 2010.

[34] K. Vizbaras and M. C. Amann, "Room-temperature 3.73 mu m GaSb-based type-I quantum-well lasers with quinternary barriers," *Semiconductor Science and Technology,* vol. 27, Mar 2012.

[35] J. R. Meyer, C. A. Hoffman, F. J. Bartoli, and L. R. Rammohan, "Type-Ii Quantum-Well Lasers for the Midwavelength Infrared," *Applied Physics Letters,* vol. 67, pp. 757-759, Aug 7 1995.

[36] A. P. Ongstad, R. Kaspi, M. L. Tilton, J. R. Chavez, and G. C. Dente, "Performance comparison of optically pumped type-II midinfrared lasers," *Journal of Applied Physics,* vol. 98, Aug 15 2005.

[37] I. Vurgaftman, J. R. Meyer, and L. R. Ram-Mohan, "Band parameters for III-V compound semiconductors and their alloys," *Journal of Applied Physics,* vol. 89, pp. 5815-5875, Jun 1 2001.

[38] G. P. Donati, R. Kaspi, and K. J. Malloy, "Interpolating semiconductor alloy parameters: Application to quaternary III-V band gaps," *Journal of Applied Physics,* vol. 94, pp. 5814-5819, Nov 1 2003.

[39] C. Alibert, M. Skouri, A. Joullie, M. Benouna, and S. Sadiq, "Refractive-Indexes of Alsb and Gasb-Lattice-Matched Alxga1-Xasysb1-Y in the Transparent Wavelength Region," *Journal of Applied Physics,* vol. 69, pp. 3208-3211, Mar 1 1991.

[40] B. W. Hakki and T. L. Paoli, "Gain Spectra in Gaas Double-Heterostructure Injection Lasers," *Journal of Applied Physics,* vol. 46, pp. 1299-1306, 1975.

[41] R. Liang, T. Hosoda, G. Kipshidze, L. Shterengas, and G. Belenky, "GaSb-Based Diode Lasers With Asymmetric Separate Confinement Heterostructure," *IEEE Photonics Technology Letters,* vol. 25, pp. 925-928, May 15 2013.

[42] T. Hosoda, G. Kipshidze, G. Tsvid, L. Shterengas, and G. Belenky, "Type-I GaSb-Based Laser Diodes Operating in 3.1-to 3.3-mu m Wavelength Range," *IEEE Photonics Technology Letters,* vol. 22, pp. 718-720, May 15 2010.

[43] R. F. Kazarinov and G. L. Belenky, "Novel design of semiconductor lasers for optical communication," *Physics and Simulation of Optoelectronic Devices Iii,* vol. 2399, pp. 386-395, 1995.

[44] J. A. Gupta, P. J. Barrios, G. C. Aers, P. Waldron, and C. Storey, "Room-temperature continuous-wave operation of type-I GaSb-based lasers at 3.1 mu m," *Electronics Letters,* vol. 45, pp. 835-836, Jul 30 2009.

[45] R. Liang, G. Kipshidze, T. Hosoda, L. Shterengas, and G. Belenky, "3.3-3.4-mu m Diode Lasers Based on Triple-Layer GaInAsSb Quantum Wells," *IEEE Photonics Technology Letters,* vol. 26, pp. 664-666, Apr 1 2014.

[46] L. Shterengas, R. Liang, G. Kipshidze, T. Hosoda, S. Suchalkin, and G. Belenky, "Type-I quantum well cascade diode lasers emitting near 3 mu m," *Applied Physics Letters,* vol. 103, Sep 16 2013.

[47] J. Faist, F. Capasso, D. L. Sivco, C. Sirtori, A. L. Hutchinson, and A. Y. Cho, "Quantum Cascade Laser," *Science,* vol. 264, pp. 553-556, Apr 22 1994.

[48] Kazarino.Rf and R. A. Suris, "Possibility of Amplication of Electromagnetic Waves in a Semiconductor with a Superlattice," *Soviet Physics Semiconductors-Ussr,* vol. 5, pp. 707-&, 1971.

[49] M. Razeghi, "High-Performance InP-Based Mid-IR Quantum Cascade Lasers," *Ieee Journal of Selected Topics in Quantum Electronics,* vol. 15, pp. 941-951, May-Jun 2009.

[50] R. Q. Yang, "Infrared-Laser Based on Intersubband Transitions in Quantum-Wells," *Superlattices and Microstructures,* vol. 17, pp. 77-83, 1995.

[51] I. S. Tarasov, N. A. Pikhtin, S. O. Slipchenko, Z. N. Sokolova, D. A. Vinokurov, K. S. Borschev*, et al.*, "High power CW (16 W) and pulse (145 W) laser diodes based on quantum well heterostructures," *Spectrochimica Acta Part a-Molecular and Biomolecular Spectroscopy,* vol. 66, pp. 819-823, Apr 2007.

[52] S. Patterson, P. Leisher, K. Price, K. Kennedy, W. Dong, M. Grimshaw*, et al.*, "High-power diode lasers operating around 1500-nm for eyesafe applications," *Laser Source Technology for Defense and Security Iv,* vol. 6952, 2008.

[53] C. H. Henry, R. A. Logan, F. R. Merritt, and J. P. Luongo, "The Effect of Intervalence Band Absorption on the Thermal-Behavior of Ingaasp Lasers," *Ieee Journal of Quantum Electronics,* vol. 19, pp. 947-952, 1983.

[54] J. Piprek, "Simulation of semiconductor optoelectronic devices," *Iee Proceedings-Optoelectronics,* vol. 149, pp. 121-121, Aug 2002.

[55] A. Lyakh and P. Zory, "Gallium-arsenide-based bipolar cascade lasers with deep quantum-well tunnel junctions," *Ieee Photonics Technology Letters,* vol. 18, pp. 2656-2658, Nov-Dec 2006.

[56] R. Q. Yang and Y. M. Qiu, "Bipolar cascade lasers with quantum well tunnel junctions," *Journal of Applied Physics,* vol. 94, pp. 7370-7372, Dec 1 2003.

[57] R. Koda, C. S. Wang, D. D. Lofgreen, and L. A. Coldren, "High-differential-quantum-efficiency, long-wavelength vertical-cavity lasers using five-stage bipolar-cascade active regions," *Applied Physics Letters,* vol. 86, May 23 2005.

[58] D. Sanchez, L. Cerutti, and E. Tournie, "Mid-IR GaSb-Based Bipolar Cascade VCSELs," *Ieee Photonics Technology Letters,* vol. 25, pp. 882-884, May 1 2013.

[59] S. Jung, S. Suchalkin, G. Kipshidze, D. Westerfeld, and G. L. Belenky, "Light-Emitting Diodes Operating at 2 mu m With 10 mW Optical Power," *Ieee Photonics Technology Letters,* vol. 25, pp. 2278-2280, Dec 1 2013.

[60] L. Shterengas, R. Liang, G. Kipshidze, T. Hosoda, S. Suchalkin, and G. Belenky, "Cascade pumping of GaSb-based type-I quantum well diode lasers," *Novel in-Plane Semiconductor Lasers Xiii,* vol. 9002, 2014.

[61] R. Liang, L. Shterengas, G. Kipshidze, T. Hosoda, S. Suchalkin, and G. Belenky, "Novel Cascade Diode Lasers Based on Type-I Quantum Wells," *International Journal of High Speed Electronics and Systems,* vol. 23, p. 1450022, Nov 3 2014.

[62] J. Chen, G. Kipshidze, L. Shterengas, T. Hosoda, Y. Wang, D. Donetsky, *et al.*, "2.7-mu m GaSb-Based Diode Lasers With Quinary Waveguide," *IEEE Photonics Technology Letters,* vol. 21, pp. 1112-1114, Aug 15 2009.

[63] L. Shterengas, R. Liang, G. Kipshidze, T. Hosoda, G. Belenky, S. Bowman, *et al.*, "Cascade type-I quantum well diode lasers emitting 960 mW near 3 μm," *Applied Physics Letters,* vol. 105, p. 161112, Oct 20 2014.

[64] T. Unuma, M. Yoshita, T. Noda, H. Sakaki, and H. Akiyama, "Intersubband absorption linewidth in GaAs quantum wells due to scattering by interface roughness, phonons, alloy disorder, and impurities," *Journal of Applied Physics,* vol. 93, pp. 1586-1597, Feb 1 2003.

[65] J. A. Gupta, A. Bezinger, P. J. Barrios, J. Lapointe, D. Poitras, and P. Waldron, "High-resolution methane spectroscopy using InGaAsSb/AlInGaAsSb laterally-coupled index-grating distributed feedback laser diode at 3.23 mu m," *Electronics Letters,* vol. 48, pp. 396-U135, Mar 29 2012.

[66] D. Caffey, T. Day, C. S. Kim, M. Kim, I. Vurgaftman, W. W. Bewley, *et al.*, "Performance characteristics of a continuous-wave compact widely tunable external cavity interband cascade lasers," *Optics Express,* vol. 18, pp. 15691-15696, Jul 19 2010.

[67] D. A. Yarekha, G. Glastre, A. Perona, Y. Rouillard, F. Genty, E. M. Skouri, *et al.*, "High temperature GaInSbAs/GaAlSbAs quantum well singlemode continuous wave lasers emitting near 2.3 mu m," *Electronics Letters,* vol. 36, pp. 537-539, Mar 16 2000.

[68] S. Jung, G. Kipshidze, R. Liang, S. Suchalkin, L. Shterengas, and G. Belenky, "GaSb-Based Mid-Infrared Single Lateral Mode Lasers Fabricated by Selective Wet Etching Technique with an Etch Stop Layer," *Journal of Electronic Materials*, vol. 41, pp. 899-904, May 2012.

[69] S. Jung, R. Liang, G. Kipshidze, S. Suchalkin, L. Shterengas, and G. Belenky, "Single spatial mode 2-2.2 mu m diode lasers fabricated by selective wet etching," *Semiconductor Science and Technology*, vol. 27, Aug 2012.

[70] T. Hosoda, G. Kipshidze, L. Shterengas, and G. Belenky, "Single spatial mode 3 mm diode lasers with continuous-wave output power of 15 mW at room temperature," *Electronics Letters*, vol. 47, pp. 1341-U60, Nov 24 2011.

[71] A. Soibel, C. Frez, A. Ksendzov, S. Keo, S. Forouhar, G. Tsvid, *et al.*, "The 3.0-3.2 mu m wavelength range narrow ridge waveguide Sb-based semiconductor diode lasers operating up to 333 K," *Semiconductor Science and Technology*, vol. 26, Sep 2011.

[72] T. Lehnhardt, M. Hummer, K. Rossner, M. Muller, S. Hofling, and A. Forchel, "Continuous wave single mode operation of GaInAsSb/GaSb quantum well lasers emitting beyond 3 mu m," *Applied Physics Letters*, vol. 92, May 5 2008.

[73] J. Chen, T. Hosoda, G. Kipshidze, L. Shterengas, G. Belenky, A. Soibel, *et al.*, "Single spatial mode room temperature operated 3.15 mu m diode lasers," *Electronics Letters*, vol. 46, pp. 367-U5479, Mar 4 2010.

[74] T. Hosoda, R. Liang, G. Kipshidze, L. Shterengas, and G. Belenky, "Room temperature operated diffraction limited lambda similar or equal to 3 mu m diode lasers with 37 mW of continuous-wave output power," *Electronics Letters*, vol. 49, pp. 667-668, May 9 2013.

[75] J. W. Lee, C. R. Abernathy, S. J. Pearton, C. Constantine, R. J. Shul, and W. S. Hobson, "Etching of Ga-based III-V semiconductors in inductively coupled Ar and CH4/H-2-based plasma chemistries," *Plasma Sources Science & Technology*, vol. 6, pp. 499-507, Nov 1997.

[76] R. Liang, L. Shterengas, T. Hosoda, A. Stein, M. Lu, G. Kipshidze, *et al.*, "Diffraction limited 3.15 mu m cascade diode lasers," *Semiconductor Science and Technology*, vol. 29, Nov 2014.

[77] *2001 BeamPROP™ Version 5.0, Synopsis Inc. Optical Solutions Group*.

[78] http://refractiveindex.info/ [Online].

[79] A. Chandola, R. Pino, and P. S. Dutta, "Below bandgap optical absorption in tellurium-doped GaSb," *Semiconductor Science and Technology*, vol. 20, pp. 886-893, Aug 2005.

[80] L. Naehle, C. Zimmermann, S. Belahsene, M. Fischer, G. Boissier, P. Grech, *et al.*, "Monolithic tunable GaSb-based lasers at 3.3 mu m," *Electronics Letters*, vol. 47, pp. 1092-U80, Sep 15 2011.

[81] J. A. Gupta, B. F. Ventrudo, P. Waldron, and P. J. Barrios, "External cavity tunable type-I diode laser with continuous-wave singlemode operation at 3.24 mu m," *Electronics Letters*, vol. 46, pp. 1218-U76, Aug 19 2010.

[82] W. Y. Choi, J. C. Chen, and C. G. Fonstad, "Evaluation of coupling coefficients for laterally-coupled distributed feedback lasers," *Japanese Journal of Applied Physics Part 1-Regular Papers Short Notes & Review Papers*, vol. 35, pp. 4654-4659, Sep 1996.

[83] J. A. Gupta, P. J. Barrios, J. Lapointe, G. C. Aers, C. Storey, and P. Waldron, "Modal Gain of 2.4-mu m InGaAsSb-AlGaAsSb Complex-Coupled Distributed-Feedback Lasers," *IEEE Photonics Technology Letters*, vol. 21, pp. 1532-1534, Oct 15 2009.

[84] L. Naehle, S. Belahsene, M. von Edlinger, M. Fischer, G. Boissier, P. Grech, *et al.*, "Continuous-wave operation of type-I quantum well DFB laser diodes emitting in 3.4 mu m wavelength range around room," *Electronics Letters*, vol. 47, pp. 46-U70, Jan 6 2011.

[85] C. H. Henry, "Performance of Distributed Feedback Lasers Designed to Favor the Energy-Gap Mode," *IEEE Journal of Quantum Electronics*, vol. 21, pp. 1913-1918, Dec 1985.

[86] S. Forouhar, R. M. Briggs, C. Frez, K. J. Franz, and A. Ksendzov, "High-power laterally coupled distributed-feedback GaSb-based diode lasers at 2 mu m wavelength," *Applied Physics Letters*, vol. 100, Jan 16 2012.

[87] T. Yamanaka, Y. Yoshikuni, K. Yokoyama, W. Lui, and S. Seki, "Theoretical-Study on Enhanced Differential Gain and Extremely Reduced Linewidth Enhancement Factor in Quantum-Well Lasers," *IEEE Journal of Quantum Electronics*, vol. 29, pp. 1609-1616, Jun 1993.

[88] G. Belenky, C. L. Reynolds, L. Shterengas, M. S. Hybertsen, D. V. Donetsky, G. E. Shtengel, *et al.*, "Effect of p-doping on the temperature dependence of differential gain in FP and DFB 1.3-mu m InGaAsP-InP multiple-quantum-well lasers," *IEEE Photonics Technology Letters*, vol. 12, pp. 969-971, Aug 2000.

[89] L. Shterengas, G. L. Belenky, A. Gourevitch, J. G. Kim, and R. U. Martinelli, "Measurements of alpha-factor in 2-2.5 mu m type-I In(Al)GaAsSb/GaSb high power diode lasers," *Applied Physics Letters*, vol. 81, pp. 4517-4519, Dec 9 2002.